Nanowire photoluminescence for photovoltaics

Citation for published version (APA):
Vu, T. T. T. (2015). *Nanowire photoluminescence for photovoltaics*. [Phd Thesis 1 (Research TU/e / Graduation TU/e), Applied Physics and Science Education]. Technische Universiteit Eindhoven.

Document status and date:
Published: 31/03/2015

Document Version:
Publisher’s PDF, also known as Version of Record (includes final page, issue and volume numbers)

Please check the document version of this publication:

• A submitted manuscript is the version of the article upon submission and before peer-review. There can be important differences between the submitted version and the official published version of record. People interested in the research are advised to contact the author for the final version of the publication, or visit the DOI to the publisher's website.
• The final author version and the galley proof are versions of the publication after peer review.
• The final published version features the final layout of the paper including the volume, issue and page numbers.

Link to publication

General rights
Copyright and moral rights for the publications made accessible in the public portal are retained by the authors and/or other copyright owners and it is a condition of accessing publications that users recognise and abide by the legal requirements associated with these rights.

- Users may download and print one copy of any publication from the public portal for the purpose of private study or research.
- You may not further distribute the material or use it for any profit-making activity or commercial gain
- You may freely distribute the URL identifying the publication in the public portal.

If the publication is distributed under the terms of Article 25fa of the Dutch Copyright Act, indicated by the “Taverne” license above, please follow below link for the End User Agreement:

www.tue.nl/taverne

Take down policy
If you believe that this document breaches copyright please contact us at:

openaccess@tue.nl

providing details and we will investigate your claim.

Download date: 04. Oct. 2023

Nanowire Photoluminescence for Photovoltaics

PROEFSCHRIFT

ter verkrijging van de graad van doctor aan de
Technische Universiteit Eindhoven, op gezag van de rector
magnificus prof.dr.ir. C.J. van Duijn, voor een commissie
aangewezen door het College voor Promoties, in het openbaar
te verdedigen op dinsdag 31 maart 2015 om 14:00 uur

door

Vu Tran Thanh Thuy

geboren te Nam Dinh, Viëtnam

Dit proefschrift is goedgekeurd door de promotoren en de samenstelling van de promotiecommissie is als volgt:

voorzitter:	prof.dr.ir G.M.W. Kroesen
1e promotor:	prof.dr. E.P.A.M. Bakkers
2e promotor:	prof.dr. J. Gómez Rivas
copromotor:	dr. J.E.M. Haverkort
leden:	prof.dr. S. Christiansen (Helmholtz-Center Berlin)
	prof.dr. T. Gregorkiewicz (University of Amsterdam)
	prof.dr.ir. R.A.J. Janssen
	prof.dr. R.E.I. Schropp

A catalogue record is available from the Eindhoven University of Technology Library

Nanowire Photoluminescence for Photovotaics, by Thuy T.T. Vu,

ISBN: 978-90-386-3809-6

The work presented in this thesis has been carried out in the group of Photonics and Semiconductor Nanophysics, at the Department of Applied Physics of the Eindhoven University of Technology, the Netherlands.

This work was supported by long-term energy and innovation program EOS-LT, which is funded by Agentschap NL, as well as the Cobra research school funded by NWO. The research leading to these results has also received funding from the European Union Seventh Framework Programme under grant agreement No. 265073.

Printed by Ipskamp Drukkers

Cover art: based on the time-resolve photoluminescence measurements along an InP nanowire

Contents

Chapter 1

Introduction

1.1 Semiconductor nanowires

Semiconductors have undoubtedly changed the world beyond anything that could have been imagined before. It is the foundation for electronic and optoelectronic devices that impact many areas of our lives, from simple household appliances and multimedia systems to computing, communications and medical instruments. According to Moore's law the number of transistors that can be placed on an integrated circuit doubles every two year, making better, faster, more efficient devices, using much less material. This can be accomplished by scaling down the size to the sub micrometer or even to the nanometer scale. These nanometer scale fabrication routes are usually categorized into two paradigms, "bottom-up" or "top-down". The 'top-down' approach relies on size reduction employing lithography and selective etching techniques to fabricate nanometer-sized structures. This technique is very popular in the silicon technology. The second route is called 'bottom-up', in which the desired nanostructures are built up from individual atoms and molecules.

Semiconductor nanowires (NWs), which are mostly fabricated by the bottom-up approach, have recently become a powerful class of new materials that open up tremendous opportunities for novel nanoscale photonic and electronic devices. NWs are defined as structures with a diameter in the range of tens of nanometers, and a third dimension, typically in the range of micrometers. They are recognized as promising candidates for quantum bits [1, 2] the realization of Majorana's fermions [3], single photon detectors [4] and next generation photovoltaic cells [5-9].

NW growth has been demonstrated using several epitaxial techniques, including laser ablation [10], molecular beam epitaxy (MBE) [11], chemical beam epitaxy (CBE) [12], and metalorganic vapor phase epitaxy (MOVPE) [13]. For semiconductor NW fabrication, the bottom-up vapour-liquid-solid (VLS) growth mechanism is most commonly used.

1.2 Vapor liquid solid growth

The VLS method, discovered by Wagner and Ellis in 1964 at Bell Laboratories [14], uses metal nanoparticles as catalysts to control the nucleation and subsequently elongation steps of NW growth. By using VLS growth, a broad range of material compositions from group IV NW, such as silicon [15, 16]and germanium [17], III-V NWs such as InP [18, 19], GaAs [20, 21], GaP [22, 23], III-Nitrides such as GaN [11, 24], and II/VI semiconductors such as ZnO [25, 26] have been grown.

A schematic of the VLS mechanism is shown in figure 1.1. In this growth mechanism, a metallic seed particles (usually gold) are deposited on the substrate prior to the growth. We focus here on the growth of III-V nanowires on corresponding substrates. The substrate is heated up under group V atmosphere. Gold particles melt to form a liquid droplet. During this process, an alloy of Au-III is form by dissolving semiconductor material from the substrate, and by decomposing group III precursors through liquid vapor interfaces. When super saturation is reached, the nucleation starts. NW axial growth is maintained by constant supply of precursors into the eutectic alloy. The diameter of the axially grown NW is mainly determined by the size of the deposited catalyst and the length is defined by the growth time. Lateral vapor-solid (VS) growth on the sidewall of the NW also takes place during VLS, but at much lower growth rate and can be suppressed by *in-situ* passivation or etching method, e.g. by introducing HCl [27].

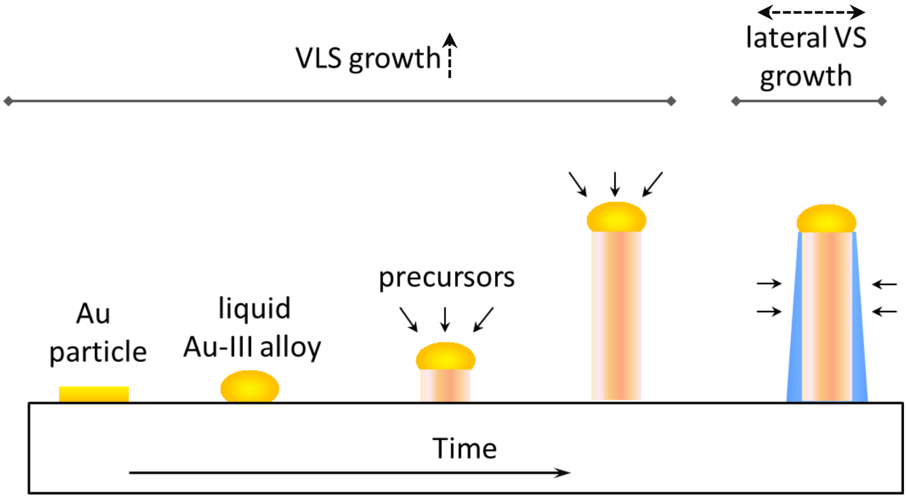

Figure 1.1. Schematic illustration of the different stages of vapor-liquid-solid (VLS) growth: (left to right) Au particles are deposited on the substrate; Au particles are heated up and form and Au-III alloy; The Au-III droplet is supplied with precursors. When it is supersaturated, the growth of a NW starts in the axial direction; the NW continues to growth longer with further precursor supply; Lateral growth by vapour-solid (VS) growth also occurs on the sidewall of the NW during the axial growth especially at higher temperatures.

Besides VLS, many other growth mechanisms such as vapor-solid-solid (VSS) [28] and solution-liquid-solid methods [29] have also been used to fabricate semiconductor NWs. In this thesis, the NW samples are grown by the VLS mechanism.

1.3 Nanowires for novel nanoscale photonic and energy devices

In this section we discuss several distinct advantages of semiconductor NWs which make them a great platform for fundamental research and various device applications. So what is the fundamental difference between a NW as compared to a thin film, a bulk semiconductor or other nanostructures such as nanotubes or nanocrystals?

1.3.1 Nanowires can be integrated with existing silicon technology

The unique quasi one-dimensionality inherent to a NW may solve some long-standing technical problems that have plagued the thin film community [30, 31]. For instance, one of the key goals of optoelectronics is to integrate materials with superior optical properties, such as III-V semiconductors, into silicon platform to combine the strengths of both material systems. However, due to the lattice mismatch [32, 33], the thin film growth often results in defective materials. This inherent lattice mismatch problem prevents the integration of optical grade III-V semiconductors to advanced silicon technology. NWs, on the other hand, have unique ability to accommodate strain via radial expansion or contraction. For instance, InSb/GaAs heterostructure NWs with an extreme lattice mismatch of 14.6% have been reported [34]. This enables the growth of dislocation-free semiconductors on lattice-mismatched substrates such as GaAs, InAs and InP NWs on silicon and germanium wafers [35-40]. In addition, this allows a large variety of axially grown III-V materials combination [41, 42], and even III-V and IV hybrid NW structures, such as GaP-Si-GaP-GaAs-Si NWs [43, 44], as shown in figure 1.1(e, f) The ability to stack almost unlimited NW heterostructure combinations also opens up possibilities for the creation of multi-junction photovoltaic cells which are perfectly matched to the entire solar spectrum for highly efficient solar energy harvesting [8].

1.3.2 Nanowires for future photovoltaics

Current solar cell technologies are dominated by silicon solar cells which presently converts 21.5% (best commercial products [45]) of the solar energy into electricity. Solar cells made from III-V compound semiconductors have much higher efficiencies, due to their better optical (absorption) and electrical (charge mobility) properties and the ability to fabricate multiple junctions or heterostructures to cover a broader range of the solar spectrum. It has been demonstrated that multi-junction III-V solar cells (lab cells) can reach efficiencies of over 44.7% [46] under concentrated solar light [47]. However, the growth of III-V materials requires expensive III-V precursors and substrates, which makes

III-V solar cells only attractive for concentrated photovoltaics but too costly for rooftop solar panels without using solar concentration.

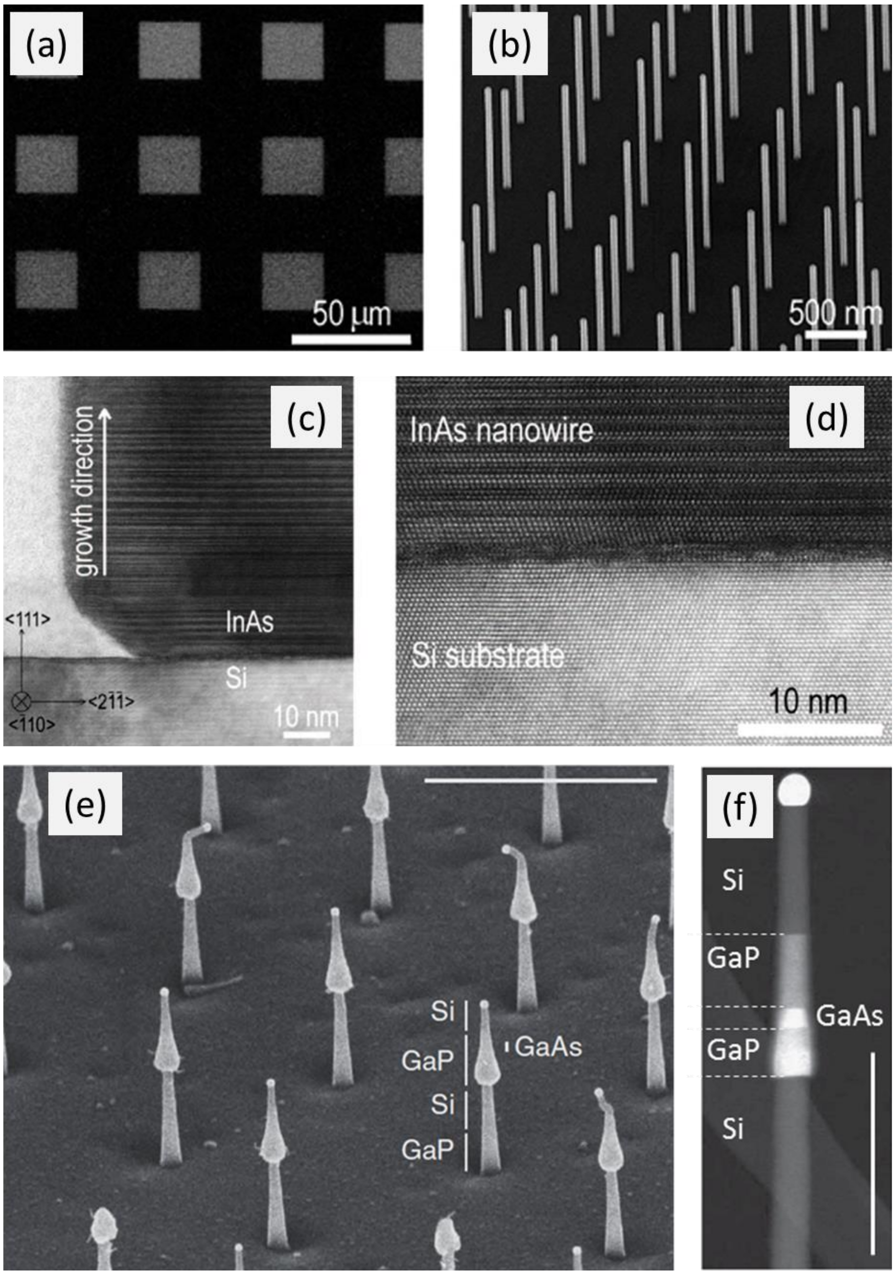

Figure 1.2. (a)-(d) Position-controlled vertical InAs nanowires epitaxially grown on silicon (111) by using selective-area metal-organic vapor epitaxy (adapted from Ref [38]). (a) Overview of InAs nanowire arrays on patterned substrate. (b) 45°-tilted view showing a vertical InAs nanowire array. (c) High-resolution TEM image of InAs nanowires on a Si(111) substrate and (d) high magnification image of panel (c). (e) SEM picture of an array of GaP–Si–GaP–GaAs–GaP–Si hybrid nanowires. Tilt angle is 45^{o}, and scale bar is 1 µm. (f) High angle annular dark-field (HAADF) image of a 25 nm-diameter Si–GaP–GaAs–GaP–Si nanowire (scale bar is 200 nm) [43].

As discussed above, one way to reduce cost while maintaining the advantages of direct bandgap III-V semiconductors is to use NW solar cells which are grown directly on an inexpensive substrate, [7, 48, 49] such as silicon. This offers opportunities for the fabrication of highly efficient, low cost solar cells based on III-V materials, using very small material quantities on large and relatively inexpensive substrates.

Furthermore, recent work has shown that the NW geometry allows waveguiding and optical resonance effects which can be exploited to efficiently absorb light. It has been recently experimentally shown by the group in Lund that an array of InP NWs with 400 nm pitch and 2000 nm length are absorbing 94 % of the incident light while covering only 10 % (diameter of about 140 nm) of the underlying surface [50]. The high absorption efficiency of NWs and diluted NW arrays has also been pointed out by a numerous theoretical and experimental studies [51-55]. This is due to the fact that the optical absorption cross-section of thin NWs is much larger than their geometrical cross section, due to weakly confined leaky modes.

There is an intense research going on in the field of NW solar cell, using both coaxial and axial p-n junctions and both group IV and group III-V materials [5, 6, 49, 56-62]. The coaxial or core-shell structures show great advantages in carrier collection while the axial structures enable the stacking of junctions with different band gaps into a multi-junction solar cell. It was recently demonstrated that an InP array with an axial pn-junction could convert more than 70 % of the photons of the solar spectrum (with energy above the band gap of InP) into photocurrent, giving rise to a record 13.8 % conversion efficiency using a 10.2% substrate area coverage [61]. The SEM image of such NW solar cell device and the corresponding I-V characterization at one sun is shown in figure 1.3.

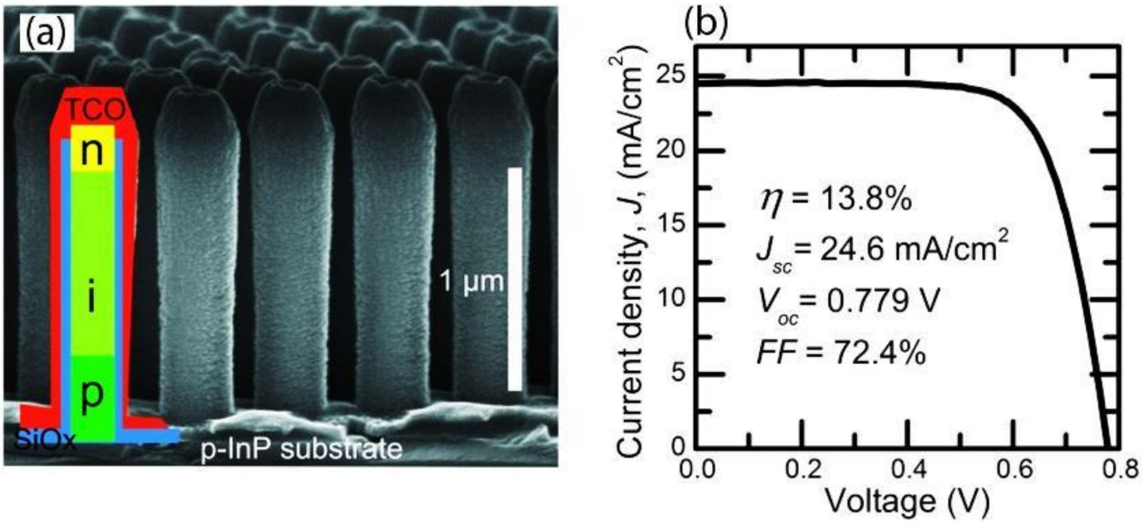

Figure 1.3. (A) Scanning electron microscopy image of processed nanowire array solar cells [61]. (b) Current-voltage curve of the solar cell device. The nanowires cover 10.2% of the substrate surface and achieve 13.8% efficiency at one sun.

In Eindhoven, Cui et al., have demonstrated 11.1 % efficiency for an InP NW array solar cell by removing the residual VS growth on the NW sidewall [62]. This solar cell efficiency is achieved with a not yet fully optimized NW array which covers only 1.8% of the substrate surface area. There is still a lot of room for improvement, such as improving the solar light absorption and the minority carrier lifetime by improving the surface passivation [48, 63]. Studies of single NW devices also provide insight into the fundamental differences between NW solar cells and conventional thin film solar cells [7] [49]. This thesis is dedicated to an optical study on InP nanowires, aiming to study the background impurity concentrations and the minority carrier lifetimes in different types of InP nanowires.

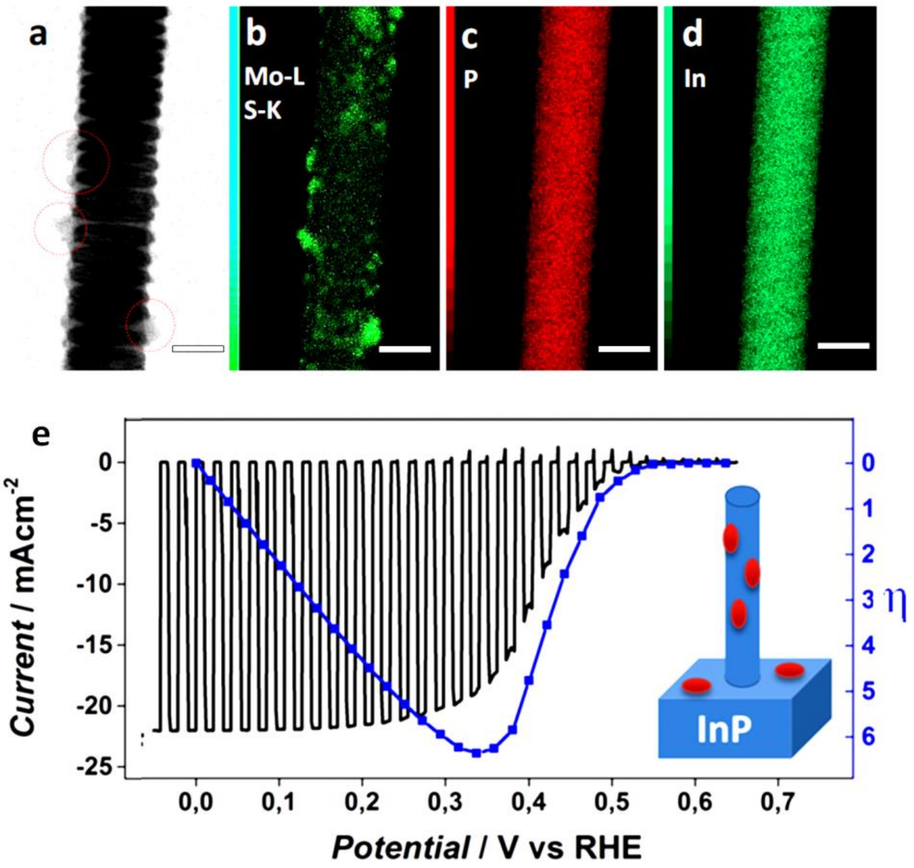

Figure 1.4. InP nanowires for water spitting application. (a) Transmission electron microscopy image of an InP nanowire after MoS$_3$ deposition. MoS$_3$ EDX mapping of (b) MOS$_3$, (c) P and (d) In elements. (e) Current-potential curves (black solid line) and photocathode conversion efficiencies (blue squares) of InP nanowire arrays with MoS$_3$ in 1M HClO$_4$ under chopped AM1.5G illumination.

NWs also show great potential for fuel cell applications such as water splitting [64, 65]. Due to their high aspect ratio, the NW geometry decouples the directions of light absorption and charge-carrier collection, and thus enhances charge separation. [66] Figure 1.4 shows p-type InP NWs coated with noble-metal-free MoS$_3$ nanoparticles, as a cathode for photoelectrochemical hydrogen production from water [65]. A photocathode efficiency of 6.4% under Air Mass 1.5G illumination was demonstrated with only 3% of the surface area covered by the NW array. A recent theoretical work has predicted that the efficiency of a tandem photoelectrochemical cell can theoretically reach 31.1% [67] when all losses can be removed and using an optimized combination of band gap energies and catalyst. Nanowires offer an excellent platform for fabricating these lattice mismatched materials without any misfit dislocations. Provided that we can eliminate all loss mechanisms, NWs thus promise to enable the fabrication of very high efficiency water splitting devices.

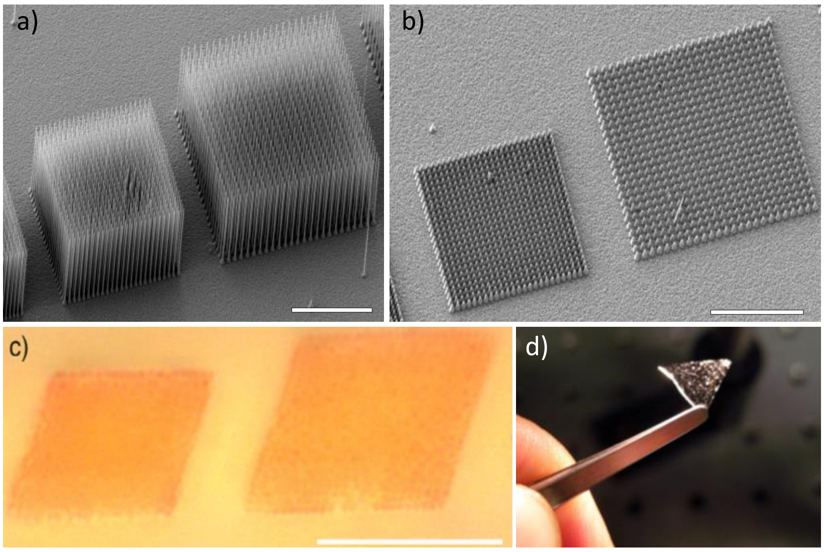

Figure 1.5. Scanning electron microscope (SEM) images of a field of GaP nanowires on a substrate (a) before and (b) after complete transfer into a PDMS polymer layer. (c) Optical microscopy images of nanowire fields embedded in PDMS after removal. (d) A photograph of a PDMS sample with the NWs embedded. Scale bars in a) and b) are 10 µm (adapted from [68]).

NW arrays can finally also be embedded into a transparent and flexible polymer, such as PDMS. It has already been shown that a flexible layer of PDMS containing a nanowire array, can be peeled off from the original substrate with almost 100% removal yield [50] [68, 69] as illustrated in figure 1.5. This procedure is very promising for the fabrication of highly versatile flexible solar modules, using only small quantities of expensive III/V materials per unit area (< 96 mg/m^2) for reaching a solar conversion energy that should eventually approach 30% for a single band gap cell.

1.4 Scope of this thesis

This thesis is dedicated to the optical and structural properties of conventional and novel crystal structures of some III-V compound and NWs for photovoltaics, and also for other quantum and optoelectronic applications. The outline of the thesis is as follows.

Chapter 2 describes the background theory of a solar cell with an emphasis on the optical absorption and minority carrier lifetime in a solar cell. Different recombination processes, which are important for evaluating the solar cell performance, are discussed. The micro-photoluminescence and time-resolved photoluminescence setups to measure optical properties of single NW are described.

The strategy to obtain high NW material quality, which is essential for NW solar cells, will be presented in chapter 3. We focus on crystal phase purity, reduction of impurities and the suppression of NW tapering by using high temperature growth in combination with *in situ* etching by HCl. We demonstrate that the post-growth etching can further remove the low quality layers on the NW sidewalls. Those steps are essential for the fabrication of high efficiency NW solar cells.

In chapter 4, single crystal, non-tapered wurtzite and zinc blende twinning superlattice (ZB TSL) InP NWs, fabricated at high temperature with *in-situ* etching with HCl, are studied. We demonstrate that VLS-grown WZ NWs are almost impurity-free due to sidewall etching by HCl. The ZB NWs exhibit a PL spectrum being unaffected by the twinning planes. Both types of NWs exhibit long carrier lifetimes and high PL efficiency up to room temperature, thus showing great potential for NW devices.

While stacking faults in NWs can induce carrier scattering and trapping and therefore affect the carrier mobility, they can also be exploited to tailor crystal phase quantum structures. In Chapter 5, we show that the switching of the crystal phase along the axial direction of a GaP NW, with a precision down to a few monolayers, facilitates the creation of position- and size-controlled crystal phase quantum disks (CPQD). These quantum disk emissions are sharp with well-defined energies, which is highly attractive for solid-state quantum device applications. We also demonstrate that a strong spontaneous polarization field is present in wurtzite GaP and leads to the quantum-confined Stark effect in CPQD.

Vertical growth of InP NWs on the (100) industry standard InP substrates with pure zincblende (ZB) crystal structure are technologically relevant for NW solar cells and optoelectronic devices. In chapter 6, we demonstrate that InP NWs grown along the <100> direction are pure ZB regardless of the use of the *in-situ* dopants. The n-type (with sulphur) and p-type (with zinc) doped <100> InP NWs are investigated by photoluminescence and lifetime measurements. While the S-doped NWs show excellent optical quality, the Zn-doped ones exhibit very low photoluminescence efficiency with a large amount of interstitial Zn (donors) which degrade the material quality and compensate the Zn acceptor. We found that the amount of interstitial Zn can be significantly reduced by thermal annealing of the NW samples.

Chapter 2

Nanowire photoluminescence for solar cells

This chapter presents the background theory of solar cells, with an emphasis on the optical absorption and the minority carrier lifetime in a semiconductor nanowire. It will be shown that nanowires allow increasing the optical absorption as compared to a thin film solar cell. The different recombination processes, which are important for evaluating the nanowire solar cell performance, are also discussed in detail. Finally, the micro-photoluminescence and time-resolved photoluminescence setups to measure optical properties of single NW are described.

2.1 Introduction

In one hour time, more solar energy hits the Earth than the total energy consumed by humanity in a full year. In fact, the sun is the most abundant energy resource, which surpasses all the other renewable and fossil-based energy sources [70]. In the inevitable transition from our current level of dependence on depleting fossil fuels and to reduce the consequences on global environment and energy security, solar electricity – or photovoltaic technology – is increasingly important as a potential approach for widespread sustainable energy production. While the resources for photovoltaic conversion are tremendous, the current solar energy's contribution to the entire energy portfolio is still modest. To make photovoltaics a primary source, solar energy need to be captured, converted, stored and distributed in a cost-effective fashion. This imposes both challenges and opportunities for science and technology to seek for ultralow cost and highly efficient solar energy breakthroughs.

The current solar cell market is dominated by single junction panels made of crystalline and polycrystalline silicon, which efficiencies are in the order of 15-20 %. The best laboratory solar cells have efficiencies of 25% for silicon, 22.1% for InP, and 28.8% for GaAs. Those values are close to theoretical conversion efficiency limit, also known as the Schockley-Quiesser limit [71] for an optimal single bandgap solar cells of 31%. The relatively small maximum efficiency for a single junction solar cell is mainly because photons with a smaller energy than the bandgap are not absorbed, whereas photons with higher energy than the bandgap release their excess energies as heat to the lattice. All useful energy that can be extracted into the external circuit is approximately equal to the bandgap energy [71]. The best efficiencies for various types of solar cell recorded by NREL are presented in figure 2.1.

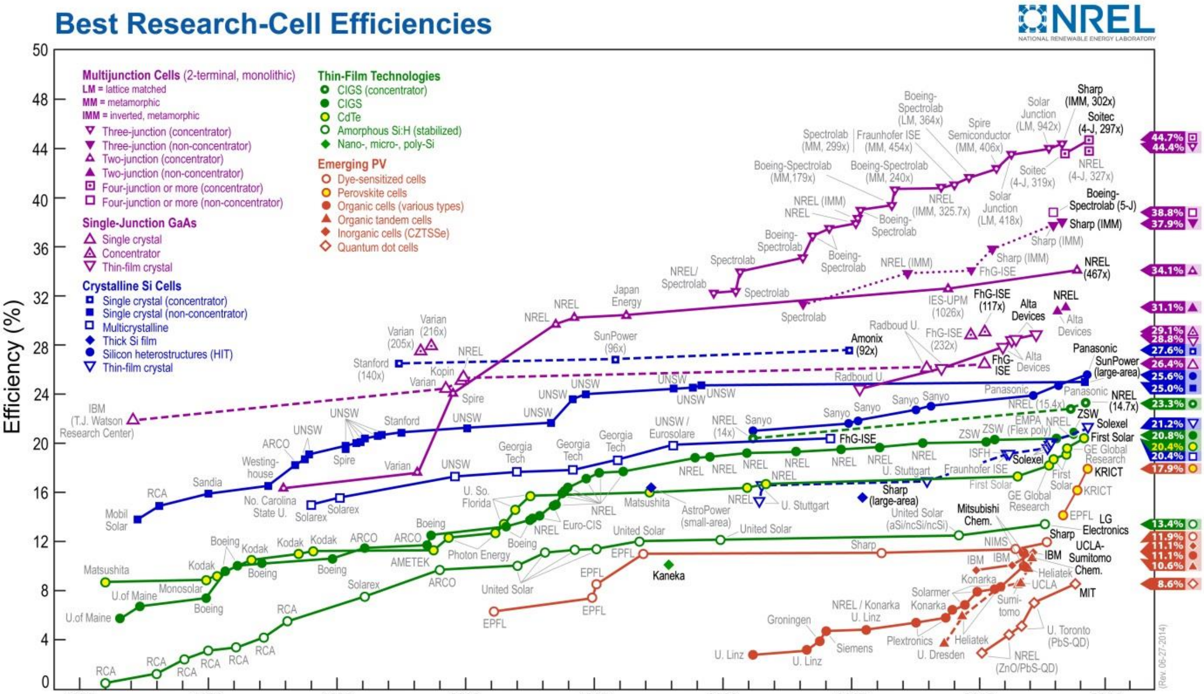

Figure 2.1. World record efficiencies of various photovoltaic technologies (NREL 2014)

Shockley and Queisser described the limiting efficiency for a single junction solar cell, but the maximum solar cell efficiency can be strongly increased when materials with different bandgaps are combined in a multi-junction cell [32]. Figure 2.2 illustrates the part of solar energy, which can be theoretically converted into electricity by single and multi-junction cells. Thermal energy losses of hot carriers are reduced by the use of higher bandgap energy materials for the top p-n junctions. The lower energy parts of the solar spectrum are absorbed by the lower-bandgap bottom p-n junctions. The record efficiency is reached in III-V multi-junction solar cells. By absorbing a broader solar spectrum range, multi-junction solar cells have achieved a record efficiency of 44.7% measured at a concentration of 297 suns for a III-V four-junction solar cell [72]. The improvement of the efficiency of III-V multi-junction cells requires precise current matching for each of the individual junctions, which in turn requires a well-defined bandgap for each junction material. The stacking of semiconductors with different bandgap on the same semiconductor substrate is usually severely limited due the requirements on lattice-matching in thin film cells. Multi-junction solar cells are also too expensive (≈ \$6 per cm2 of cell area) [73] for rooftop application without using solar concentration.

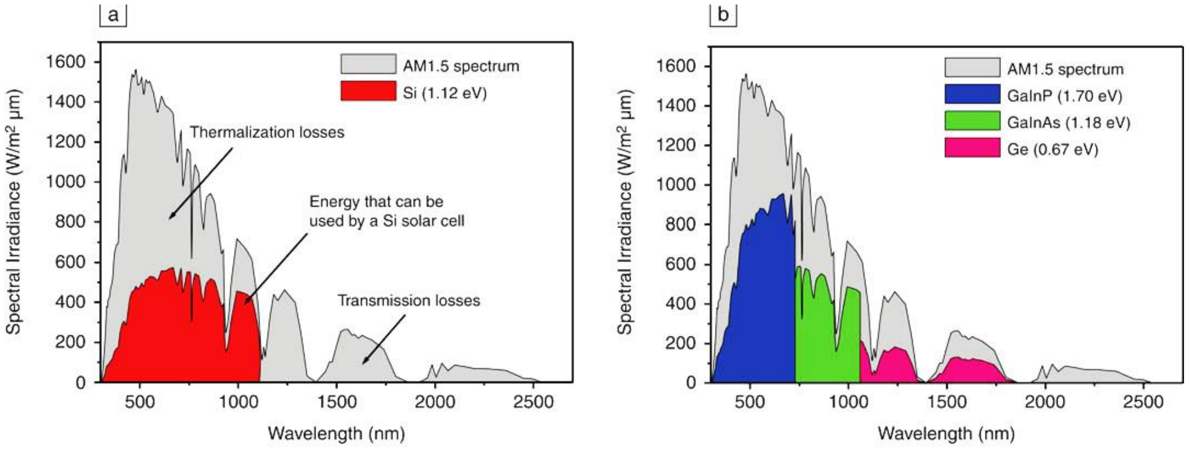

Figure 2.2. The AM1.5 solar spectrum and the portion of the spectrum that can be used by (a) Si solar cells and (b) $Ga_{0.35}In_{0.65}P/Ga_{0.83}In_{0.17}As/Ge$ solar cells (adapted from [74]).

Nanowires (NWs) have emerged as a promising class of materials for high efficiency, low cost solar cells [6, 60, 75, 76]. For instance, thanks to the elastic strain relaxation, NWs enable the fabrication of almost unlimited combinations of semiconductor materials for multi-junction cells [8], with bandgaps matching the entire solar spectrum. This is expected to strongly relax the difficulties for obtaining current matching between each subcell. Furthermore, NW solar cells consume much less material as compared to their thin film counterparts. They can also be epitaxially grown on inexpensive substrates such as silicon [35-40] allowing to further reduce the cost. In order to achieve high-efficiency solar cells, many requirements must be simultaneously met, including a perfect crystal phase, a low surface recombination velocity, the absence of unintentional sidewall growth and very low residual doping levels. In the next section, we will examine different optical processes, which are important for the optimization of material quality of NW solar cells.

2.2 Optical phenomena in nanowire solar cells

The basic four steps needed for photovoltaic energy conversion for any type of solar cells are [77-79]

1. Efficient light absorption, which results in transitions in the absorbing materials from the ground state into an excited state, which is an electron-hole pair in a semiconductor. At this stage, it is important to efficiently convert all solar photons into electron-hole pairs, without suffering from reflection losses or insufficient light absorption.

2. The conversion of the electron-hole pair into free negatively (electron) and positively (hole) charged carriers. At this stage, one of the carriers is a minority carrier which is extremely vulnerable to nonradiative recombination before it reaches the depletion region. At this stage, it is thus important that the minority carrier diffusion length is sufficiently long for efficient diffusion of all photo-generated minority carriers to the depletion region.
3. Separation of the photo-excited carriers in the depletion region. The separated majority electrons subsequently move toward the cathode, and the majority holes move to the anode. They finally release their useful energy at the electrical 'load'.

In the following section the light absorption efficiency and the processes that determine the minority carrier diffusion length will be discussed in more detail.

2.2.1 Absorption, reflection and scattering processes

The absorption of electromagnetic radiation in a semiconductor is due to interband (or band to band) transitions, creating free electron-hole pairs. In a direct bandgap semiconductor, the onset of the band-to-band transition is marked by a sharp increase of the absorption coefficient, $\alpha \propto (\hbar\omega - E_g)^{1/2}$, and for an indirect transition, $\alpha \propto (\hbar\omega - E_g)^2$ [80]. In direct bandgap semiconductors, the rise of the absorption coefficient at the absorption edge is steeper due to higher probability of interband transitions, than in indirect semiconductors, where the optical transition requires the assistance of a phonon. This is very important for photovoltaics where a large light absorption coefficient is essential for efficient energy conversion. Silicon (indirect bandgap) solar cells are typically hundreds of micrometers thick. If it was much thinner, the light especially in infrared region will not be efficiently absorbed. In a planar geometry, carriers have to travel a distance related to the light absorption length to reach the contacts. For efficient charge collection the carrier diffusion length needs to be considerable larger than the thickness of the solar cell. The solar cell efficiency made of indirect semiconductor is thus limited by the tradeoff between the absorption and charge collection efficiency. On the other hand, thin-film solar cells are made of direct band gap materials (such as CdTe, CIGS or CZTS, GaAs), which absorb the light in a much thinner region, and consequently can be made with a very thin active layer often on the scale of a few micrometers thickness. Light impinging on a solar cell device can also be reflected. This is due to the refractive index contrast between air and the semiconductor materials. Abrupt InP and GaAs surfaces reflect more than 30 % of light at normal incidence [81, 82]. That is why anti-reflection coatings are needed to reduce the reflection losses in a thin film solar cell.

Recently there has been an increasing interest in the enhancement of the light absorption in solar cells by using nanostructures. Semiconductor NWs and NW arrays, for instance, can interact strongly with incoming light due to their large geometrical aspect ratio and their periodic arrangement on the substrate [83-88]. A single NW standing on a substrate shows a self-concentration effect [49], with an optical absorption cross section much (~ 10 times) larger than its geometrical size. InP NWs have been shown to absorb 94 % of the incident light while covering only 10 % of the underlying surface [89].

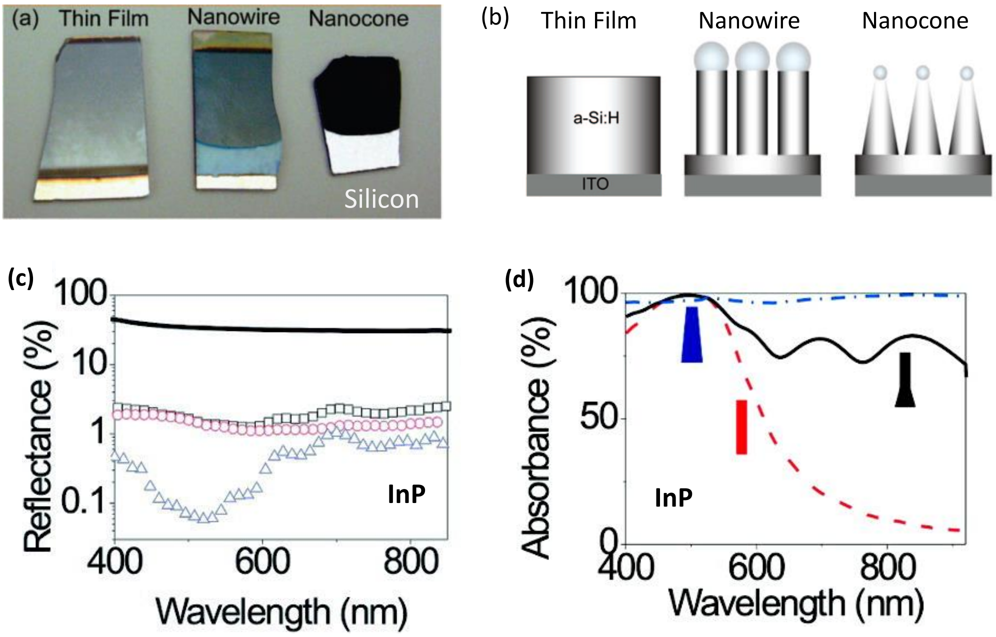

Figure 2.3. (a) Photograph of a-Si:H thin film, a nanowire array and a nanocone array and (b) their schematic illustration (adapted from reference [87]). The absorption measurements from those samples show that the nanocone sample absorbs 93% of incoming light in the range of 400-650 nm. (c) Measured total reflectance (black squares), nonspecular reflectance (red circles), and specular reflectance (blue triangles) of a InP nanowire array sample as a function of wavelength for an angle of incidence of 8^{o} (adapted from reference [86]). The InP nanowires have diameter at top of 90 ± 5 nm with a length of 2 µm, and a tapered lower part with a length of ~1 µm. The diameter of the nanowires at the bottom is 270 (±20 nm). The solid curve shows the measured total reflectance of bulk InP. (d) Simulated absorbance of base-tapered InP nanowires (black solid curve), cylindrical nanowires (red dashed curve), and conical nanowires (blue dashed-dotted curve) for normal incidence [86].

Conical or tapered NWs with a small diameter at the tip and large diameter at the base, provide a graded effective refractive index which results in a strongly reduced reflection and enhanced absorption. Theoretical calculations and experimental results [86-88] show that in this geometrical configuration, a light absorption of more than 98 % percent can be attained. Figure 2.3(a-b) show a photograph and the corresponding illustration of a 1 µm thick amorphous Si:H thin film sample (left), a NW array (middle) and a nano-cone array (right) which have been reported in Ref [87]. The experimental data show that the nanocone sample absorbs 93% of incoming light in the range of 400-650 nm. In contrast, the thin film made of the same material is highly reflective, absorbing only 64

% of the light. The NW sample without tapering shows 75% absorption in the same wavelength range. In another work, the experiment and simulation results on tapered InP NWs array also reveal a strong reduction of the reflection and enhanced absorption, as seen in figures 2.3(c-d). Those studies reveal a great potential for NW structures in photovoltaic applications.

2.2.2 Recombination and trapping of carriers

The performance of a solar cell depends mainly on the minority carrier dynamics. When light is absorbed, minority carriers are generated [77]. The photogenerated carriers have to diffuse to the p-n interface (depletion region) and must be separated by the built-in field for harvesting them in the external circuit. However, photogenerated carriers can get lost before they are collected at the electrodes by mainly 3 different processes: 1) radiative recombination, 2) nonradiative recombination via a localised state in the forbidden gap releasing phonons; this mechanism corresponds to the well-known Shockley-Read-Hall recombination [90, 91]. Surface recombination which is a very important loss mechanism in NWs, can also be mathematically described in terms of the SRH model [92]. 3) Electrons can also relax their energy by transferring it to another electron or hole through an Auger process [93] (Auger recombination). The illustration of the three recombination processes is presented in figure 2.4.

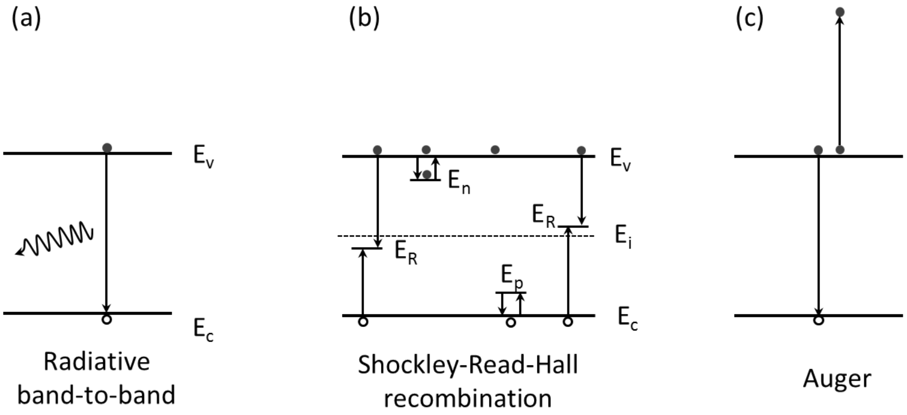

Figure 2.4. Schematic diagram of (a) radiative band-to-band recombination, (b) Shockley-Read-Hall recombination and (c) Auger recombination. E_n and E_p are shallow trap levels and E_R is a deep trap level.

Based on the ABC rate equation [94-97], the recombination rate R(n) and the PL lifetime (τ) are determined by

$$R(n) = \frac{n}{\tau} = An + Bn^2 + Cn^3 \tag{2.1}$$

where n is the carrier density, A, B and C are SRH (including the surface recombination), radiative, and Auger coefficients and n is the carrier density. This equation implies that the SRH and surface recombination are linear with the injection level. The Auger recombination rate is proportional to the third power of the carrier concentration and the band-to-band radivative recombination is proportional to the square of the carrier concentration. Therefore, at a low injection level, SRH and surface recombination are most important, while Auger recombination is expected to become dominant at high carrier density.

2.2.2.1 Radiative recombination

Radiative recombination takes place when an electron in the conduction band recombines with a hole in the valence band, releasing the excess energy as a photon $h\nu \sim E_g$ (photoluminescence). The spontaneous radiative recombination rate R_s is defined as the number of spontaneous recombinations per second in unit volume which can be expressed by an integral:

$$R_s = \int_0^\infty r_s(\hbar\omega)d(\hbar\omega) = \int_{E_g}^\infty r_s(\hbar\omega)d(\hbar\omega) \tag{2.2}$$

where r_s is a spectral function for spontaneous recombination and $\hbar\omega$ is the energy of emitted photon. A standard quantum mechanical calculation (given in reference [98]) yields the following expression of the spectral function

$$r_s = \frac{e^2\sqrt{\epsilon}\hbar\omega}{2m_0^2\pi^3c^3\hbar^2}\mathbf{M}^2 \int \mathrm{d}\mathbf{k}_c^3\mathrm{d}\mathbf{k}_v^3 f(E_c)[1 - f(E_v)]\delta(\mathbf{k}_c - \mathbf{k}_v)\delta(E_c - E_v - \hbar\omega). \tag{2.3}$$

where $\sqrt{\epsilon}$ is the refractive index, m_0 is the free electron mass, $\mathbf{k}_\mathrm{c}$ and $\mathbf{k}_\mathrm{v}$ are the electron and hole wave vector, E_c and E_v are electron and hole energies, f is the Fermi-Dirac function ($f = \left\{1 + \exp\left[\frac{E-\mu}{k_BT}\right]\right\}^{-1}$) with μ the chemical potential. The matrix element **M** [98] is given by

$$\mathbf{M}^2 = \frac{1}{4\pi}\sum_{\lambda=1}^{2}\int \mathrm{d}\Omega_\mathbf{k}|\mathbf{e}_{\mathbf{k}\lambda}.\mathbf{P}_{cv}|^2,$$

where $\mathbf{e}_{\mathbf{k}\lambda}$ is the polarization vector of the photon with the momentum **k.** The integration is over all photon momentum directions, the sum is over the two polarizations, and $\mathbf{P}_{cv}$ is the interband transition matrix element at the Γ point.

By using anisotropic band energy dispersion in the parabolic approximation for both the conduction and valence bands, we obtain

$$E_c - E_v = E_g + \frac{\hbar}{2}\left(\frac{k_x^2}{\mu_x} + \frac{k_y^2}{\mu_y} + \frac{k_z^2}{\mu_z}\right),$$

where $E_g = E_c^0 - E_v^0$, $\mu_x = \left(m_{e,x} + m_{h,x}^{-1}\right)^{-1}$ is the reduced effective mass of an electron-hole pair in the x, y, z direction.

By performing the integration over photon energy and wave vector using the parabolic approximation for a non-degenerate semiconductor $(f(E_c) \approx \exp\left(\frac{\mu - E_c}{k_BT}\right)$ and $[1 - f(E_v)] \approx \exp\left(\frac{E_v - \mu}{k_BT}\right)$), [98] we obtain the spontaneous radiative recombination rate

$$R_s = \frac{e^2\sqrt{\epsilon}}{m_0^2 c^3 \hbar^2}\mathbf{M}^2 \left[\frac{2k_BT}{\pi\hbar^2}\right]^{3/2} \sqrt{\mu_x\mu_y\mu_z} E_g \left[1 + \frac{3k_BT}{2E_g}\right] e^{-\frac{E_g}{k_BT}}. \qquad 2.4$$

The radiative recombination coefficient B is defined from the rate equation

$$R_s = Bnp,$$

where n and p are electron and hole concentration. Using the mass-action law

$$np = 4(m_e m_h)^{\frac{3}{2}} \left(\frac{k_BT}{2\pi\hbar^2}\right)^3 \exp\left(-\frac{E_g}{k_BT}\right)$$

we finally obtain [98]

$$B = \frac{e^2\sqrt{\epsilon}}{m_0^2 c^3 \hbar^2}\mathbf{M}^2 \left[\frac{2\pi\hbar^2}{k_BT}\right]^{\frac{3}{2}} \frac{1}{\sqrt{\overline{m}_x\overline{m}_y\overline{m}_z}} E_g(T) \left[1 + \frac{3k_BT}{2E_g(T)}\right], \qquad 2.5$$

where $\overline{m}_x = m_{e,x} + m_{h,x}$ and so on. It can be see that for the calculation of the radiative recombination coefficient B the matrix element $\mathbf{M}^2$ and the temperature are important parameters.

For simplicity, in many experimental papers [99-101], the following simplified equation for the B coefficient is used

$$B = 3 \times 10^{-10} \left(\frac{E_g}{1.5}\right)^2 \left(\frac{300}{T}\right)^{3/2} = B_0 \left(\frac{300}{T}\right)^{3/2} \ (\mathrm{cm^3 s^{-1}}) \qquad 2.6$$

The value of B is much larger for direct than for indirect bandgap materials. For instance, $B \approx 2 \times 10^{-10}$ cm^3/s for GaAs and is about 1×10^{-15} cm^3/s for silicon at room temperature [92]. A detailed calculation indicates that B also weakly varies with doping level and carrier concentration [102].

If the radiative recombination is the dominant process, the PL decay time (τ) is related to the recombination coefficient by $\tau = 1/Bn$. A study on the temperature dependence of the radiative recombination coefficients and PL lifetime on temperature of GaAs/AlGaAs quantum well structure [103] show that the radiative recombination rate decreases one order of magnitude from 2 x 10^{-9} cm^3/s at 15 K to 1.7 x 10^{-10} cm^3/s at 300 K and the corresponding lifetime increases from 0.4 ns to 5.2 ns. In a nanowire of large enough diameter, the B-coefficient decreases with $T^{-3/2}$ which implies that the nonradiative SRH and surface recombination become dominant at room temperature.

2.2.2.2 Shockley-Read-Hall and surface recombination

Shockley-Read-Hall (SRH) recombination describes a process in which minority carriers are captured into nonradiative recombination centers, located within the forbidden gap [90, 91]. The SRH recombination can be described by the following equation [92]

$$R_{SRH} = \frac{\sigma_p \sigma_n v_{th} N_t [pn - n_i^2]}{\sigma_\mathrm{n}\left[n + n_i e^{\frac{E_t - E_i}{kT}}\right] + \sigma_p \left[p + n_i e^{\frac{E_i - E_t}{kT}}\right]} \ (\mathrm{cm^{-3}s^{-1}}) \qquad 2.7$$

Here, N_t is the volume density of deep trap levels; and σ_n and σ_p are the electron and hole capture cross-sections, repectively. E_t is the energy level of the trap; n and p are electron and hole concentrations; v_{th} is thermal velocity and E_i is intrinsic Fermi level.

The trap level in equation 2.7 can be either a nonradiative recombination center due to an impurity or a crystal defect [104]. The maximum recombination rate occurs at trap levels near midgap. If the energy level E_t lies near E_c or E_v, a captured electron and hole can be thermally activated to the conduction band or to the valence band and R_{SRH} drops many order of magnitudes compared to that of midgap centers.

If the electron-hole pairs are optically injected with a volume density ρ, we obtain an electron density of $n = n_0 + \rho$, and a hole density of $p = p_0 + \rho$. If we define the SRH lifetimes $\tau_p = 1/\sigma_n N_t v_{th}$ and $\tau_n = 1/\sigma_p N_t v_{th}$ and use N for the majority carrier concentration, the SRH recombination rate approximated as

$$R_{SRH} = \frac{[\rho N + \rho^2]}{\tau_{min}[N + \rho] + \tau_{max}\rho} \qquad 2.8$$

Where τ_{min} and τ_{max} are minority and majority carrier lifetime respectively. For low injection $\rho \ll N$, equation 2.8 can be simplified to $R_{SRH} = \rho/\tau_{min}$. Therefore, for low injection levels, the SRH lifetime is determined solely by the capture of minority-carriers into nonradiative recombination centers.

The surface of a semiconductor NW also provides an inherent source of deep-level traps. The surface states are caused by dangling bonds at the surface due to the interruption of the crystal periodicity, or by impurity atoms such as carbon or oxygen. Ahrenkiel presented a calculation for the recombination rate at the surface of a slap of a semiconductor material with a thickness d, assuming that surface states are single level SRH traps [92]

$$R_{vs} = \frac{2}{d} \frac{\sigma v_{th} N_{st} \rho_s}{1 + \frac{2n_i}{N} \cosh \frac{E_t - E_i}{kT}} = \frac{2}{d} R_s = \frac{2S}{d} \rho_s \ (\mathrm{cm^3 s^{-1}}) \qquad 2.9$$

Here, R_{vs} is the volume recombination rate and R_s is surface recombination rate. ρ is the minority carrier density, N_{st} is the surface state density, n_i is the intrinsic density, N is the majority-carrier density, E_t is the energy of the trap, E_i is intrinsic Fermi level at the surface, and S is the surface recombination velocity which is given by

$$S = \frac{\sigma v_{th} N_{st}}{1 + \frac{2n_i}{N} \cosh \frac{E_t - E_i}{kT}} \qquad 2.10$$

Near midgap, equation 2.10 can be rewritten to be

$$S = \sigma v_{th} N_{st} \qquad 2.11$$

In the presence of the surface band bending with a surface potential of V_s ("+/-" sign for downward/upward band bending), the surface recombination can be rewritten as $S = \sigma v_{th} N_{st} \exp(-eV_s/k_B T)$.

In summary SRH and surface recombination rates depend strongly on the density of recombination centers as well as their capture cross-section, and are linear with injection levels. In contrast to the radiative recombination rate, which decreases with increasing temperature, the SRH and surface recombination rates increase with increasing the temperature [105]. For instance, the A coefficient increases from 5.5×10^7 to 1.9×10^8 $\mathrm{s^{-1}}$ from 6 to 300 K for an InGaN/GaN dot-in-a-wire nanoscale heterostructures [97].

2.2.2.3 Auger recombination

Auger recombination is a three body process, in which an electron and a hole recombine and the released energy is transferred to another electron or hole (Figure 2.3). The net Auger recombination rate can be expressed as

$$R_{Aug} = C_n(pn^2 - nn_i^2) + C_p(np^2 - pn_i^2) \qquad 2.12$$

Here, R_{Aug} is the Auger recombination rate, C_n and C_p are the Auger coefficients, which represent the energy transfer rate of the minority carriers. Auger processes are most dominant when the carrier concentrations are high, such as in a low bandgap semiconductor, in highly doped materials, or at very high excitation. For the same reason, Auger recombination becomes more important in indirect semiconductors such as silicon than in direct semiconductor (due to slow radiative recombination in indirect bandgap materials). The minority carrier lifetime in intrinsic crystalline silicon is dominated by the Auger process at injection levels exceeding 1×10^{17}cm^{-3}. The Auger recombination process is also relevant at high electrical injection levels in lasers or LEDs [92]. Measurement of the Auger coefficient by a variety of techniques has yielded values in the range of 0.35-2.0 x 10^{-30} cm^6/s for GaN and InGaN [97], and 4 x 10^{-29} cm^6/s for an In$_{0.4}$Ga$_{0.6}$As/GaAs quantum dot. For the NW geometry, the Auger recombination rate in GaN/InGaN heterostructures was found to be of several order of magnitude smaller (~10^{-34} cm^6/s) than in bulk due to lower amount of defect-assisted Auger recombination in a NW [95, 97]. For bulk InP, the Auger recombination was found to be 9 x 10^{-31} cm^6/s [81]. The Auger coefficient for InP NWs has not been reported so far.

2.2.2.4 Minority carrier lifetime in semiconductor nanowires

We now discuss which parameters determine the minority carrier lifetime. We express the photogenerated carrier concentrations per unit volume at the time t as $\Delta n(r,t) = n(r,t) - n_0$ for the electrons and $\Delta p(r,t) = p(r,t) - p_0$ for the holes. The solution for $\Delta n(x,t)$ is derived by solving the time-dependent continuity equation. The continuity equation can be reduced to a time-dependent diffusion equation for quasi-neutral or field-free regions.

$$\frac{\partial \Delta n(r,t)}{\partial t} = D\nabla\Delta n(r,t) - \frac{\Delta n(r,t)}{\tau} \qquad 2.13$$

Here, D is the minority carrier diffusion coefficient, and τ is the recombination lifetime. The minority-carrier density depends on both the minority-carrier lifetime and the diffusion rate out of the active region. The minority-carrier density is therefore structure dependent.

For semiconductor NWs, we assume that the geometry is approximated by a cylinder of infinite length. To calculate the surface recombination velocity, we follow the methods derived in references [106] and [107]. The continuity equation describing the carrier concentration profile is given by

$$\frac{\partial \Delta n(r,t)}{\partial t} = D\frac{\partial^2 \Delta n(r,t)}{\partial r^2} - \frac{\Delta n(r,t)}{\tau_{bulk}} \qquad 2.14$$

Where r is the radial coordinate and τ_{bulk} is the electron lifetime within the bulk volume of the NW. The net flow of carrier toward the surface, which is equal to normal component of the classical diffusion $-D\frac{\partial \Delta n(r,t)}{\partial r}$, should be equal to the surface recombination rate. Therefore equation 2.14 is subjected to the following boundary condition [108]

$$D\frac{\partial \Delta n(r,t)}{\partial r}|_{r=r_0} = -S\Delta n(r_0,t) \quad 2.15$$

Where r_0 is the diameter and S is the surface recombination velocity of the NW. The solution of this equation is given by an exponential time decay of the carrier density, with a lifetime

$$\frac{1}{\tau} = \frac{1}{\tau_{bulk}} + \lambda(S,D,r) \quad 2.16$$

which satisfies

$$D\lambda J_1(\lambda r_0) = J_0(\lambda r_0), \quad 2.17$$

Where J_0 and J_1 are 0^{th} and 1^{st} order Bessel functions of the first kind. For $S \ll D/r$ one can use the small argument behavior of the Bessel functions ($J_n(\beta) = \beta_n/2^n n!$). We have $J_0(\beta) = 1$, $J_1(\beta) = \beta/2$. By using this approximation, equation 2.16 can be simplified to

$$\frac{1}{\tau} = \frac{1}{\tau_{bulk}} + \frac{2S}{r_0} = \frac{1}{\tau_{bulk}} + \frac{4S}{d} \quad 2.18$$

Where d $(= 2r_0)$ is the diameter of the NW. The total recombination rate is therefore strongly determined by the surface recombination velocity and the NW diameter. The details of the recombination processes within the bulk volume of the NWs (τ_{bulk}) as well as the surface recombination velocity (S) will be discussed in the following sections

2.2.2.5 Summary of the main recombination processes in nanowires

Due to small dimensions and very high aspect ratio compared to bulk or a thin film, a NW is very sensitive to the surface and surrounding environment, which is good for sensor applications. For photovoltaic applications, however, the surface recombination velocity can be detrimental for the minority carrier lifetime. As presented earlier in this chapter, the minority carrier lifetime in a NW can be rewritten as

$$\frac{1}{\tau} = \frac{1}{\tau_{bulk}} + \frac{4S}{d} = \frac{1}{\tau_r} + \frac{1}{\tau_{nr}} + \frac{1}{\tau_s} \quad 2.19$$

Where τ_r the radiative band-to-band recombination time, τ_{nr} is the nonradiative recombination time due to SRH or Auger processes and τ_s is due to the surface recombination.

In order to evaluate the role of each recombination processes, we assume that the NWs, which are used for a NW solar cell have a cylindrical geometry with 100 nm diameter, 2 um length and a surface recombination velocity $S = 5 \times 10^3$ cm/s. The resulting lifetime due to the contribution from surface recombination is then $\tau_s = 0.5$ ns. From equation 2.19, the minority carrier lifetime is shorter than τ_s. Since the room temperature PL lifetime of a III-V semiconductor such as InP and GaAs is in the range of tens of ns to a few µs, the short lifetime due to surface recombination is expected to limit the performance of NW based devices such as solar cells or LEDs.

Surface passivation is important for NW photovoltaics. For instance, GaAs is normally subject to very high surface recombination (10^6 cm/s), which will result in a picosecond minority carrier lifetime. This lifetime is too short so that the diffusion length $L = \sqrt{\tau D}$ ~ 100 nm (assuming a diffusion constant of D = 100 cm^2/s [109]), which is not enough for the minority carriers to efficiently diffuse to the depletion region. By capping a GaAs NW with an $Al_xGa_{1-x}As$ shell, as commonly done in double herterostructures, the minority carrier lifetime can be substantially increased, up to a few ns. For InP, the effect of the surface is less detrimental. InP NWs can emit brightly at room temperature even without any surface passivation. A recent work by the Jagadish group [110] suggests an ultra-low surface recombination velocity of 170 cm/s in InP NW with WZ/ZB mixed phases measured by optical-pump THz probe technique. The conductivity carrier lifetime is measured to be 1ns, even while the PL lifetime is in the range of 30 ps. However, it should be mentioned that this measured low surface recombination rate is due to the fact that electron and holes are quickly spatially separated and trapped to thin ZB and WZ layers, respectively. However, this kind of carrier trapping is localized and will also reduce the carrier mobility [111, 112] and thus degrade the performance of a NW solar cell. Very recently, the PL lifetime of pure WZ NWs (diameters of 200-400 nm) reported by the same group is ~ 1.5 ns at room temperature [113]. However this lifetime is still an order smaller than that of the bulk InP (20-40 ns) [114].

2.3 Measurement of photoluminescence and carrier lifetime

The external luminescence efficiency is an indicator for the internal optical losses at open-circuit condition in a solar cell [71]. In this thesis we use photoluminescence (PL) and time resolved PL (TRPL) measurement techniques to study the optical quality of single NWs and ensembles of NWs for solar cell applications.

The PL emission of a semiconductor NW contains a wealthy source of information about the material properties, such as the carrier lifetime, the bandgap energy, the quasi-Fermi level splitting, and the impurity levels [115, 116]. A PL measurement is a very efficient, contactless and nondestructive method to examine the optical properties of a semiconductor NW at different stages of development. In this thesis we extensively use micro-photoluminescence (μ-PL) and time-resolved photoluminescence (TRPL) measurements to study the structural and optical properties of various semiconductor NWs.

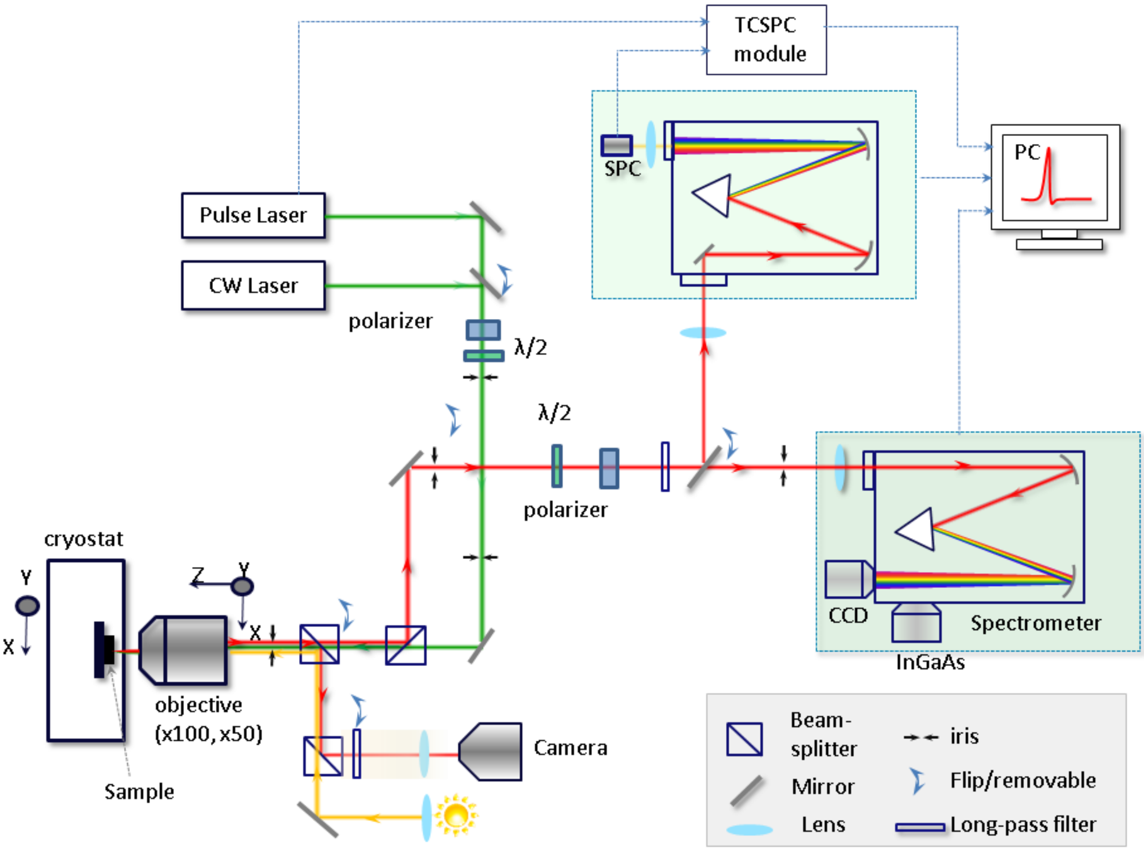

Figure 2.5. Schematic of the micro-photoluminescence (PL) and time-resolved PL (TRPL) setup. Samples are mounted in the optical cryostat. The live video recorded by the camera allows us to find and focus the laser spot on a single nanowire. The PL signal is excited and collected by the same microscope objective. The time-integrated PL spectra are measured by CCD or InGaAs array detector and the TRPL is measured by a single photon detector (SPC) connected to a time-correlated single photon counting module (TCSPC).

A schematic of our μ-PL setup is shown in figure 2.5. Long working distance 0.45/0.7NA objectives with 50x/100x magnification are used to image the NWs. The NW sample is loaded into a He flow optical cryostat. The cryostat is mounted on a x-y translation stage for rough positioning and the objective is mounted on a piezoelectric actuators driven stage for fine positioning in x, y, and z directions with an accuracy of 30 nm. Various laser sources are used for PL studies including continuous wave (CW) diode lasers operating at 405 nm, 532 nm, 632 nm as well as pulsed lasers with repetition rates of 5, 10, 20, 40, 80 MHz and a wavelength of 420 nm and 635 nm. For some experiments, a tunable Ti-Sa laser is used. The image of the NW is projected on the entrance slit of a triple grating SP2500A (50 cm) or SP2300i (30 cm) spectrometers (Princeton Instruments).

The SP2500 is equipped with a 2014x512 pixels electrically cooled CCD camera and a liquid-nitrogen-cooled InGaAs detector array. The CCD detection wavelength is in the range from 200nm to 1000 nm and the InGaAs detector works efficiently in 1000-1700 nm spectral window. These detectors are used for PL imaging and time-integrated PL measurement.

In order to perform the PL measurement on individual NWs, we transfer the NW to a host substrate such as SiO_2 wafer or a TEM grid. The samples are first checked with an optical microscope (figure 2.6a) and then mounted onto the cold finger of the cryostat. A camera is used to record live video from the optical microscope, which allows us to easily find and focus the laser spot (with a size of about 1 μm) on individual NWs, with the help of the piezoactuators. The laser spot can also be scanned along the NW axis to measure the PL from different parts of a single NW. The optical image of the NWs and laser spot recorded by our PL setup is shown in figure 2.6(b).

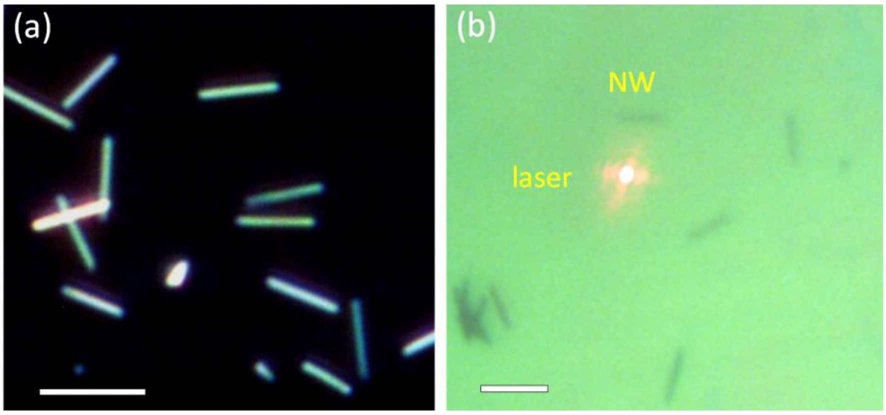

Figure 2.6. (a) Dark-field optical microscopy image of InP nanowires horizontally transferred to a SiO_2 substrate. (b) Bright field image of a number of nanowires and the laser spot (~ 1 μm) taken by the camera of our micro-photoluminescence setup. The scale bars are 5 μm.

The time-resolved photoluminescence (TRPL) measurements are carried out by using a time-correlated single photon counting (TCSPC) module. This module measures the time delay between the sample excitation by a laser pulse and the arrival of the emitted photon at the single photon detector (SPD). TCSPC requires a defined “start”, provided by the electronics steering the laser pulse or a photodiode, and a defined “stop” signal, realized by detection with single-photon sensitive detectors [117]. The measurement of this time delay is repeated many times and the delay times are sorted into a histogram that plots the time distribution of the emission after the excitation pulse. In this thesis a 50 x 50 μm^2 single photon avalanche photodiode (SPAD from Picoquant) is employed. The output signal is sent to channel 1 of a Picoharp 300 TCSPC module. The trigger signal (channel 0) comes from the pulse laser. The total resolution of the system is 100 ps.

Chapter 3

Improving material quality of InP nanowires for solar cells

This chapter discusses the approach to obtain high material quality InP nanowires for solar cells. First we focus on crystal phase purity by using different growth parameters such as the size of the catalyst nanoparticle and the growth temperature. In order to improve the optical and electrical properties of the InP nanowires, high temperature growth is employed in combination with HCl in situ etching. This dramatically reduces the incorporation of impurities and suppresses nanowire tapering. A minimal amount overgrowth on the sidewall of the NWs (even with the use of HCl in-situ etching) can finally be removed by post growth cleaning using piranha etching. These steps are essential for the fabrication of high efficiency nanowire solar cells.

3.1 Introduction

Direct bandgap III-V semiconductors are widely used for numerous optoelectronic applications. III-V semiconductor nanowires (NWs) have recently been extensively investigated as a platform for high performance devices [118] including solar cells [6, 76, 8, 62, 57, 56, 119, 120], nanolasers [113, 121-123], light-emitting diodes [124, 125] and sensitive photodetectors [4, 126]. One important advantage of NW structures is that they have small dimensions, which allow them to accommodate strain better than planar structures. Therefore, the lattice-matching constraint is strongly reduced when we combine different semiconductor materials within a single nanowire, as required for a tandem NW solar cell. According to a theoretical calculation [127], tandem NW solar cells with multiple axial junctions in the lattice-mismatched system can achieve energy-conversion efficiencies of over 50 %. Moreover, it enables the integration of III-V materials with existing silicon technology. NWs also use much less expensive material compared to bulk or thin film counterparts and therefore they can thus strongly reduce the material cost.

Despite the abovementioned advantages, the bottom-up growth of semiconductor NWs usually leads to lower material quality compared to that of thin film or bulk growth. NWs often contain random stacking faults, incorporate higher amount of unwanted impurities (MOVPE growth), and are subject to high surface recombination velocity due to high surface to volume ratio. For most of optoelectronic applications, excellent material quality is essential to obtain high device performance. The material quality and the control of the growth of NWs are currently the main challenges which limit the efficiency of the NW devices as compared to their planar counterparts. Therefore, improving the NW material quality is an important step toward high efficiency NW solar cells.

InP NWs are a good candidate for high-efficiency solar cells and other optoelectronics devices since InP has a very low surface recombination velocity and an ideal band gap energy. Many recent efforts were devoted on the growth of high quality InP NWs, especially on the perfection of crystal phase and the control of the morphology, the doping levels, and the elimination of unwanted impurities. In this chapter, we focus on several key aspects to improve the material quality for high efficiency NW solar cells, including the elimination of crystal phase defects, the reduction of unwanted impurity and tapering, and the surface cleaning passivation. We demonstrate that these steps are essential for high performance NW photovoltaic devices.

3.2 Experiment

In our studies, InP NWs wires are grown by vapour-liquid-solid (VLS) mechanism on (111) and (100) InP substrates in metalorganic vapor phase epitaxy reactors (Aixtron 200 or Aixtron CCS) by using Au catalysts. Various growth parameters such as the size of Au seeds, the growth temperature, and the V/III ratios were investigated. The growth temperature is varied in the range from 420 °C to 560 °C. The detailed growth conditions will be mentioned for each batch of samples in the next sections.

The morphology and growth direction of NWs are examined by using scanning electron microscopy (SEM) and the crystal structure and quality of single NWs are investigated by transmission electron microscopy (TEM). To study the optical properties of the NWs, we use micro-photoluminescence (μ-PL) and PL lifetime measurements. Those measurements give us insights into the material quality of the NWs and therefore provide us an effective way to optimize the growth of high efficiency NW solar cells. In order to perform micro-photoluminescence (μ-PL) and PL lifetime measurements NWs are transferred to a thermally oxidized Si wafer. The samples are then mounted on a cold finger of an optical flow cryostat which allows us to vary the temperature from 4 K to 300 K. The PL emission is excited and collected through a 100x long working distance objective with numerical aperture of NA = 0.7. A continuous-wave diode laser (635 nm) and a pulse diode laser (635 nm, repetition rate in the range 5-80 MHz) are used as excitation sources. The time-integrated PL is detected by an electrically-cooled CCD camera and the PL lifetime is measured by a single photon avalanche photodiode (SPAD) connected to a time-correlated single photon counting (TCSPC – Picoharp 300) module. The final timing resolution of the system is 100 ps.

3.3 Improving material quality of InP nanowires for solar cells

3.3.1 Structural and optical properties of InP nanowires

Bottom-up III-V semiconductor NWs grown by VLS method are usually polytypic, with successive arrangements of zincblende (ZB) and wurtzite (WZ) crystal phase segments along their axis [128]. The atomic stacking sequence of ZB along the <111> direction is AaBbCcAaBbCc (or ABCABC) and of WZ along the <0001> direction crystal structure is AaBbAaBb (ABAB) as illustrated in figure 3.1 (a). There are two common crystal defects in NWs: twins and stacking faults. Twins are formed as the interface between two ZB segments mutually rotated by 60° around the <111> growth direction. The twin plane (TP) can also be regarded as a single monolayer of WZ. Periodic arrangement of TPs along <111> direction in a NW is called ZB twinning superlattice (ZB-TSL), as illustrated in figure 1(c). A stacking fault refers to the local interruption of the regular stacking sequence, where the regular stacking sequence continues after each stacking fault. Figure 3.1(b) and (c) show schematically a ZB InP stacking fault in a WZ NW and a ZB twinning superlattice structure.

Due to the difference in electronic band structures of ZB and WZ phases, the optical and electrical properties of the two are different. Theoretical calculations and experimental studies show that WZ InP has a zero temperature bandgap energy of about 1.504 eV, which is higher than that of the ZB InP (1.42 eV) [129, 130]. The two crystal phases show type II band line-up with band offsets shown in figure 3.1(b). The PL spectra of a ZB and a WZ InP single NW are presented in figure 3.2(a). It can be seen that the WZ NW exhibit a dominant free exciton peak at 1.494 eV (FWHM =11.6 meV) and ZB at 1.415 eV (FWHM of 9.5 meV). A donor-acceptor (D-A) impurity peak at about 35-40 meV below the bandgap peaks are clearly observed for both types of NWs. Those impurity peaks are often pronounced at low excitation power (~ 1 W/cm^2) and become saturated at high excitation, normally above 100 W/cm^2, depending on the sample quality. The relative intensity of the bandgap peak with respect to the D-A peak as well as their PL linewidths can provide us useful information about the crystal phase and the impurity level within the NWs.

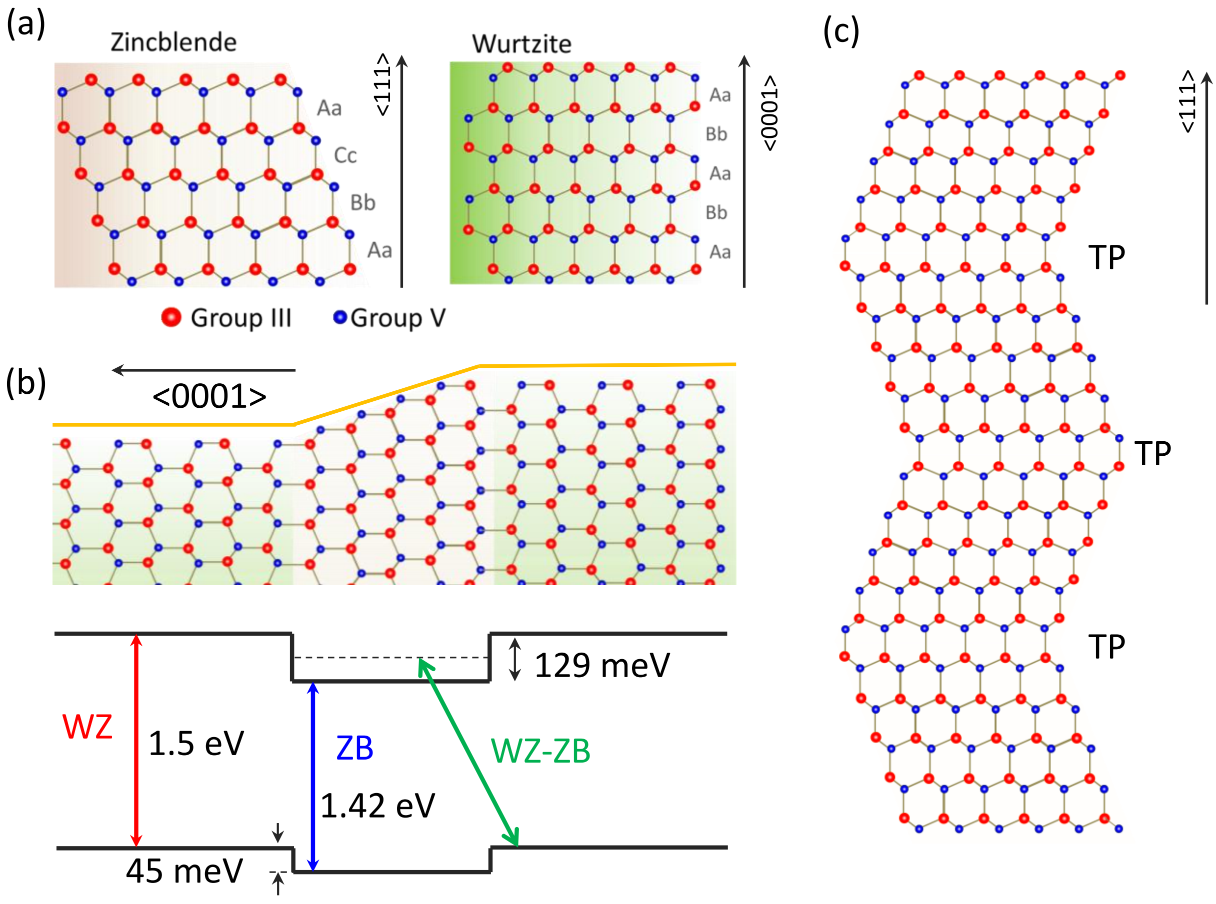

Figure 3.1. Schematics of (a) zincblende and wurtzite crystal structures, and (b) thin zincblende stacking fault in wurtzite InP. The corresponding band diagram is shown below. (c) Zincblende twinning superlatice (ZB-TSL) containing a periodic sequence of twin planes (TPs).

A type II band alignment between WZ and ZB is predicted. This leads to trapping of electrons (holes) in WZ (ZB) stacking faults in mixed phase InP NWs and type II transition across the ZB-WZ interface, as indicated in figure 3.1(b). According to theoretical predictions these transitions have energies ranging from 1.371 eV to 1.545 eV depending on the band line-up between WZ and ZB InP [129, 131]. In our experiment, the typical energy of such transition is in between the ZB and WZ bandgaps as seen in figure 3.2. A type II transition has a lifetime in the range from a few to tens of nanoseconds [131, 132], which is about one order of magnitude higher than that of the WZ and ZB free exciton peaks due to the spatial separations of electron and holes at both sides of the ZB-WZ interfaces.

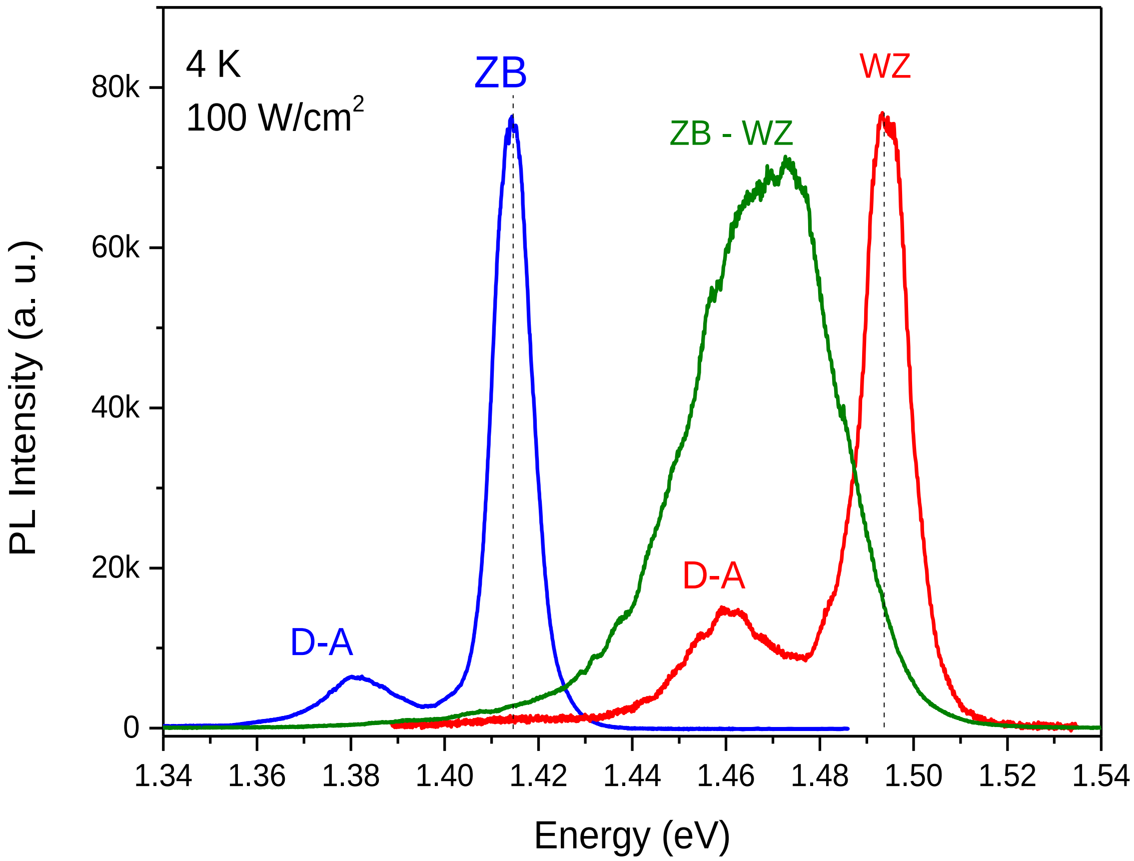

Figure 3.2. Low temperature PL spectra of a single zincblende (ZB), a single wurtzite (WZ), and a single ZB-WZ mixed-phase InP NW at an excitation density of 100 W/cm^2. The PL from ZB and WZ shows bandgap related emissions and impurity related (D-A) peaks at about 35-40 meV below the bandgap peaks. The mixed-phase WZ-ZB NW shows a broad emission in between the WZ and ZB band gap. This is due to type II band alignment between the two crystal phases.

For solar cell applications, the uncontrolled crystal phase mixtures can strongly affect the performance of the devices. Both theoretical and experimental work has shown that twins and stacking faults can induce trapping [111, 131] and scattering of both charge carriers [133-135] and phonons [136]. For instance, the carrier mobility of InP NWs is significantly lower than values reported for optimized bulk InP due to enhanced carrier scattering at ZB–WZ boundaries [112, 110] even when the surface recombination is low (170 cm/s) [110]. On the other hand, formation of stacking faults also induces the incorporation of unwanted impurities on the sidewall of the NWs [27, 62]. Therefore, the elimination of stacking fault is important to enhance the carrier mobility [112] and reduce the impurities at the sidewall of the NW.

3.3.2 Crystal phase purity in nanowires

3.3.2.1 Growth temperature dependence of stacking fault density

The crystal structure of a bulk III-V semiconductor depends on its ionic characteristics [128]. A higher ionicity induces larger attracting Coulomb forces and thus favours shorter bond length. The WZ crystal structure is thus favoured for materials with high ionicity (GaN, InN, AlN), and the ZB structure is favoured for other III-V materials (InP, InAs, GaP, GaAs). Materials with moderate ionicity, such as InP, InAs, GaAs, GaP, tend to form stacking faults when they are grown by using metal particle-assisted VLS growth. The reason for the transitions between ZB and WZ is still under debate though. Recently, extensive efforts have been devoted to achieve pure and controlled crystal phase <111> NWs. There are several key parameters that affect the crystal phase of an InP NW, including the diameter of the catalyst seeds, the growth temperature, the III-V ratio and the use of dopants.

Both theoretical models and experiment work show that a smaller diameter NW favours the WZ crystal phase. In our studies, when we reduce the size of Au catalyst particle to 20 nm, the crystal structure is mainly WZ with a NW diameter of about 70 nm. A TEM image of an InP NW grown with a 20 nm catalyst at 500 °C is shown in figure 3.3(a). At this growth temperature, the NWs still contain a considerable amount of ZB stacking faults. The number of stacking fault can be reduced further by decreasing the diameter of NW. However, a too small diameter NW is not desirable for a high solar light absorption which is important for a high efficiency solar cell. An alternative approach would be to increase the growth temperature. This has two benefits. Firstly, we can achieve higher quality and more pure crystal phase InP NWs. Secondly, the residual impurity incorporation level will be dramatically reduced at higher growth temperature.

Figure 3.3(a) and (b) present the TEM images of two typical WZ InP NW grown by using 20 nm Au catalysts at same V-III ratio of 400, but at different grow temperatures. The NW grown at 500 °C shows mainly WZ crystal structure with a high number (~ 30 per micron) of stacking faults while the NW grown at 540 °C shows an almost pure WZ structure with only a few stacking faults (~ 0.6 per micron).

The low temperature PL measurements on an ensemble of NWs show a similar trend. The normalized PL spectra of typical InP nanowires from those sample are plotted in figure 3.3(c). As discussed above, the PL linewidth is a good indication of the randomness of the ZB stacking faults in a WZ InP NW. When the growth temperature increases from 480 °C to 540 °C, the PL line width decreases from 55 meV down to 10 meV. A higher growth temperature is thus a viable approach to eliminate stacking faults in WZ InP NWs. The growth temperature also strongly affects the photoluminescence efficiency and the photoluminescence lifetime of the NWs, which will be discussed later on in this chapter.

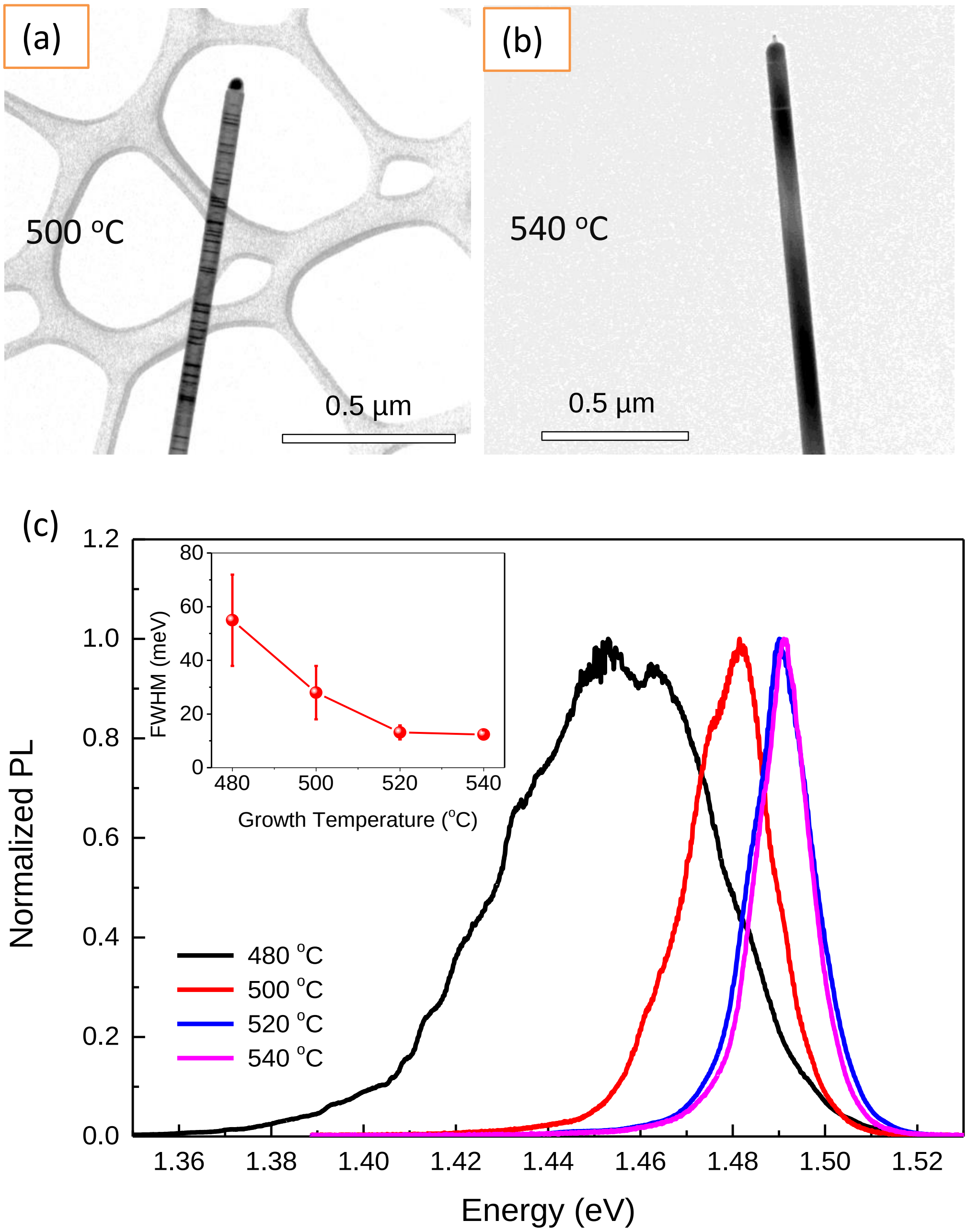

Figure 3.3. TEM images of InP NWs grown by 20 nm Au seeds at (a) 500 °C and (b) 540 °C. NWs grown at 540 °C are almost stacking-fault-free while the one grown at 500 °C still contain a relatively high density of stacking faults. (c) Typical PL spectra of NWs grown at 480, 500, 520 and 540 °C measured at 4K and 105 W/cm^2 excitation density. The inset of (c) shows the corresponding PL linewidths.

3.3.2.2 Exploring alternative growth directions

While the most favorable growth direction of the III-V NWs is <111>B, they can also be forced to grow in different crystallographic direction. This approach can be employed to obtain pure ZB crystal structure for NW grown in <001> direction because it is more difficult to form a rotational twin in this growth direction [137, 138].

A square array of Au particles with a diameter of 50 nm and a pitch of 500 nm was first patterned by electron beam lithography. Our <100> InP NW samples were subsequently fabricated in a horizontal MOVPE system (Aixtron 200) on Sn-doped (100) InP substrates. The growth was carried out at 460 °C and a V/III ratio of 229. The total growth time for these NWs was 15 minutes. Figure 3.4 presents a bright-field TEM image, a high resolution TEM image and the PL spectra of single InP NW grown along <001> crystal direction. The NW is pure ZB without any stacking fault and slightly tapered. This stacking-fault free NW yields a narrow PL line width of only 2.3 meV at 2.4 W/cm^2 (and 8.1 meV at 100 W/cm^2). This result implies that <001> NWs can provide high material quality for high efficiency solar cells.

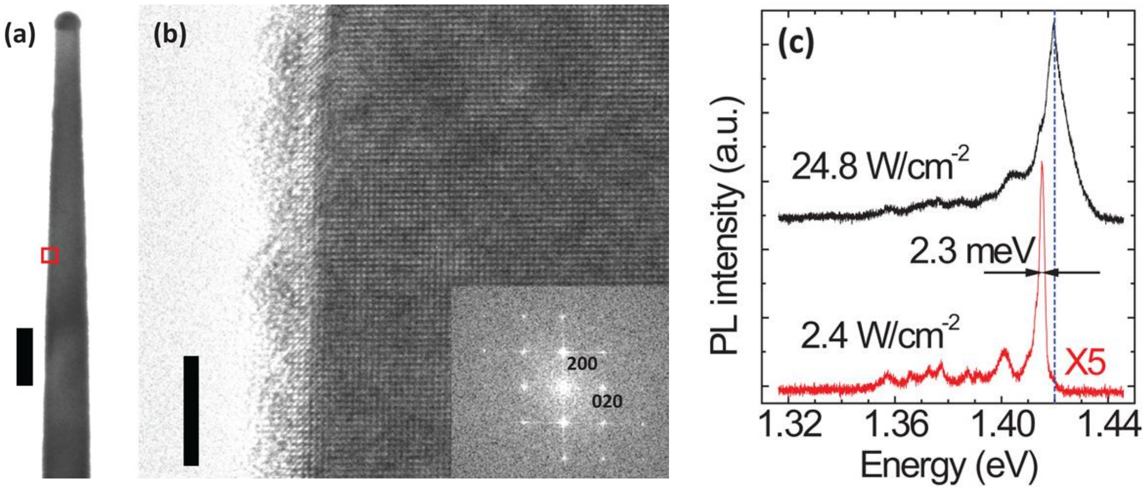

Figure 3.4. (a) Bright-field TEM image of a [100] InP NW. (b) High resolution TEM image of the boxed area. The inset shows the Fourier transform of the HRTEM image, displaying a [001] zone axis pattern. The PL measurement (c) shows a very narrow free exciton line with a width of 2.3 meV at an excitation density of 2.4W/cm^2, indicating an excellent crystal quality. The scale bar is 100nm for (a) and 5nm for (b).

However, one drawback of the <001> NWs is that the growth direction is less favourable. Growth of InP NWs on (001) substrates often exhibits a poor vertical yield. The percentage of vertical wires can be improved by using poly-L-Lysine surface treatments prior to the growth [137]. However, this treatment can contaminate the NWs with carbon impurities, which then degrade the materials quality. Recent result by Wang *et al.* has demonstrated that by filling the catalyst droplet with In to equilibrium composition prior to the NW growth initiation, a vertical yield of higher than 90% can be achieved without using poly-L-Lysine [139], which makes the <001> NWs promising for solar cell applications.

3.3.3 Reduction of incorporated impurities

3.3.3.1 High growth temperature and in-situ HCl etching

High growth temperature yields better optical quality. However, unintentional radial growth on the NW sidewall becomes significant at high temperature. This shell growth results in tapered NWs and can degrade the device performance by short-circuiting axially designed structures [140]. Sidewall growth, at a temperature lower than the normal bulk growth, often leads to incorporation of impurities, which can act as recombination centres for charge carriers. Borgström *et al.* have shown that *in situ* etching by using HCl [19, 20] can prevent tapering, even under growth conditions, which would otherwise lead to strong radial growth.

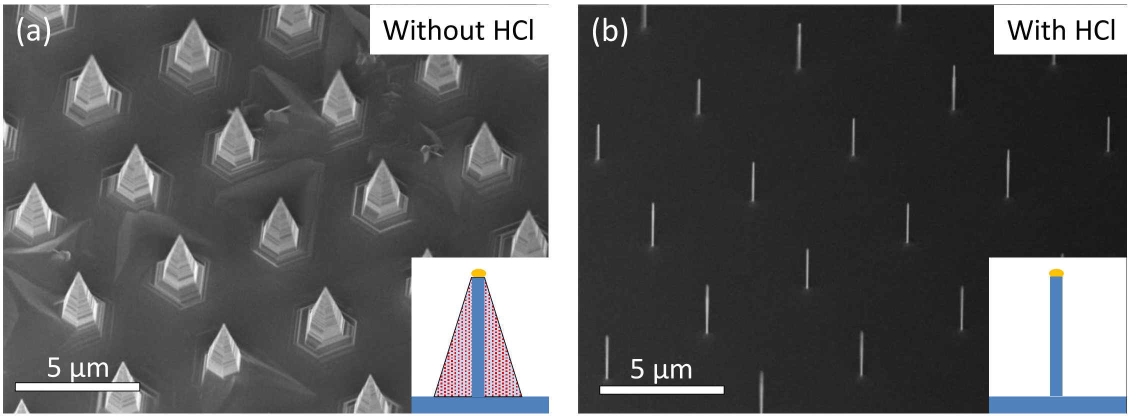

Figure 3.5. SEM images of InP NW samples grown (a) with and (b) without using HCl in situ etching. The sample grown without HCl shows NWs with a pyramidal shape due to vapor solid (VS) growth on the sidewall at a high growth temperature of 540 °C while the sample grown with optimal HCl flow shows a non-tapered smooth NW surface.

SEM images of two InP NW sample grown at the same growth condition at 540 °C with and without HCl are shown in figure 3.5. The sample grown with optimal flow of HCl show straight and non-tapered morphology while the sample grown without HCl shows pyramidal shapes. It is still under debate whether Cl atoms also passivate the surface of the NW during the growth and further reduce the incorporation of unwanted impurities.

The growth of high quality bulk InP by MOVPE is usually carried out at a growth temperature above 600 °C [141]. However, InP NWs are usually grown at a much lower temperature [142] (420 – 480 °C). Now we study the effect of a higher growth temperature on room-temperature PL intensity and PL lifetime of single <001> NWs by using identical growth parameters, except for the growth temperatures. We have chosen to study <001> NWs because they have the pure ZB crystal phase for all growth temperatures, allowing to directly compare the PL intensity and the PL lifetime measurement. We compare the room-temperature PL instead of low temperature PL because the effect of non-radiative processes due to incorporated impurities on PL efficiency is more pronounced at room temperature.

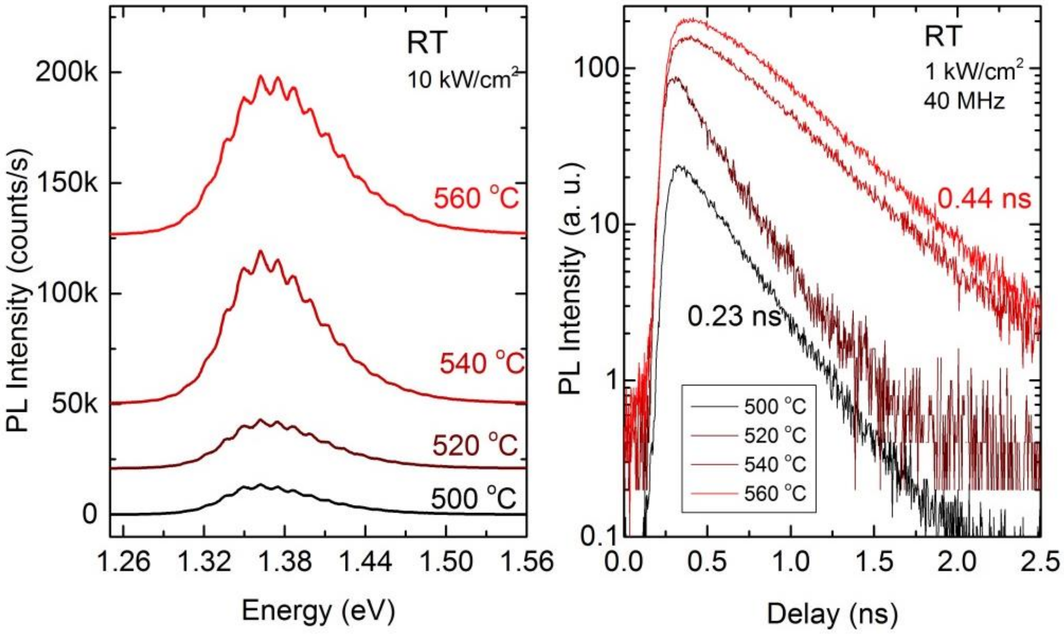

Figure 3.6. Influence of growth temperature on the room temperature photoluminescence (PL) intensity (left) and PL lifetime (right) of <100> InP NWs grown at different temperatures. The offsets are added for clarity. The PL intensity increases 5.4 times and the PL lifetime doubles when the growth temperature increases from 500 °C to 560 °C. The small peaks superimposed on top of the broad PL spectra are artefacts resulting from interference within the CCD.

Figure 3.6 shows typical room-temperature PL and time-resolved PL spectra of <001> InP NWs. It is clearly observed that the PL intensity is enhanced by 5 times and the PL lifetime is doubled when the growth temperature is raised from 500 °C to 560 °C. A low temperature PL study on these samples (not shown here) exhibit a sharper ZB bandgap and D-A peaks for sample grown at 560 °C compared to the sample grown at 500 °C.

3.3.3.2 Post growth surface cleaning and removal of impurities

The use of in-situ HCl etching can significantly reduce the sidewall growth at high temperature. However, in many cases, the complete elimination of the sidewall growth is not fully achieved. Figure 3.7(a) shows TEM images of a ZB twining supper lattice (ZB-TSL) InP NW grown by using 80 nm gold seeds at 540 °C. The precursor molar fractions for the indium and phosphorus sources was chosen to be $\chi_{TMI} = 5 \times 10^{-5}$ and $\chi_{PH3} = 2 \times 10^{-2}$ respectively, giving a V/III ratio of about 400. To avoid tapering, HCl was introduced after a 15s nucleation step using a molar fraction of $\chi_{HCl} = 5 \times 10^{-5}$. The NWs have flat sidewalls and do not show any visible tapering.

As explained by Algra *et al.* it is mandatory that during the growth of a ZB-TSL, saw-tooth facets, consisting of alternating {111}A and {111}B facets, are formed [143]. It is remarkable that our ZB-TSL NWs clearly show flat facets, as can be seen in Figure 3.7(a) and (b). This can be explained by the overgrowth of the original {111} side facets to form flat and stable {110} sidewalls [144]. Together with the fact that imaging was performed along the <110> zone axis, this proofs that we have {110} side facets, as reported earlier in reference [144].

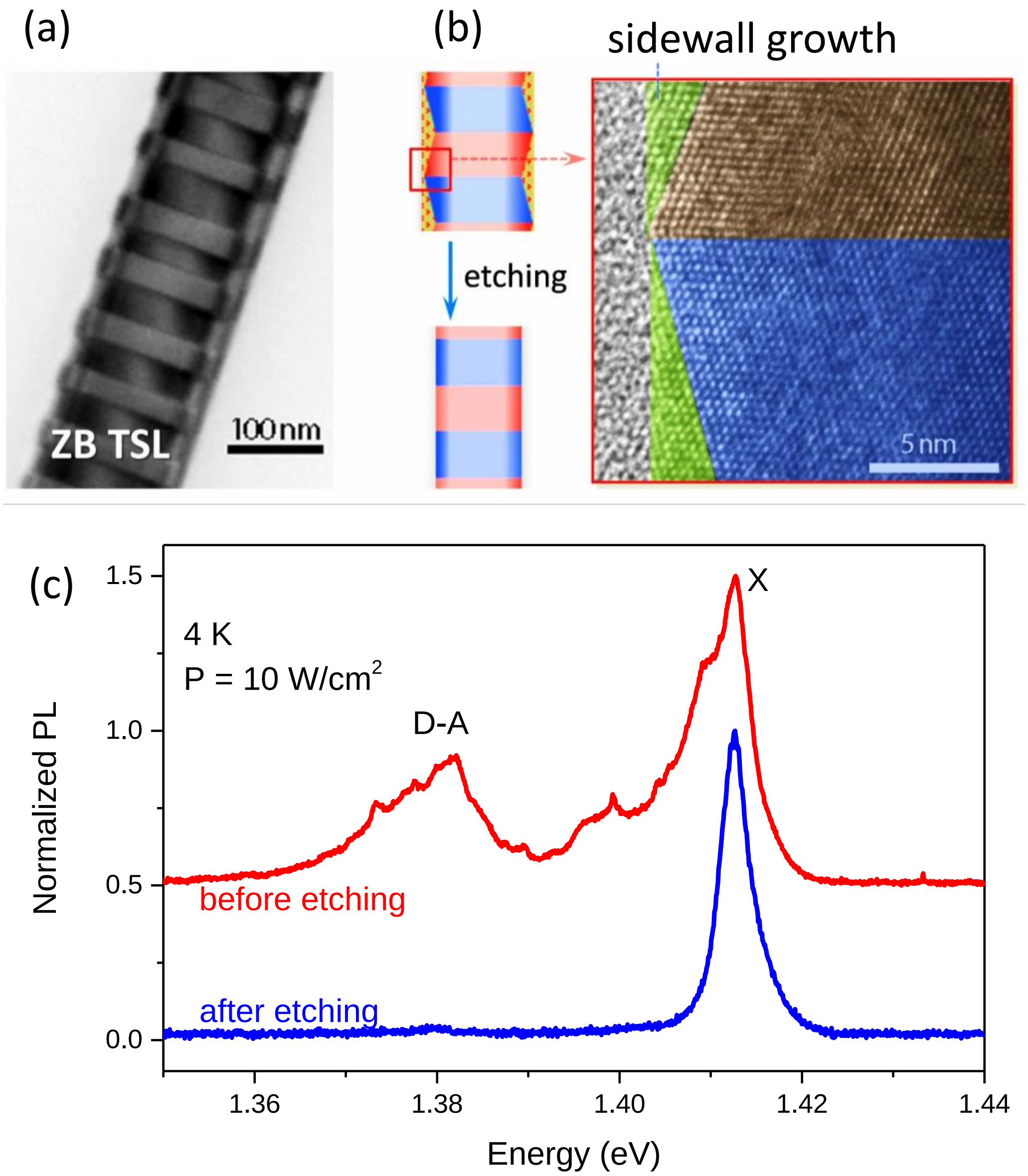

Figure 3.7. Removal of the excessive impurity incorporation as introduced during vapor-solid (VS) growth on the sidewall of zincblende (ZB) InP NWs. (a) TEM images of a ZB twinning super-lattice (ZB-TSL) InP NW showing a flat side wall instead of the sawtooth morphology (typical morphology of ZB-TSL NWs) due to VS growth. The contaminated sidewall can be completely removed by piranha etching, resulting in a clean PL spectrum as illustrated in (c).

A possible explanation for the overgrowth might be that the polar {111} facets are more difficult to passivate with Cl compared to {110} facets. This could lead to two situations: 1) layer-by-layer sidewall growth of the (unpassivated) {111} facets, leaving the outer morphology unchanged. This is contradictory to our observations, or 2) a rapid formation of {110} nano-facets on the VLS-grown {111} side-facets. Growth will now only proceed by expanding the passivated {110} nano- facets and will fully stop as soon as the flat side facets are obtained. The fact that no tapering is observed supports this latter hypothesis. The investigation of such a side facet dependent passivation goes beyond the scope of this chapter. The fraction of InP material that overgrows the corners between the original {111} side facets to create the flat {110} sidewalls are colorized green in the high-resolution TEM image in figure 3.7(b).

We have performed PL measurements on single NWs of this sample at a low excitation power of 10 W/cm^2 at 4 K to highlight the impurity emissions. The PL spectrum (red curve in Figure 3.7(c)) exhibits a main peak at 1.414 eV which is attributed to free-exciton emission. The broad emission at about 1.38 eV is attributed to donor-acceptor pair recombinations (D-A), which are likely from impurities incorporated during the vapor-solid growth on the sidewall. We prove this assumption by removing the overgrown shell of the NWs.

The shell of the ZB TSL NWs is removed by a 5 seconds etching in a Piranha solution with an etch rate of approximately 2 nm/s. This reduces the NW diameter from approximately 200 nm to approximately 180 nm. From a geometrical perspective, the shell is estimated to have a thickness between 10 and 17 nm, depending on the spacing of the twin planes in the TSL. This leads to the etching of almost the complete contaminated shell. The PL spectrum of the post-growth-etched NW is presented (blue curve) in figure 3.7(c). This spectrum was measured at exactly the same measurement conditions as the spectrum of the NW before etching. It is clearly seen that the D-A emission is almost completely removed, resulting in a high quality PL spectrum, which is now only dominated by a band gap-related peak. This means that the VS growth on the sidewall contains a large amount of impurities which can be removed by post-growth etching. We will show later that this treatment also allows the surface cleaning of NW solar cell for significantly improving the efficiency of a NW solar cell.

3.3.4 Improving the material quality for nanowire solar cells

The NW solar cells in our group are fabricated by using a two dimensional square array of axially grown p-n NW junctions on <111> InP substrates (diameter of about 100 nm and pitch of 513 nm). The NWs are grown in an Aixtron CCS MOVPE system using trimethylindium (TMI) and phosphine (PH_3) at 450°C. HCl is introduced at a 2.83×10^{-5} molar fraction to reduce radial growth. Diethylzinc (DEZn) and H_2S are used as p-type and n-type dopants. The total growth time is 19 min, resulting in a NW length of 2.3 μm with the p-n junction located at the middle part of the NWs. TEM studies (figure 3.8(a)) indicate that the n-part has dominant WZ crystal structure with ZB stacking faults and the p-part shows a ZB structure with many twin planes (about 10-15 nm spacing) due to the different effect of H_2S and DEZn during the growth [143, 145].

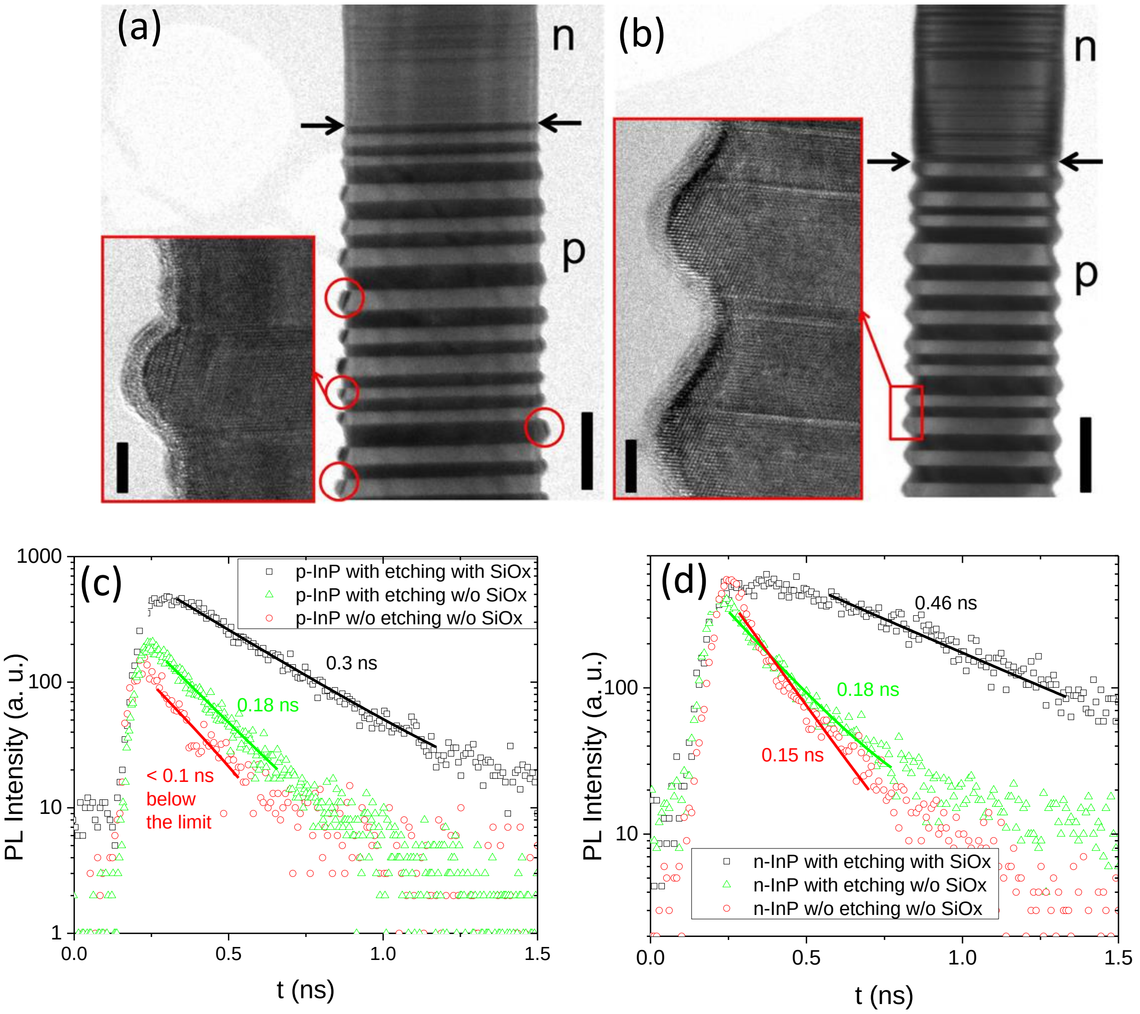

Figure 3.8. TEM images of p-n junction in InP NWs before (a) and (b) after surface cleaning. Room-temperature PL lifetimes (c) and (d) of p-InP and n-InP NWs before and after etching and after surface passivation by SiO_2, showing a strong improvement in both the PL intensity and PL lifetime.

It is noticeable in figure 3.8(a) that a very rough surface is observed on the sidewall of the p-doped NW section. We observe large extrusions or side-branches, as shown in the red circles. Each of them contains many stacking faults. The formation of the extrusions is related to the presence of HCl during InP growth and can be tuned with DEZn dopant concentration. These extrusions with poor crystal quality are a source of non-radiative recombination, which is detrimental to solar cell performance. Figure 3.8 (b) shows that piranha etching can effectively remove these extrusions, resulting in clean <111> sidewalls without visible defects.

To gain understanding on the effect of piranha etching on the optical properties, room temperature PL lifetime measurements on NWs transferred onto a thermally oxidized Si wafer were performed. For this study p-doped and n-doped InP NWs were grown separately using the same growth parameters as for the p-n junction. These NWs were also etched by piranha for 25 sec, and capped with a 40 nm thick SiO_2 shell. These processes are kept identical as for the solar cell fabrication. The lifetime of p-type NWs before piranha treatment is below the instrumental resolution of 0.1 ns. The lifetime is improved to 0.18 ns only with piranha etching. After piranha etching together with passivation by a SiO_2 shell, the PL lifetime is improved further to 0.3 ns and stabilized at this value. A similar trend is observed for n-InP NWs, the PL lifetime increases from 0.15 ns to 0.18 ns after piranha etching and 0.46 ns after piranha etching and SiO_2 passivation. This is attributed to the elimination of defects and carbon impurities in the unintentional grown NW sidewalls and also to the SiO_2 passivation [146]. The combination of piranha etching and SiO_2 capping is important to improve and keep the lifetime stable for long period of time.

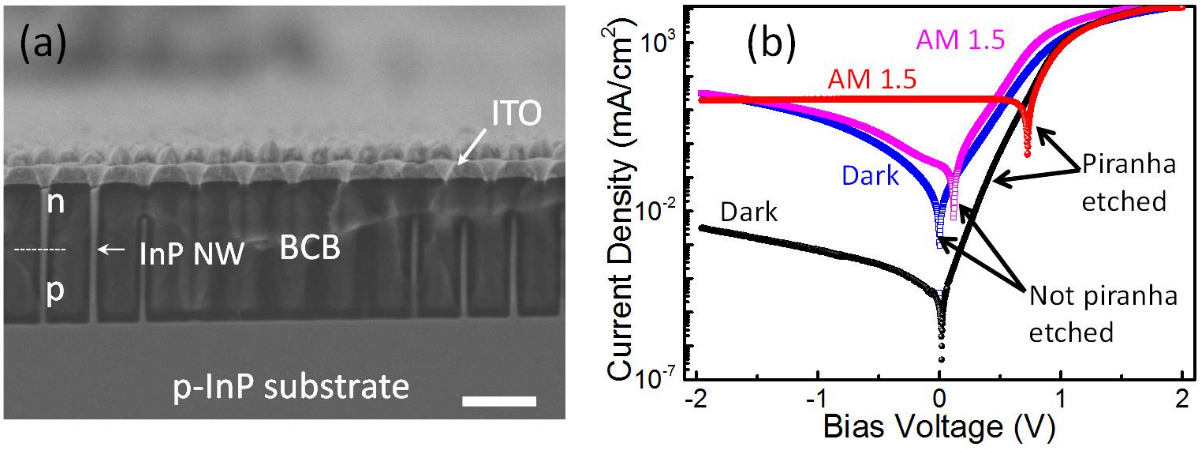

Figure 3.9. SEM image of the as-grown InP NW solar cell device. The device consists of an array of p-n nanowires on p-InP substrate. The space between nanowires is filled by benzocyclobutene (BCB) for isolation and planarization. Ti/Pt/Au is used to form a back contact to the substrate, and 300 nm indium−tin−oxide (ITO) is deposited as the front contact. (b) Log J−V characteristics of our best solar cell in the dark (black) and at 1 sun (red). For comparison, we also show the J−V curve without piranha etching in the dark (blue) and at 1 sun illumination (pink*)* [62].

The cross section of a complete nanowire solar cell device (500×500 μm^2) fabricated in our group is presented in figure 3.9(a). The nanowires are etched by piranha and immediately capped by a SiO_2 shell. The SiO_2 is used to improve the adhesion between the NWs and the benzocyclobutene (BCB) - an isolation and planarization layer. Ti/Pt/Au is used to form a back contact to the substrate, and 300 nm indium-tin-oxide (ITO) is deposited as the front contact. The detailed fabrication process is presented in reference [62].

Figure 3.9(b) show the current density – voltage (*J-V*) curves of two solar cell devices fabricated with and without piranha etching step. The NW solar cell without piranha etching step shows very poor performance. The NW solar cell with 25 s of piranha etching exhibits an open-circuit voltage of 0.73 V, a short-circuit current density of 21 mA/cm^2, and a fill factor of 0.73 at 1 sun. This yields a power conversion efficiency of up to 11.1% at 1 sun. Therefore, post growth piranha etching of our NWs is critical for obtaining a good solar cell performance.

3.4 Conclusions

We have discussed several important aspects of the VLS-grown NW by MOVPE in order to obtain high material quality for NW solar cells. The crystal phase purity of the NW can be improved by different growth parameters such as the size of catalyst and growth temperature. In order to obtain high optical quality of InP NWs, high temperature growth in combination with HCl *in situ* etching were employed. This combination helps to avoid tapering and to reduce the incorporation of unwanted impurities. The overgrowth on the sidewalls of the NW degrades the material quality of the NW and is harmful to the solar cell performance. We have shown that the excessive impurity incorporation at the nanowire sidewalls can be successfully removed by post growth cleaning using a piranha solution.

Chapter 4

High optical quality single crystal phase wurtzite and zincblende InP nanowires

In this chapter we report single crystal phase and non-tapered wurtzite (WZ) and zincblende twinning superlattice (ZB TSL) InP nanowires (NWs). The NWs are grown in a metalorganic vapor phase epitaxy (MOVPE) reactor using the vapor-liquid-solid (VLS) mechanism and in-situ etching with HCl at high growth temperature. Our stacking fault-free WZ and ZB TSL NWs allow access to the fundamental properties of both NW crystal structures, whose optical and electronic behaviours are often screened by polytypism or incorporated impurities. The WZ NWs do not show any acceptor related emission, implying that the VLS-grown NWs are almost impurity-free due to sidewall removal by HCl. They only emit light at the free-exciton (1.491 eV) and the donor-bound exciton transition (1.4855 eV). The ZB NWs exhibit a PL spectrum being unaffected by the twinning planes. Surprisingly, the acceptor related emission in the ZB NWs can be almost completely removed by etching away the impurity contaminated sidewall grown via a vapor-solid mechanism

4.1 Introduction

Semiconductor nanowires (NWs) have been extensively studied because of their fascinating optical and electronic properties. They are recognized as promising candidates for future applications, including NW quantum bits [1, 2], the realization of Majorana's fermions [3], single photon detection [4] and future generation photovoltaic cells [5-8, 62, 76]. For a device, such as a NW solar cell, many requirements should be simultaneously met, including a perfect crystal phase, a low surface recombination velocity, the absence of unintentional sidewall growth and very low residual doping levels [5-8, 62, 76]. From a more fundamental point of view, the question arises whether the vapor-liquid-solid (VLS) growth mechanism allows controlling the NW growth down to the atomic scale, yielding "perfect NWs". In this chapter, we will set a step towards this goal by demonstrating both purely wurtzite [132, 142, 145, 147] (WZ) and purely zincblende (ZB) crystal phase <111> InP NWs grown by MOVPE in which the contamination by residual impurities has been almost completely removed.

Unintentional radial vapor-solid (VS) during vapor-liquid-solid (VLS) growth gives sidewall growth that not only leads to unwanted NW-tapering, but the low nanowire growth temperature presumably also results in high impurity incorporation in the NW-shell [27, 148, 149]. Thus, as a first step towards a high optical quality NW, the growth on the sidewall of NWs should be eliminated to avoid broadened bandgap related PL and a degraded PL-efficiency at room temperature. In this chapter we build upon the approach of Borgström *et al.* [27] by using *in-situ* etching and surface passivation with HCl to prevent uncontrolled sidewall growth around the InP NW.

Growth of III-V NWs using the VLS mechanism often results in polytypism with random distribution of zincblende (ZB) and wurtzite (WZ) segments. Band structure differences between the two can lead to electron (hole) trapping in ZB (WZ) segment [111, 131, 150] and excess carrier scattering at stacking faults [133, 134]. These effects strongly degrade the NW optical and electronic properties as compared to a single crystal phase NW. As a second important step towards a high optical quality NW, *in-situ* etching with HCl enables us to increase the conventional InP VLS growth temperature of about 420°C into the range of 500 – 540°C without suffering from unintentional sidewall growth. In this chapter, we will show that the increased VLS growth temperature is a key to promote purely WZ crystal phase NWs for small NW diameter [151, 152]. We show that both ZB twinning superlattices [143] (TSL) and pure WZ InP NWs are achieved with exactly the same growth conditions for different NW diameter.

As a third important step towards a high optical quality NW, we study the residual impurities within *in-situ* etched NWs. It is important to note that the residual impurity incorporation is much more clearly visible in the PL-spectra of pure crystal phase NWs. A high VLS growth temperature is expected to also be beneficial [148, 149] for reducing the residual impurity incorporation within the NW-core. We study the impurity incorporation by performing µ-PL measurements on single NWs at very low excitation density for highlighting impurity related PL. The µ-PL measurements are performed in direct correlation with transmission electron microscopy (TEM) to be able to unambiguously attribute the different PL peaks [153]. By this approach, we are able to resolve different excitonic emission lines and almost suppress the acceptor-related emission, which is probably the result of carbon incorporation [27, 149] in MOVPE grown NWs. We finally measured temperature dependent series of the PL-efficiency and observed an improvement at room temperature due to the reduction of the impurity incorporation.

4.2 Experiment

The InP nanowires were grown on InP (111)B substrates in an Aixtron 200 MOVPE system using Au as catalyst, and trimethylindium (TMI) and phosphine (PH_3) as indium and phosphorus sources respectively. Samples with randomly distributed and e-beam lithography defined patterns of Au nanoparticles with various sizes (20 – 100 nm) were prepared and cleaned previously to the growth using first a 30s piranha etch and then an *in-situ* annealing step for 10 min at a temperature of 660 °C. After annealing the samples were cooled to the growth temperature at 540 °C and nanowire growth took place for 25min. The precursor molar fractions for the indium and phosphorus sources was chosen to be $\chi_{TMI} = 5 \times 10^{-5}$ and $\chi_{PH3} = 2 \times 10^{-2}$ respectively, giving a V/III ratio of about 400. To avoid tapering, HCl was introduced after a 15s nucleation step using a molar fraction of $\chi_{HCl} = 5 \times 10^{-5}$.

Figure 4.1 shows scanning electron microscope (SEM) images of the InP NW sample grown at 540 °C using a 25 nm Au catalyst nanoparticle array and employing *in-situ* etching with HCl. The NW-array displays uniform growth rate and the NWs show almost no tapering as compared to the pyramid shaped NWs grown without HCl (inset of figure 4.1(a)). Similar results on *in-situ* etching have been reported by Borgström *et al* [27]. Top-view and 30° tilted-view SEM images show that these NWs have a hexagonal cross-section with a diameter of about 60 nm and a length of 3 μm (figures 4.1(b-c)). TEM images of stacking fault-free WZ and ZB TSL NWs grown by 20 nm and 80 nm Au seeds are presented in figures 4.1(d) and 4.1(e), respectively.

NWs are dispersed randomly on TEM grids for the direct correlation between PL measurements and the crystalline structure of the same single NWs [153]. The overview of the measurement procedure is presented in figure 4.2. For Au colloid catalyst sizes below 20 nm, we realize WZ InP NWs without any stacking fault with our growth conditions. When the catalyst particle diameter increases up to 50 nm, ZB TSL InP NWs are grown. Until now, the formation and control of both WZ and ZB TSL by using temperature and diameter has been reported for InAs, and GaAs NWs [151, 152, 154] InP has an optical bandgap, which is near ideal for the use in single-junction photovoltaics, and InP has a much lower surface recombination velocity than GaAs [110]. So far, stacking fault free WZ and ZB TSL InP NWs were mainly realized by using high n- and p-type doping [143, 145], respectively. The present undoped WZ and ZB TSLs grown simultaneously at very high temperature of 540 °C therefore provide useful input

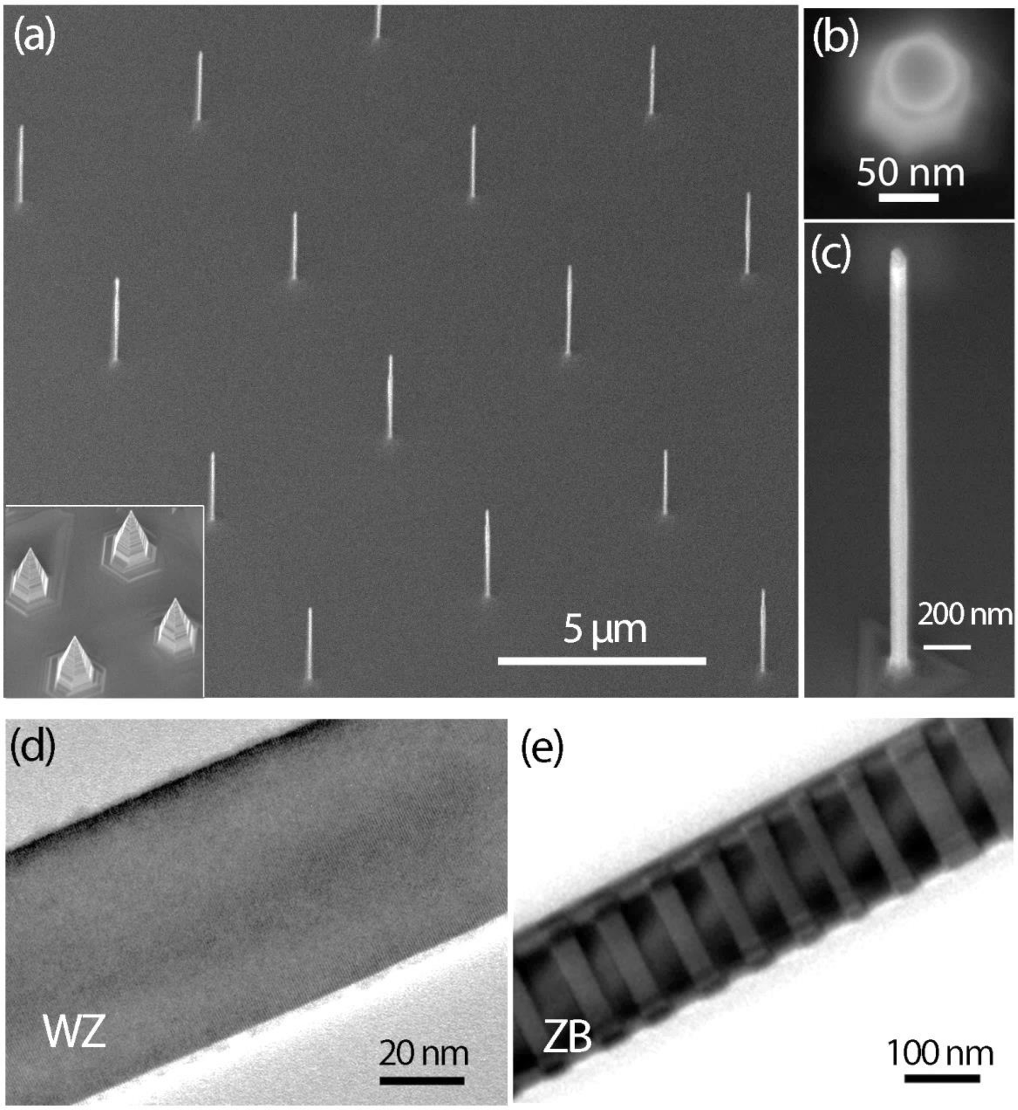

Figure 4.1. (a-c) Scanning electron microscopy images of a nanowire array grown at 540 °C using in-situ etching with HCl for suppressing sidewall growth: (a) large-area view, (b) top-view and (c) zoom-in images. Inset of (a) shows NWs grown under identical growth conditions but without using HCl. (d,e) Transimision electron microscopy (TEM) images of a stacking fault-free wurtzite InP nanowire and a InP ZB twinning superlattice grown by using 20 nm and 80 nm Au catalyst nanoparticles, respectively. These wires have been grown on the same substrate. Imaging was performed along the <2-1-10> and <011> zone axes, respectively.

to a more complete understanding of InP NW growth and crystal structure formation. Our pure WZ and ZB TSL NWs allow us to access the fundamental properties of both InP crystal structure NWs, whose optical and electronic behaviour are often screened by stacking faults, polytypism, and intentional or unintentional impurity incorporation in the NW shell. In the following we will mainly focus on the optical and structural properties of these NWs by using µ-PL, TEM and PL efficiency measurements.

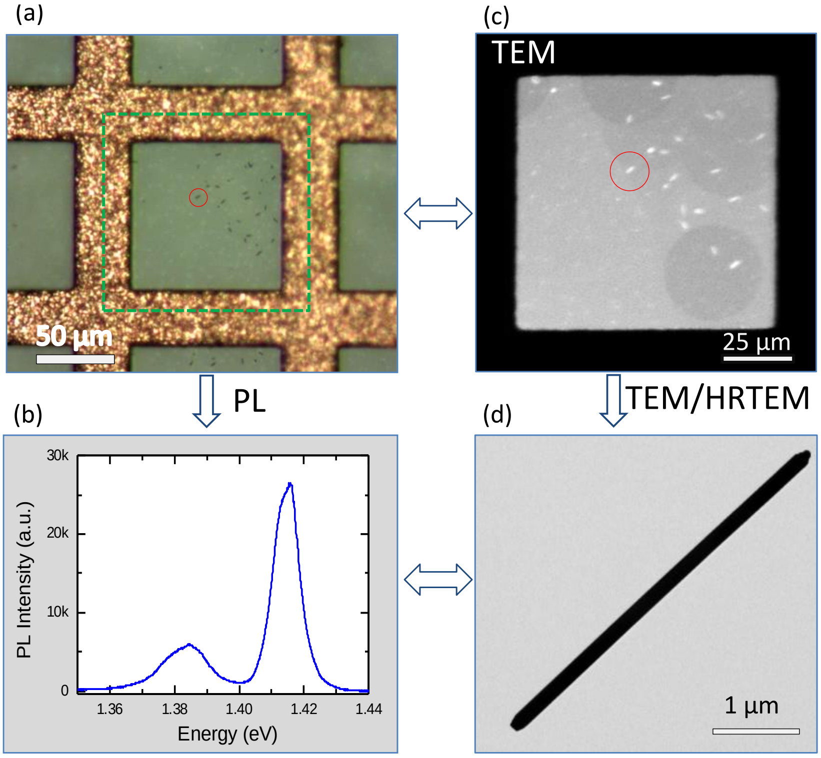

Figure 4.2. Overview of the measurement process: (a) Optical microscopy image of transferred nanowires on a TEM copper grid. (b) Low temperature PL measurement on a single nanowire prior to TEM examination to avoid the possible material destruction due to electron beam. (c-d) TEM and/or high-resolution TEM (HRTEM) images of a single nanowire, which has first been studied by PL (marked as red circles). Based on the PL and TEM results on the same nanowire, a direct correlation between optical and structural properties can be performed.

4.3 High optical quality single crystal phase wurtzite and zincblende InP nanowires

4.3.1. Stacking fault free wurtzite InP nanowires

Correlated µ-PL and TEM images of the same NW are presented in figure 4.3. TEM studies show that the studied InP NW grown from a 20nm Au particle has a diameter of about 70 nm and a length of 1.7 µm. A careful high-resolution TEM examination along the whole length of the NW indicates that it is free of any stacking faults or ZB insertions. The power dependent µ-PL at 4 K of this NW reveals interesting spectra when

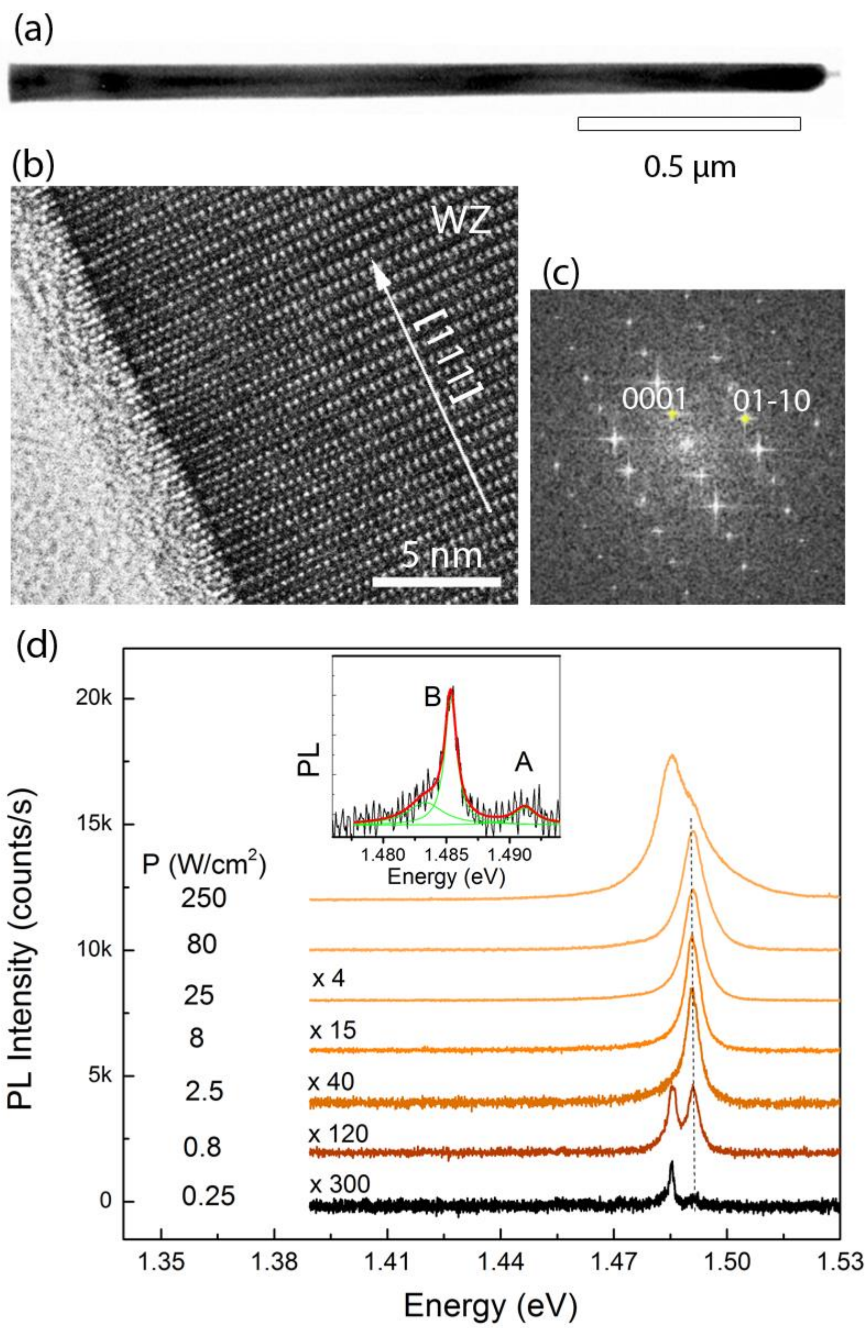

Figure 4.3. Direct correlation of the structural and the optical properties of a pure wurtzite InP nanowire. (a), (b) and (c) TEM, HRTEM images along the <2-1-10> zone axis, and associated FFT image. (d) Micro-PL spectra of the same nanowire measured at excitation densities in the range 0.25 – 250 W/cm^2 at 4 K. The inset shows the expanded bandgap-related PL at 0.25 W/cm^2. At low excitation power (0.25 W/cm^2) a sharp peak at 1.4855 eV (labelled as B in the inset) with a FWHM 1.5 meV. This is probably the bound exciton (D^0,X) and/or the neutral donor recombination with a free hole (D^0,h). The dashed line shows free exciton emission centered at 1.491 eV (labelled A in the inset, FWHM of 2 meV), which becomes dominant at excitation higher than 2.5 W/cm^2.

we reduce the excitation density down to 0.25 W/cm^2, which is two orders of magnitude lower than the excitation density where the crystal phase quantum dots are studied [131] (~ 20 – 1000 W/cm^2) and ten times lower than the PL studies of the stacking fault free WZ InP NW grown by using sulphur, reported in reference [145], and those grown on SrTiO$_3$ (001) substrate [155]. The low excitation power PL measurement allows us to observe the near-gap PL which is well-known for high quality bulk-type semiconductors [156]. At the lowest excitation powers (0.25 – 0.8 W/cm^2), a peak is observed at 1.4855 eV, labelled (B) in the inset, with a full width at half maximum (FWHM) of 1.5 meV. This is most probably the bound exciton (D^0,X) and/or the neutral donor recombination with a free hole (D^0,h) [145]. It is however important to note that no additional peaks, e.g. no donor-acceptor (D^0-A^0) or electron-acceptor (e-A^0) related recombination, are observed. This indicates that we realized almost no impurity incorporation due to the combination of HCl *in-situ* etching and the high temperature growth resulting in a high quality WZ NWs. The spectral line centered at 1.491 eV (dashed line in figure 4.2(d)) with full width at half maximum of about 2 meV corresponds to a free exciton recombination (peak (A) in the inset of figure 4.2). This free exciton recombination peak becomes pronounced at slightly higher excitation powers and dominates the PL-spectra at powers higher than 2.5 W/cm^2. The free exciton PL peak gradually broadens and turns into free electron-hole recombination when the excitation density further increases and band filling appears [157, 158]. The observed PL-spectra are essentially different from the PL-spectra observed in WZ NWs with ZB stacking faults, where the electrons and holes are trapped and then recombine radiatively at a lower energy, resulting in a broad emission in the region between ZB and WZ bandgap energies (1.42 – 1.49 eV) [131, 132, 158].

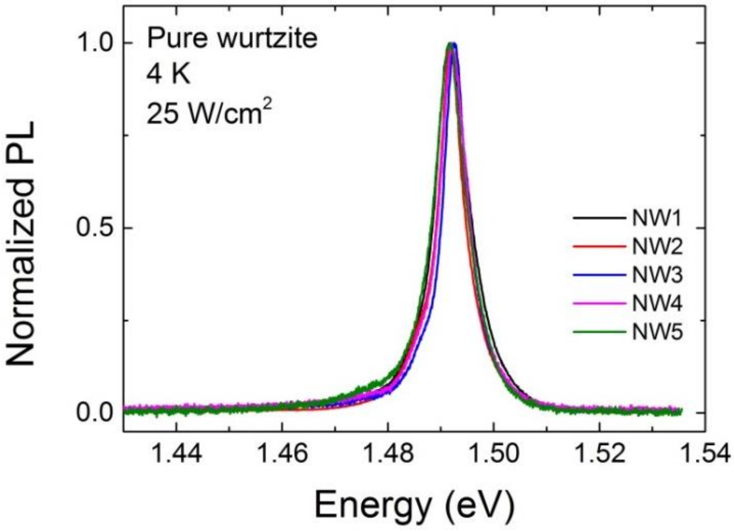

Figure 4.4. The PL spectra from different wurtzite nanowires are almost identical. No acceptor-related transitions (1.45 eV) are observed, indicating excellent material quality.

Importantly, other NWs of this sample yield similar results. The PL peak positions and PL line widths of five different NWs are very consistent, as seen in figure 4.4. We are therefore able to unambiguously determine the bandgap energy of the WZ InP to be at about E_g = 1.494 ± 0.0004 eV (including the exciton binding energy of 3 meV obtained from the Arrhenius-equation fit shown in figure 4.10(d)), which is close to the value reported [130, 142, 145]. These high quality WZ NWs have potential for NW devices which require single WZ crystal phase and low impurity contamination. At an excitation density exceeding 80 W/cm^2, we observe heating effects resulting from the low heat conductivity of the carbon film. The PL red shifts, broadens and finally decreases in intensity [153].

4.3.2 Zincblende twinning superlatice InP nanowires

The direct correlation between the structural and the optical properties of a ZB NW is presented in figure 4.5. The TEM image shows a NW of about 200 nm in diameter and 3.5 μm in length containing many twins. A twin plane is defined as a mirror plane between two segments which are mutually rotated by 60^o (figure 4.3b) [143]. Different from the growth with 20 nm Au catalyst nanoparticles, the 80 nm Au nanoparticles result in a ZB twinning superlattice (TSL), with a segment length between two twin boundaries of roughly 30 nm at top part of the NW. The twin plane density however increases near the bottom of the NW. Again, no tapering effect is observed for this NW showing that the *in-situ* etching with HCl is effective. The μ-PL study on this NW presented in figure 4.5(d) shows two major peaks at 1.414 eV and 1.38 eV at low excitation powers. The first peak (FWHM = 6 meV, at 0.25 W/cm^2) is bandgap related and is at about 4 meV below the free exciton line observed in bulk [159]. The second peak at 35 meV below the first peak is attributed to either an acceptor-related transition [160] and/or the type II transition [131, 156, 161] at the interface between WZ and ZB segments. The type II emission from twin planes (monolayers of WZ) would be very close to the bandgap-related transition from ZB InP (~1 meV below, as predicted by Zhang et al [162]) and is not clearly observed in our data. Since we do not observe any WZ segment (consisting of 2 or more sequential twin planes) in this NW from HRTEM images, this peak can be unambiguously attributed to the D^0-A^0 and e-A^0 transitions. This observation implies that we have incorporated impurities in the ZB wires, but not in the WZ wires, while they were simultaneously grown in the same run. The PL spectra from 5 different ZB wires at excitation density of 25 W/cm^2 are presented in figure 4.6. The variation in the position of PL peak is probably due to the incorporated impurity.

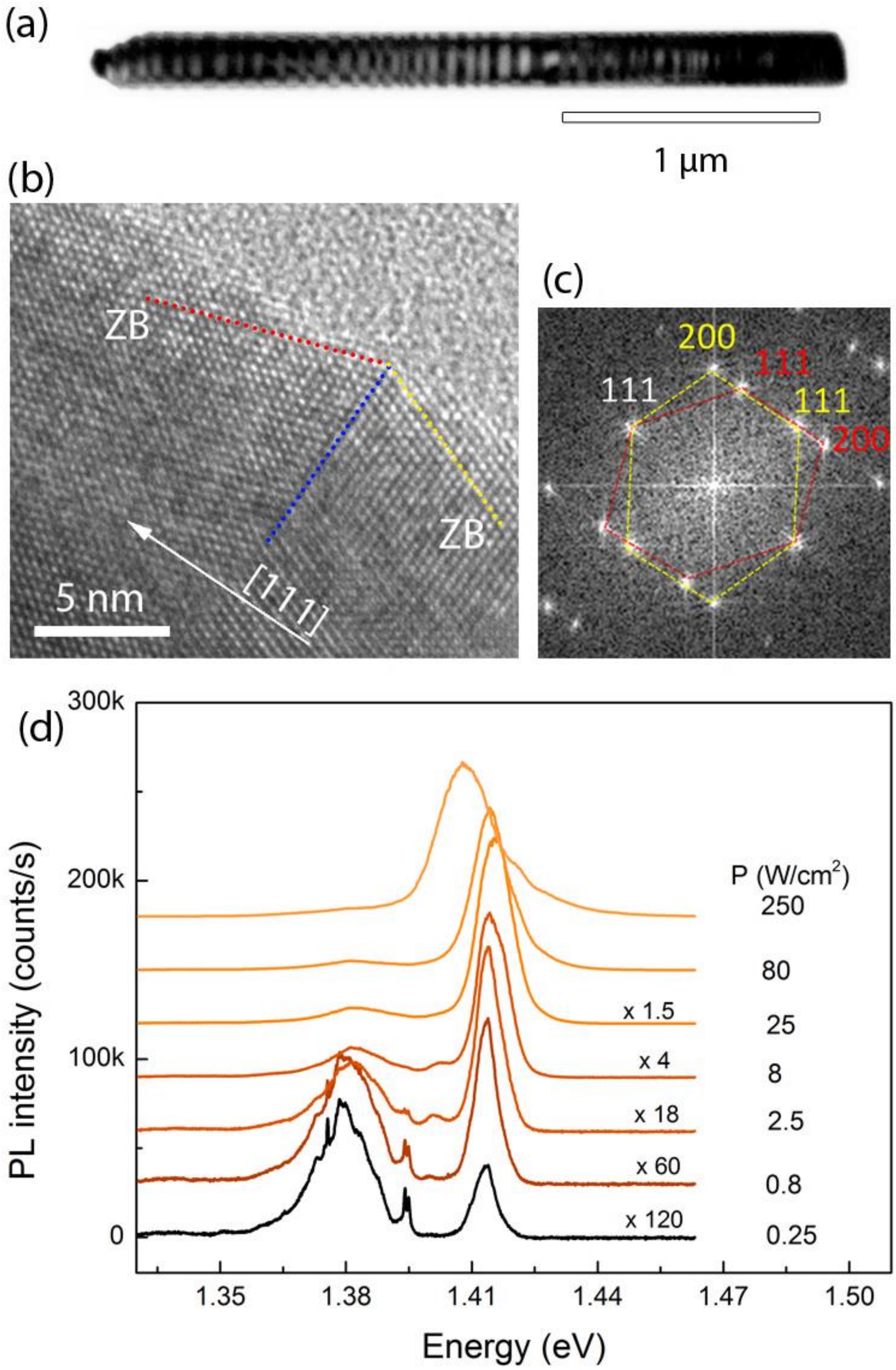

Figure 4.5. Direct correlation of the structural and the optical properties of a zincblende twinning superlattice InP nanowire. (a), (b) and (c) TEM, HRTEM images along the <011> zone axis of a small area, and associated FFT image. (d) Corresponding micro-PL spectra of the same nanowire measured at various excitation densities in the range of 0.25 – 250 W/cm^2 at 4 K.

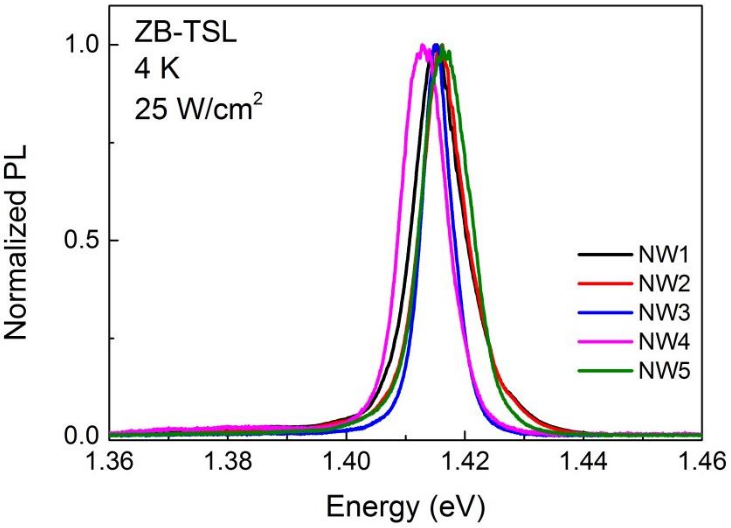

Figure 4.6. (a) PL spectra of different zincblende nanowires measured at 4K and at an excitation density of 25 W/cm^2. The variation in the PL peak is probably due to Coulomb interactions with ionized impurities.

We notice two important differences between the PL of WZ and ZB NWs:

(1) WZ NWs have narrow and consistent PL emission while the band-gap peak of ZB TSL NWs is more broadened and varies slightly from NW to NW as clearly seen in figure 4.6.
(2) ZB NWs show pronounced acceptor related impurity peaks, which do not appear in the PL spectra of WZ NWs grown in the same run.

These differences can be explained if we carefully examine the sidewall of the ZB NW in the TEM-image. It is remarkable that the ZB NW has flat side facets instead of the saw-tooth facet morphology consisting of alternating {111}A and {111}B facets, which is essential for the creation of ZB TSL NWs [143]. The flat facets are explained by the overgrowth of the {111} side facets to form flat and stable {110} sidewalls, similar to that of InAs NW presented elsewhere [144]. Radial growth, at these high temperatures, is expected to be fast because of the re-entrant corners, which are at the concave positions where the {111}A and {111}B facets meet. When these corners have grown out, the growth rate decreases and is balanced by the *in-situ* etching by HCl vapour [27].

We found that the NW sidewalls have dramatic consequences for the NW optical properties, which is shown by etching of the NWs with piranha to remove the thin sidewall layer (see also chapter 3). The power dependence PL spectra of a ZB NW after piranha etching are presented in figure 4.7. We directly observe that the donor-acceptor (D^0-A^0) or electron-acceptor (e-A^0) peaks at 1.38 eV have been eliminated and the PL linewidth decreases from 7 meV to 2.5 meV at 0.25 W/cm^2 when etched. The PL intensity of the etched NW presented in figure 4.7 is a few times smaller than that of the unetched (figure 4.5) due to the smaller volume and the variation in the PL intensity between different NWs of the same sample. Similar to the WZ NWs, the etched ZB TSL NW shows free exciton feature at 1.418 eV which becomes pronounced at high excitation power (dashed line in figure 4.7), and an impurity bound exciton line at 1.414 eV, respectively [156]. These experiments show that the core of the ZB TSL InP NW has a bulk-like PL spectrum which is not affected by the twinning planes.

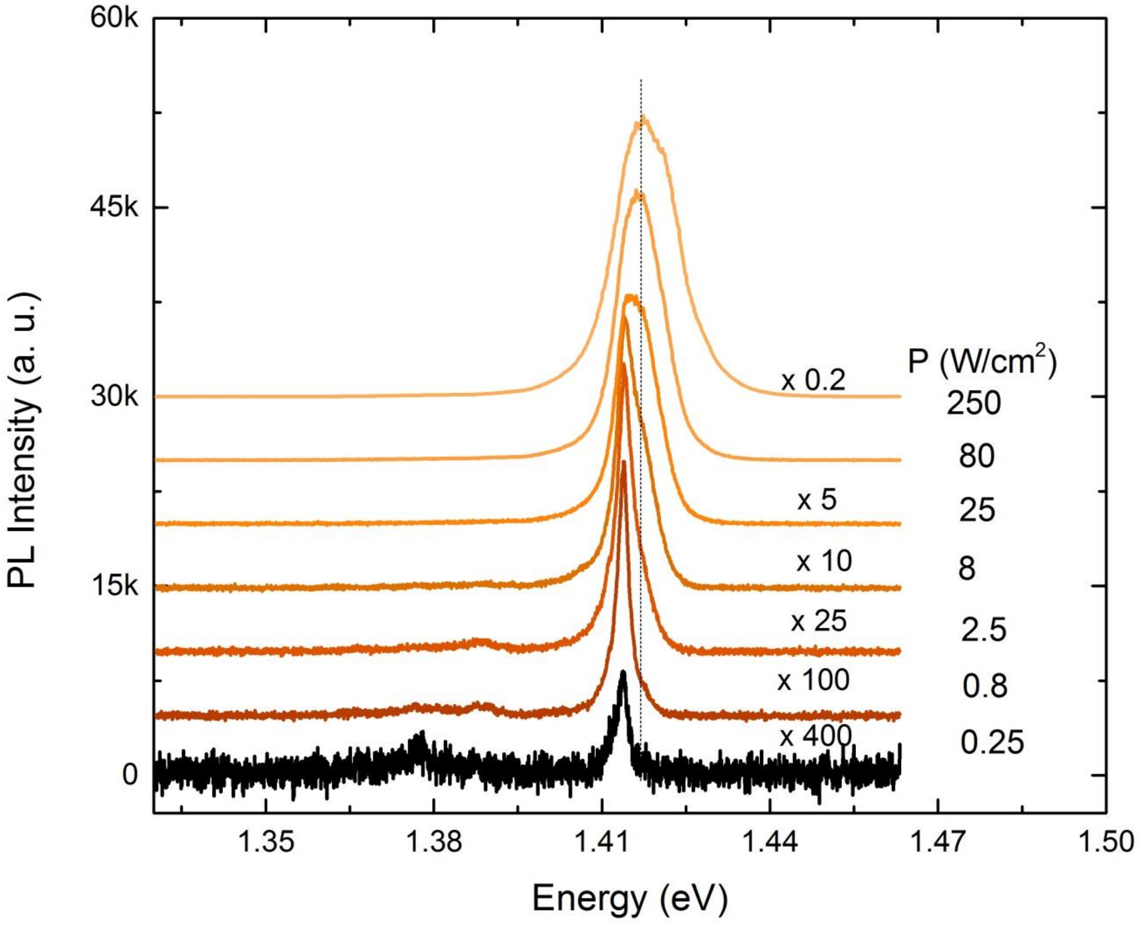

Figure 4.7. Micro-PL spectra of an etched zincblende InP nanowire measured at various excitation densities in the range of 0.25 – 250 W/cm^2 at 4 K. The acceptor-related emission observed for the unetched wires (~ 1.38 eV) is now completely removed. This indicates that most impurities are incorporated on the sidewall of the nanowires.

The very high optical quality of both the WZ and the sidewall-etched ZB NW clearly indicates that the core NW, axially grown by the VLS mechanism, has excellent structural quality and that almost no impurities are incorporated. The VS sidewall growth, in contrast, is highly contaminated by impurities even at a relatively high growth temperature of 540 ^{o}C. For many applications such as solar cells where the unwanted impurity level should be minimized, it is thus required to completely remove the unintentional sidewall growth.

4.3.3. Carrier lifetimes and temperature dependent PL-efficiency

Carrier lifetime and temperature dependent PL-efficiency measurements were performed on both WZ and sidewall-removed ZB TSL NWs (we will refer to these NWs as ZB NWs from now on) from 4 K up to room temperature. The spectrometer was tuned to the free exciton transition of either ZB or WZ InP using a spectral resolution of 0.5 nm. In order to have better thermal dissipation for a wider range of excitation powers, the NWs are transferred to thermally oxidized Si wafers instead of a Cu-grid. Figures 4.8(a-d) show the typical power dependence of the time-integrated PL and time-resolved PL spectra from WZ (left column) and ZB NWs (right column) measured at 4 K. The bright emissions from both types of NW allow us to use a broad range of excitation power 1P – 3200P (with P = 67 nJ/pulse/cm^2) in our measurements. The lifetimes as a function of excitation density are plotted in figures 4.8(e) and 4.8(f) and are obtained by fitting the time-resolved PL spectra in figures 4.8(a) and 4.8(b), respectively.

We first discuss the power dependence of the time resolved PL (TRPL) spectra from the WZ InP NW. At an excitation power below 3.2P (0.2 μJ/pulse/cm^2), the TRPL spectrum of the WZ InP NW exhibits single exponential behaviour with a decay time of τ_{W0} = 1 ns. The decay time at this low injection level does not vary considerably (less than 5 %) with excitation power below 10P. The corresponding time-integrated PL spectrum shows sharp free exciton emission. Similar to the PL spectra presented in figure 4.3, no impurity emission is observed for the WZ NW. When the excitation power is increased to the range of 10P – 1000P, the band filling gradually becomes pronounced and the TRPL spectrum cannot be fitted by standard single or multi-exponential decay. By fitting two different parts of the TRPL spectra, we found two different decay times of τ_{W1} and τ_{W0} as indicated in figure 4.8(c). The longer carrier lifetime, τ_{W1}, features the beginning of the decay when the excess carrier concentration is high. This longer lifetime process is followed by shorter lifetime τ_{W0} at the end of the decay when the excess carrier concentration is again much lower. Both τ_{W0} and τ_{W1} progressively increase when the laser power increases. They reach maximum values of τ_{W1} = 4.6 ns and τ_{W0} = 1.8 ns at an excitation power of about 2 μJ/pulse/cm^2 (32P). It is should be mentioned here that when we have more electrons and holes available for the recombination, the PL decay is expected to be faster. The fact that we observe an increase in PL lifetime with increasing excitation density is therefore counter-intuitive. This phenomena can however be understood if we consider the competition between non-radiative recombination, radiative recombination of free excitons and refilling effects at high excitation density [163].

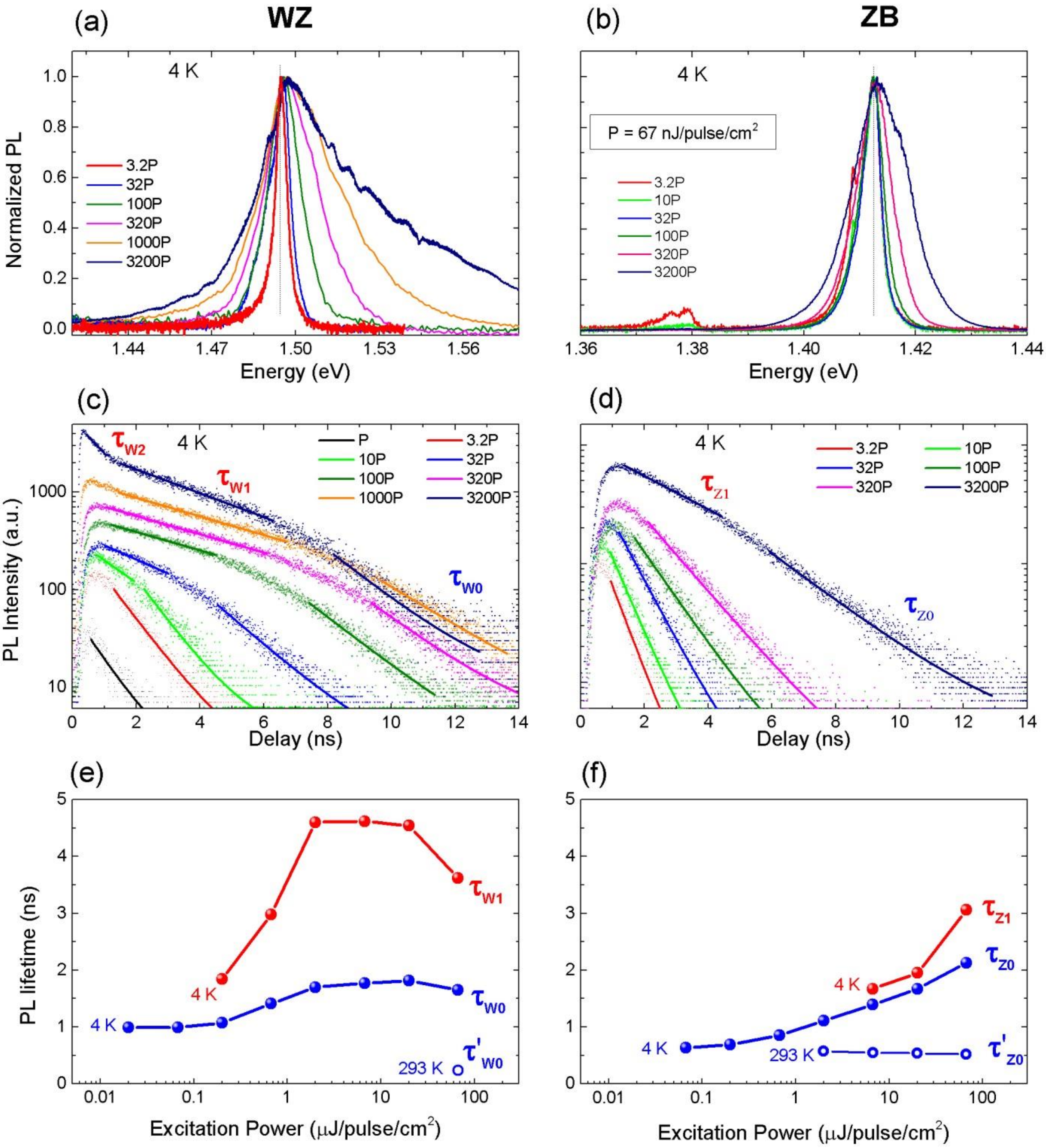

Figure 4.8. Typical power-dependent (a-b) photoluminescence (PL) and (c-d) time-resolved PL spectra of wurtzite (left column) and zincblende (right column) InP measured at 4 K. The decay times (e) τ_{W0}, τ_{W1}, τ_{W2} and (f) τ_{Z0} , τ_{Z1} are obtained by fitting the time-resolved PL spectra in c and d, respectively. τ'_{W0} and τ'_{Z0} are the decay times measured at 293 K for wurtzite and zincblende nanowires, respectively.

The enhancement of the PL lifetime with excitation power indicates that at very low excitation power the excessive carriers are mainly captured by non-radiative centres, namely mid gap defects in the bulk, or most probably, on the surface of the uncapped nanowires. The dependence of the nonradiative lifetime on the excess carrier concentration is given by the well-known Shockley–Read–Hall (SRH) formula, as described by Rosenwaks *et al.* for the case of bulk InP [163] (also see chapter 2). According to the SRH formula, when the injection level is increased, the nonradiative lifetime increases due to the saturation of traps. For our WZ NW, the competition between radiative and non-radiative processes happens under a moderate excitation of 3.2P – 32P (0.2 –2 μJ/pulse/cm^2). At an excitation level above 32P (2 μJ/pulse/cm^2), the nonradiative recombination traps are completely saturated and the recombination processes in WZ InP is dominated by radiative recombination. Once the radiative lifetime τ_{W0} becomes dominant, the effect of carrier refilling into the excitation level due to the relaxation of free carriers, starts to become important. At this point, band filling becomes clearly visible in the PL spectra, thus providing evidence for the onset of the carrier refilling mechanism towards the exciton level. Remember that the spectrometer was tuned to the exciton level, implying that we only observe free exciton recombination. The refilling mechanism accounts for the longer lifetime τ_{W1} at the beginning of the decay [164] for an excitation level above 3.2P (0.2 μJ/pulse/cm^2). The radiative lifetime of the WZ InP nanowire is therefore estimated to be $\tau_r \geq 1.8$ ns and the nonradiative lifetime is $\tau_{nr} \geq 1$ ns (at 4 K) depending on the excitation levels. At very high excitation level of 3200P (200 μJ/pulse/cm^2), the TRPL spectra show an additional decay $\tau_{W2} = 1.25$ ns. The decay time τ_{W0} and τ_{W1} also become shorter as seen in figure 4.8(e). This is probably due to Auger recombination [93], as well as the heating effect in the NW. It should be emphasized here that the radiative lifetime of our almost acceptor-free InP is 5 times higher than that of the microsized InP nanoneedles grown on Si whose the PL spectrum shows a considerable amount of acceptor-related transitions [132].

The PL and TRPL results from ZB NW (left column of figure 4.8) show similar trend as for the WZ NW. PL lifetime τ_{Z0} increases from 0.65 ns at an excitation level of 1P (0.067 μJ/pulse/cm^2) to 2.3 ns at an injection level of 3200P (200 μJ/pulse/cm^2). The saturation of the lifetimes is not observed up to our highest excitation power of 3200P. This implies that the density of non-radiative recombination in ZB NW is higher than that of the WZ NW. It is due to the fact that this ZB NW still contains some non-radiative centers from uncompleted sidewall removal (evidenced by a small PL peak near 1.38 eV in figure 4.8(d)) and some additional surface roughness after piranha sidewall etching process. At the highest excitation density, band filling effect clearly appears and a longer lifetime of $\tau_{Z1} = 3.1$ ns is observed. The lifetime τ_{Z0} measured at this excitation power ($\tau_{Z0} = 2.3$ ns) therefore approaches the true radiative lifetime of a ZB InP NW at 4 K. The radiative lifetimes from our WZ and ZB InP NWs are higher than that in reference [157] and for GaAs/AlGaAs core/shell NWs [165].

The internal quantum efficiency (IQE) of the PL emission from NWs can be extracted by measuring the integrated PL intensity I_{PL} as a function of excitation power density P_{laser}. By fitting the following equation $P_{laser} = P_1\sqrt{I_{PL}} + P_2 I_{PL} + P_3 I_{PL}^{3/2}$ (4.1), the radiative quantum efficiency as a function of excitation power density can be calculated as $\eta = I_{PL}P_2/P_{laser}$ [96]. P_1, P_2, and P_3 are three fitting parameters. The power dependent PL measurements were performed on single WZ and ZB NWs (5 NWs each sample) transferred onto thermally oxidized Si wafers using a 635 nm CW diode laser. Figure 4.9 plots the IQEs of a WZ and a ZB InP NWs for different excitation power densities at 4 K.It can be seen that at an excitation density below 3 W/cm^2, which is relevant for solar cell applications, the quantum efficiencies are relatively low. This is due to non-radiative recombination processes, which are relatively strong at low injection levels, as discussed above. The IQE values increase and become stabilized at about 80-90 % for both types of NWs at an excitation density exceeding 100 W/cm^2 where the radiative recombination is dominant.

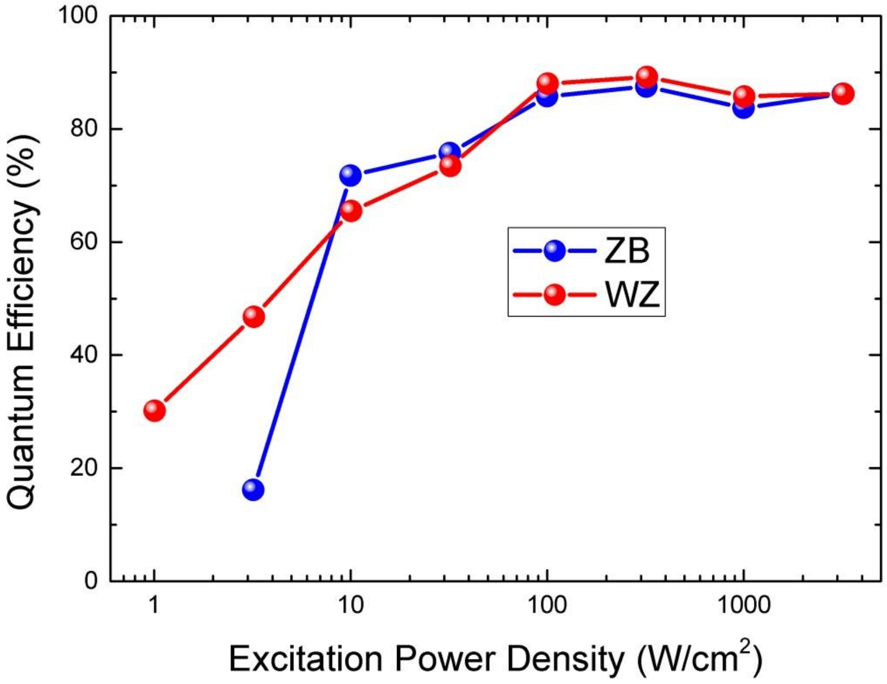

Figure 4.9. Internal quantum efficiencies (IQEs) at 4K for wurtzite and zincblende InP nanowires as a function of the excitation power density.

At higher temperature, the radiative lifetime decreases with T$^{-3/2}$, whereas nonradiative recombination increases with temperature. Rosenwaks *et al.* has shown that the electron capture into neutral acceptors (e-A$^{(0)}$) is the dominant nonradiative recombination mechanism in p-doped bulk InP [160]. We expect that the strong suppression of the impurity incorporation into our NWs by using *in-situ* etching and high temperature growth will also strongly reduce the nonradiative (e-$A^{(0)}$) recombination. We indeed observe that the PL-efficiency only decreases by a factor of 17 and 35 for WZ and ZB TSL NWs, respectively, when we increase the temperature from 10 K to room temperature as seen in figure 4.10(d). The corresponding PL lifetime of WZ NWs decreases from 1.8 ns (4 K) to 0.24 ns (293 K) while a PL lifetime of 0.54 ns at 293 K is found for ZB NWs. We emphasize that the resulting PL-efficiency at room temperature is realized in InP NWs without surface passivation and without a shell to protect the free NW surface. The recent study on micro-sized InP nanoneedles [132] demonstrates that the quantum efficiency drops only 4 times when temperature is increased from 4 K to 298 K. This remarkably high room-temperature quantum efficiency is 4.25 and 8.75 times better than that of our ZB and WZ NWs. However, the diameters of those microsized wires are of 5 and 14.2 times larger than the diameters of our ZB and WZ InP nanowires, respectively. Therefore, we believe that the quantum efficiencies of our NWs at room temperature are limited by the surface recombination, which becomes dominant at room temperature. The measured PL lifetime τ_{eff} is related to the bulk and surface recombination by the following equation: $1/\tau_{eff} = 1/\tau_{bulk} + 4S/d$. If the surface recombination is a dominant process, the PL resulted lifetime can be approximated as $\tau_{eff} \approx d/4S$. The surface recombination velocities for WZ NW ($d = 70$ nm) and ZB NW ($d = 200$ nm) are then estimated to be 7 x 10^3 cm/s and 9 x 10^3 cm/s, respectively. Those values are typical for bulk InP, and are close to the surface recombination velocities measured by us in a different study (see chapter 6).

The temperature dependent PL efficiency of both WZ and ZB InP NWs is finally presented in figures 4.10(a-b). PL spectra of WZ and ZB InP NWs measured at various temperatures ranging from 10 to 300 K. The energy of WZ and ZB emission peaks as a function of the temperature are presented as red and blue dotted curves in figure 4.10(c), respectively. By fitting those data with the Varshni equation we obtain $E_g^{WZ} = 1.497 - 4.61 \times 10^{-4} T^2/(T + 255)$ for WZ and $E_g^{ZB} = 1.416 - 4.9 \times 10^{-4} T^2/(T + 324)$. This result suggests that the bandgap of WZ InP is 1.497 eV at 0 K. The bandgap value obtained from this measurement is slightly different from that of InP NWs on Cu grid due to substrate-induced strain generated from the difference in thermal expansion coefficient of InP NWs and the host substrate as presented elsewhere [166].

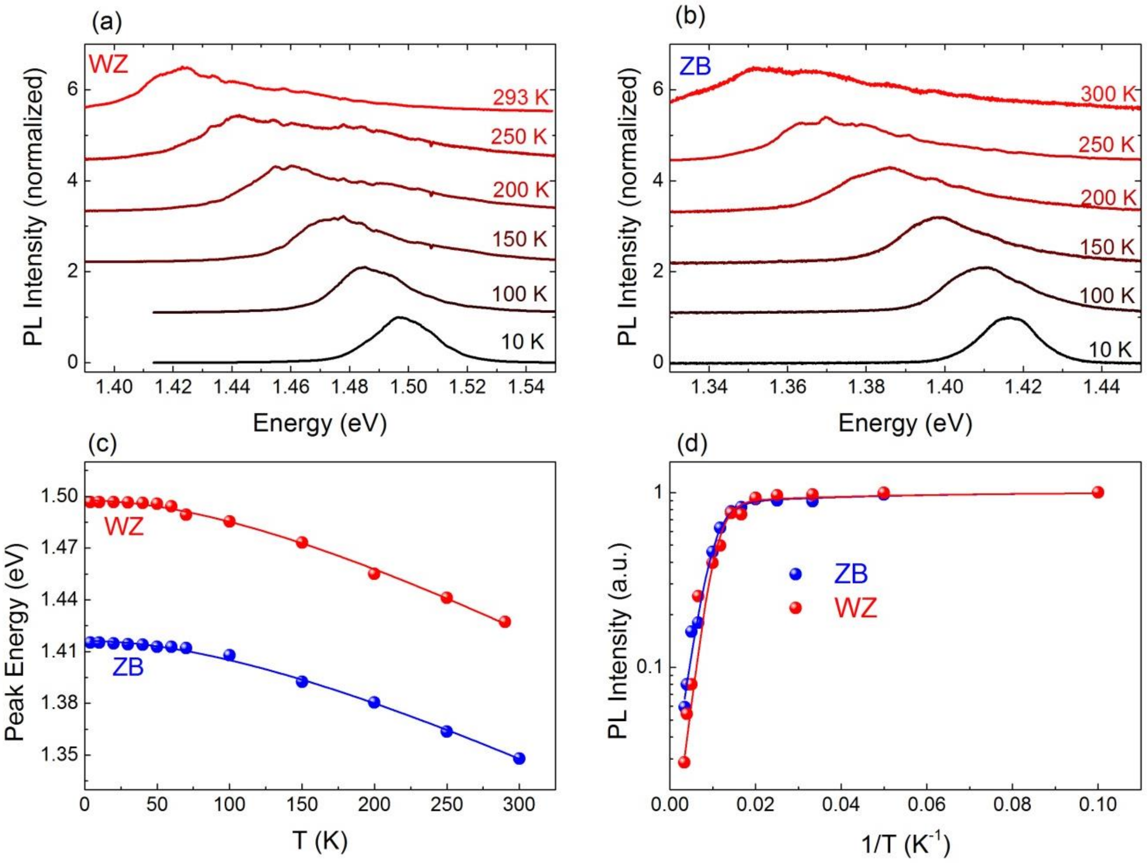

Figure 4.10. Temperature-dependent PL spectra of (a) wurtzite and (b) zincblende InP nanowires (10 to 300 K). The nanowires are pumped by a 635 nm CW diode laser at an excitation power of 104 W/cm^2. The energies of emission peaks of wurtzite (red) and zincblend (blue) nanowires are plotted in c, and fitted with the Varshni equation. (d) Temperature-dependent integrated PL intensity the two crystal phases normalized to the intensities measured at 10 K. The data are fitted with the Arrhenius equation (solid curves). The PL intensities decrease 17 and 35 times when temperature increase from 10 to 293 K.

4.4 Conclusions

We have studied the optical and structural properties of pure wurtzite and zincblende twinning superlattice InP NWs grown at a very high temperature of 540°C. The pure wurtzite InP NWs are free of stacking faults and exhibit very narrow bandgap related transitions with a free-exciton line at 1.491 eV and an impurity bound exciton line at a 5.5 meV lower energy. The zincblende twinning superlatice InP NWs contain a considerable amount of impurities in the vapor-solid grown sidewall. This contaminated sidewall can be almost completely eliminated by simple chemical etching, resulting in high quality core which was axially grown by vapor-liquid-solid mechanism. Both types of NWs exhibit long carrier lifetime and high PL efficiency up to room temperature, thus showing great potential for NW devices.

Chapter 5

Crystal phase quantum structures in GaP nanowires

One distinctive advantage of nanowires is that they enable the growth of both zincblende (ZB) and wurtzite (WZ) crystal structures. Due to the bandgap difference, a WZ/ZB/WZ nanowire section provides crystal phase quantum dots/disks (CPQDs) in a chemically homogeneous nanowire. The atomically flat interfaces result in extremely high quality quantum disks, which can be exploited as building blocks for solid state quantum systems. However, a precise control of crystal structure down to an atomic layer is notoriously challenging. In this chapter we demonstrate for the first time the controlled growth of atomically sharp WZ and ZB GaP nanowire sections, resulting in the formation of CPQDs along the nanowire length. We will discuss the band alignment between ZB and WZ GaP with special emphasis on the internal electric fields due to the spontaneous polarization (P_{sp}) in WZ GaP. This spontaneous polarization leads to triangular potential wells at the two opposite sides of the ZB insertion, where the electrons and holes are confined. From statistical data, we found that the energy of CPQD emissions decreases linearly with the thickness of the ZB insertion due to quantum-confined Stark effect induced by the internal spontaneous polarization field P_{sp}, which is found to be $(7.02 \pm 0.19) \times 10^{-3}$ C/m^2. The nanowire CPQDs show very sharp emissions (< 75 μeV) at visible wavelengths and show single photon characteristics. Our results open up an opportunity for the realization of more complex solid-state quantum system, based on crystal phase quantum dot structures.

5.1 Introduction

Most of the bulk III-V semiconductors, including the phosphides, arsenides and antimonides of In, Ga, and Al crystalize in the cubic zincblende (ZB) structure, except for the nitrides which can also crystallize in the hexagonal wurtzite (WZ) crystal structure [167] [168]. One unique feature of semiconductor nanowires (NWs) is that they can adopt different crystal structures which do not exist in bulk [23] [128] [169] [142] [19].

The bottom-up NWs along [111] crystal direction typically exhibit a mixture of both ZB and WZ. Many recent efforts have been devoted to achieve a pure crystal phase along the whole length of the NWs. Perfect WZ crystal structures have been realized for many different III-V nanowires such as InAs [151], InP [170], and GaP [23]. On the other hand, the possibility to switch between different crystal phases within a single NW in a controllable manner is of great interest. It enables a novel gateway for band gap engineering [128, 171] and tailoring of crystal phase structures [131, 172] by the alternation of the atomic stacking sequences to switch between ZB and WZ structures.

Recently, there has been a great deal of interest on the tailoring of the crystal phase structures, such as crystal-phase superlattices [19, 154, 171], crystal-phase quantum dots/disks. In such structures, due to the difference in band gap energy of the semiconductors crystalized in the WZ and ZB phases [131, 150, 172], as well as the spontaneous polarization effect in WZ structures [173, 174], the confinement of charge carriers is achieved by solely modifying the crystal phases while keeping the chemical composition unchanged. Those structures possess some major advantages [131, 175]: (1) the structures are chemical homogeneous. (2) The interfaces are atomically sharp. (3) The lattice mismatch is almost negligible. The light emissions from those crystal phase quantum structures are thus expected to be sharp and have well defined energy which is highly desirable for quantum optics applications. The control of the crystal phase along the length of the NW, down to one or several atomic layers, is however very difficult. An InAs WZ-ZB superlattice [171, 176] has been reported with a very high level of crystal phase control. However, the characterization by optical, magneto-optical measurements was mainly performed on CPQDs in InP [131] and GaAs [172] NWs with a limited degree of position and size control. The randomness of the crystal structure along the NW length usually complicates the interpretation of the experimental data and introduces more uncertainty.

In this chapter, we demonstrate for the first time the controlled growth of atomically sharp WZ and ZB GaP nanowire sections, resulting in the formation of crystal phase-quantum disks (CPQDs) in GaP nanowires. The emission from these CPQDs is systematically studied and the spontaneous polarization in WZ GaP together with its band alignment with ZB GaP is investigated.

5.2 Experiments

In this work, GaP nanowires were grown in an Aixtron CCS-MOVPE reactor by the vapor-solid-liquid (VLS) mechanism, using gold nanoparticles as catalysts for the vapor-solid-liquid growth. A square array of gold particles (8 nm thick) was first patterned on a $(111)_B$ GaP substrate by using electron beam lithography (for 200 nm diameter and 1.2 μm pitch) or nanoimprint lithography (for 100 nm diameter and 500 nm pitch). The WZ wires were grown at 750°C using trimethylgallium (TMG) and phosphine (PH_3) as precursor gases at molar fractions of 7.4 x 10^{-5} and 1.7 x 10^{-3}, respectively (at V/III ratio of 23). The growth was performed under hydrogen chloride gas (HCl) with a molar fraction of 1.2 x 10^{-4} to suppress the radial overgrowth [27]. In order to create the CPQD structures, the growth parameters are switched during the VLS process. The growth of mixed phase WZ-ZB is carried out by reducing the temperature from 750 °C to 600 °C, while keeping the V/III ratio fixed. Pure ZB segment are achieved at 600 °C by increasing the PH_3 molar fraction from 1.7 x 10^{-3} to 1.8 x 10^{-2} and by stopping the in-situ HCl etching. The lengths of the ZB segments can be tuned by the growth time.

The crystal structures of the NWs are analyzed by transmission electron microscopy (TEM). For optical characterization of individual nanowires, NWs from as-grown samples are transferred to thermally oxidized Si wafers and mounted onto a cold finger of a He optical flow cryostat. The optical measurements were performed by a micro photoluminescence (μ-PL) and time-resolved μ-PL. We use two different excitation sources: a continuous wave diode laser (405 nm) and a pulse diode laser (420 nm) operating at one of the flowing repetition rates: 5, 10, 20, 40 or 80 MHz. The laser is focused on a spotsize of about 1 μm by a 50x microscope objective (NA = 0.45). The best spectral resolution of the CCD detector is 50 μeV and the temporal resolution of the time-correlation module is 100 ps. More details of the μ-PL setup can be found in chapter 2.

5.3 Wurtzite and zincblende GaP

Gallium phosphide (GaP) is a III-V semiconductor material, which is naturally occurring in the cubic (zinc blende) phase, with a bandgap of 2.26 eV at room temperature [177]. This gap energy is highly attractive for light emission in visible wavelength range as well as the top cell of multi-junction solar cells. However, the indirect bandgap nature of bulk GaP severely hampers its use for optoelectronic devices. Theoretical studies predicted that WZ GaP is a direct semiconductor with a band gap in the 2.12-2.25 eV range at low temperatures, [168, 178, 179]. The theoretical prediction on the direct bandgap of WZ GaP has been experimentally examined in a recent paper by Assali et al. [23]. In that work, the PL emission peak at 2.1 eV, which dominates the photoluminescence, was arguably believed to originate from band gap transition of WZ GaP. However, a recent systematic study using PL and PL excitation (PLE) measurements on higher quality WZ GaP have shed more light to the understanding the band structure of this new material. In this chapter, we only briefly discuss the PL emission of different bands of WZ GaP. A detailed investigation and discussion on band structure of WZ GaP will be presented elsewhere [180].

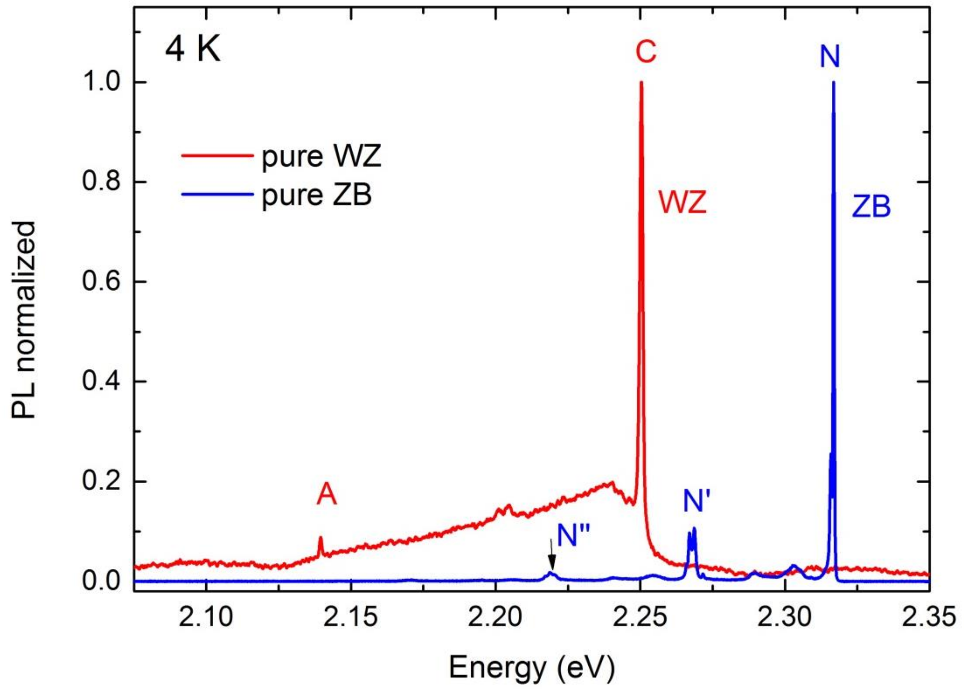

Figure 5.1. Normalized photoluminescence spectra of a single wurtzite (WZ) GaP nanowire (red) and a zincblende (ZB) GaP wafer (blue) measured at 4 K and with an excitation power of 800 W/cm^2. The emission peak denoted as N is attributed to excitons bound to isoelectronic nitrogen impurities in ZB GaP. N’ and N’’ are the first and second order phonon replica of N, respectively. WZ GaP show two bandgap related peaks at A (2.140 eV) and C (2.251 eV).

Figure 5.1 shows the normalized PL spectra of a single crystal phase WZ GaP NW and ZB GaP wafer measured at 4 K under an excitation power of 800 W/cm^2 . The strongest emission from ZB GaP is the N-line at 2.317 eV which is attributed to the exciton bound to isoelectronic nitrogen impurities [181, 182]. The energy of this line is 0.020 eV lower than the band gap, and 0.011 eV lower than the energy of the free exciton [181]. The first and second phonon replica of this line are marked as N’ and N’’, respectively. The N line has very long decay time of about 0.25 μs due to indirect gap of ZB GaP. The PL spectrum from single WZ GaP NW displays two sharp emissions at 2.140 eV (A-peak) and 2.251 eV (C-peak). The A peak has a full width at half maximum (FWHM) of 1 meV, exhibiting a long lifetime of about 70 ns from our TRPL measurement. It is also accompanied by multiple phonon replicas at lower energy. This peak is most probably coming from the A band (Γ_{8c}-Γ_{9v}) excitons bound to impurities in the WZ GaP [179, 180]. The free excitons of A band are however not observed due to the small transition matrix element. In contrast, peak C (FWHM = 1 meV), which is most probably related to the Γ_{8c} - Γ_{7v-} transition, shows free exciton behavior with a short PL lifetime of 0.7 ns. This emission from pure WZ GaP NWs is a strong indication of a direct transition. When the vertically standing NWs are measured, the B-peak (probably Γ_{8c}-Γ_{7v+}) at about 2.162 eV can also be observed. The observation of A, B, and C band from PL measurement are in line with the theoretical prediction by Bechstedt et al. [168] [179] However, the relative intensity of those peaks and the fact that only bound exciton transitions are observed for the A and B bands, and B peak only appears in certain samples, are not fully understood. In this chapter, we will mainly focus on the size and position controlled CPQDs in GaP which give sharp emissions at a well-defined energies.

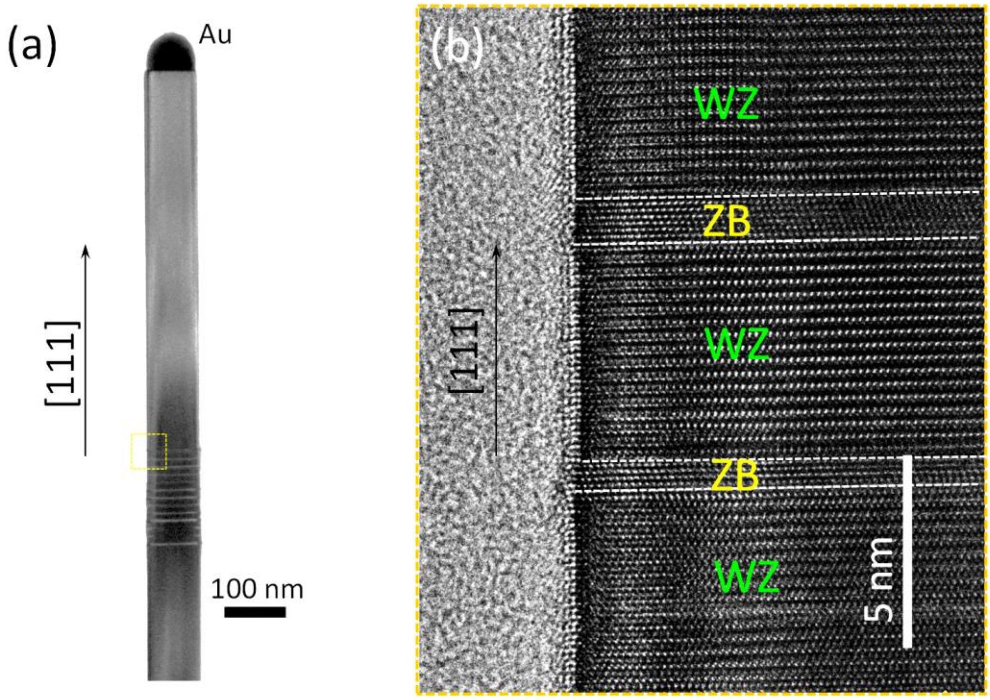

Figure 5.2. (a) Transmission electron microscopy (TEM) image of a <111> wurtzite GaP nanowire with intentional zinc blende insertions at desired positions. (b) High resolution TEM image showing the zoom-in of the boxed area in (a) with two zinc blende segments. The interface between wurtzite and zinc blende are indicated by the white dashed lines.

5.4 Spontaneous polarization

It has been theoretically predicted [173, 184-186] and experimentally verified [174, 175, 187-190] that there exist a spontaneous polarization along the singular-polar-axis in wurtzite crystal structures, even in equilibrium. In group III-nitrides the electric field induced by the spontaneous polarization can be as high as a few MV/cm [187]. While the WZ crystal structure is often characterized by lattice parameters a and c, there is an additional free internal parameter u, which is equal to the fraction of the bond length of the A and B atoms along c-axis to the lattice parameter c. In the ideal hexagonal structure ($c/a = \sqrt{8/3}$, with a bond angles of 109.47°), the internal cell parameter u takes the value of 3/8. It was pointed out that $u > 3/8$ holds for the nitrides, while $u < 3/8$ is found for all other III-V in WZ phase [173, 191]. The magnitude and sign of the parameter $(u - 3/8)$, which is the most essential parameter determining the crystal field in WZ structure, also determines the sign and magnitude the spontaneous polarization field [173].

The spontaneous polarization is not accessible for infinite bulk materials. The measurement of the P_{sp} still remains very challenging. In the presence of surfaces or interfaces, the internal spontaneous polarization field can occur due to the polarization charges. The electric field is particularly pronounced for microscopic heterostructures [174, 188, 190] and is responsible for the polarization-induced quantum-confined Stark effect (QCSE) [192]. Based on the platform of crystal-phase structures, direct detection of P_{sp} in GaAs and GaN were performed by the differential phase contrast microscopy in a scanning transmission electron microscope ($P_{sp-GaAs} = 2.7 \times 10^{-3}$ C/m^2) [190], or via the emission energies of excitons bound to different types of ZB stacking faults ($P_{sp-GaN} = -2.2 \times 10^{-2}$ C/m^2) [174].

From the Ga-P bond length and lattice parameters measured by XRD, an internal cell parameter $u = 0.37385 \pm 0.00017$ was found and a spontaneous polarization of 9 x 10^{-3} C/m^2 was predicted for WZ GaP [193]. Since the lattice mismatch between WZ and ZB structures is very small, the piezoelectric field is almost negligible compared the spontaneous polarization field. While the ZB stacking faults are much thinner than the NW diameters, we can adopt the simple plate capacitor analysis presented in reference [174, 194]. According to that approximation, the polarization sheet charge density

$$\sigma = |P_{sp}| = \frac{\Delta V \epsilon \epsilon_0}{t} \tag{5.1}$$

where $\Delta V = \Delta E/q$ is the potential difference due to the polarization sheet charges (q is elementary charge) at the two opposite sides of a ZB stacking fault of thickness t, ϵ is the static dielectric constant for ZB GaP and ϵ_0 is the permittivity of free space.

Although the experimental data on the bandgap energy of WZ and ZB are recently available, measurements of band alignment of WZ-ZB are still missing and were only predicted by theory [168, 179] with an accuracy of approximately 0.1 eV. In figure 5.3, we schematically illustrate the band profiles of a ZB insertion in a WZ NW, assuming two different types of band alignments in the presence of the spontaneous polarization induced electric field. Both the X minimum (dashed line) and the Γ minimum (solid line) are plotted. If we assume that the polarization field is sufficiently strong, the carrier confinements will be mainly determined by the polarization-induced triangular potentials [174, 194]. For type I band alignment, electrons and holes are confined in the WZ parts at two opposite sides of the ZB barrier (notice that ZB GaP has larger band gap energy than WZ GaP). For type II band alignment, however, electrons are confined in the WZ triangular well while the holes are localized in ZB segments. In those pictures, the CPQD transitions are always from carriers that are spatially separated.

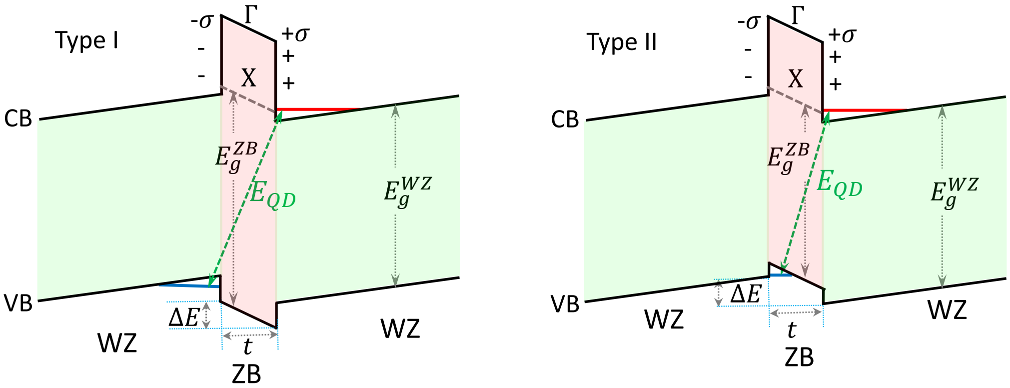

Figure 5.3. Schematic band profiles of a zincblende (ZB) insertion of thickness t in a wurtzite (WZ) nanowire assuming different band alignments: type I (left) and type II (right). The conduction band energies at X minimum and Γ point of the ZB GaP are presented as the dashed- and solid lines, respectively. The spontaneous polarization induced sheet charges σ lead to the quantum-confined Stark effect even for type I band alignment (no confinement otherwise). For both cases, the transition energy EQD is changed by an amount of ΔE as indicated.

5.5 Crystal phase quantum structures in GaP nanowires

5.5.1 Random crystal phase quantum disks GaP nanowires

We first investigate the PL emission from random CPQDs in GaP NWs. For this study, 500 nm WZ-ZB mixed phase segments in otherwise stacking-fault-free WZ GaP NWs are grown. The mixed phase segment is positioned near the top of the NWs, at about 0.5 μm from the Au seed (as shown in the inset of figure 5.4). The NWs have a total length of about 5 μm and a diameter of 200 nm. Figure 5.4 presents the low temperature (4 K) PL measurement at three different positions on a single NW of such a sample. At the base and middle of the NW, we only observe the A and C peaks at 2.140 eV and 2.251 eV, respectively. Those two peaks originate from pure WZ GaP as also observed in figure 5.1. No additional peak is found. However, when we measure the PL emission from the WZ-ZB mixed phase segment, many extra sharp lines appear below the C peak of the WZ GaP. In another μ-PL measurement on vertically standing NWs of an as-grown sample, we scan the laser spot (illuminating the NW from the side) from the top to the base. The sharp emissions are also found to be localized at about 0.5-1 μm near the top. Those measurements thus confirm that the extra emissions are from the WZ-ZB mix-phase segment.

In bulk GaP, sharp emissions can also originate from excitons bound to impurities, such as isoelectronic nitrogen [181, 182] (N-line in figure 5.1) or bismuth traps [195]. The nitrogen pairs in ZB GaP can give rise to singe photon emissions at energies below the isoelectronic impurity peaks as well [196]. However, those N-pair emissions are only observable for very high doping levels. The energy difference between the N-pair emissions and isoelectronic peak is inversely proportional to the N-N pair distance [196] [197]. The emissions observed in the WZ-ZB segment in our experiment, however, are attributed to CPQDs. This can be confirmed by considering the following points: (1) the WZ-ZB segments are not intentionally doped. (2) The sharp emissions are localized at the WZ-ZB segments and do not appear for the pure WZ GaP parts of the same NWs. (3) The statistics on the emission wavelength which we will present later, clearly shows that the emission lines are associated with WZ-ZB-WZ segment and the spontaneous polarization in WZ GaP. This point will be further elucidated later in this chapter. Additionally, a magneto PL measurement on those emissions (not shown here) exhibits a pronounced diamagnetic shift of the PL lines in the presence of magnetic field, which is a signature of CPQDs. Therefore, we can unambiguously attribute the sharp emission lines observed at the WZ-ZB segment to transitions from random CPQDs in GaP NWs.

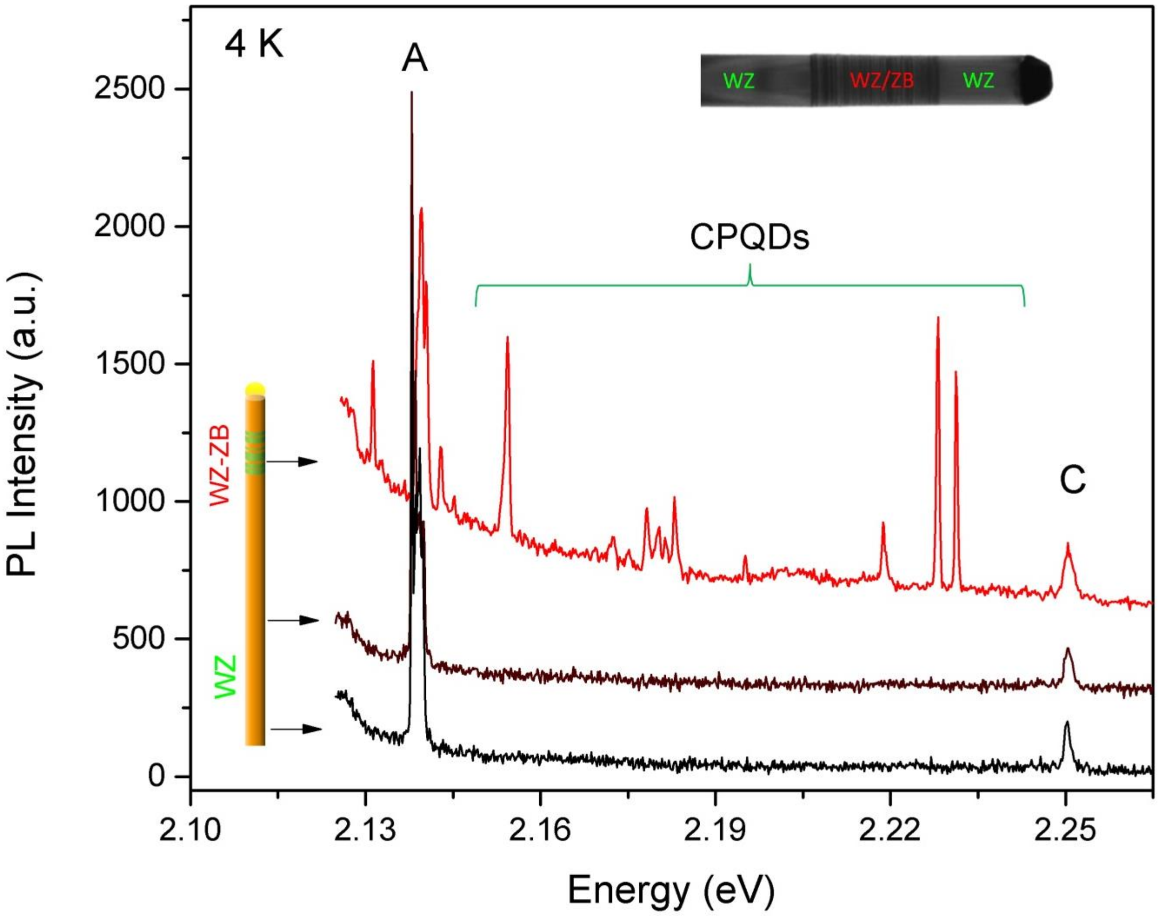

Figure 5.4. Photoluminescence spectra measured at different positions on a single GaP nanowire. The nanowire contains (~ 500 nm) wurtzite-zinc blende mixed phase segment near the top of an otherwise WZ GaP nanowire. The additional sharp emissions measured at the top of the NW are attributed to random crystal phase quantum disks.

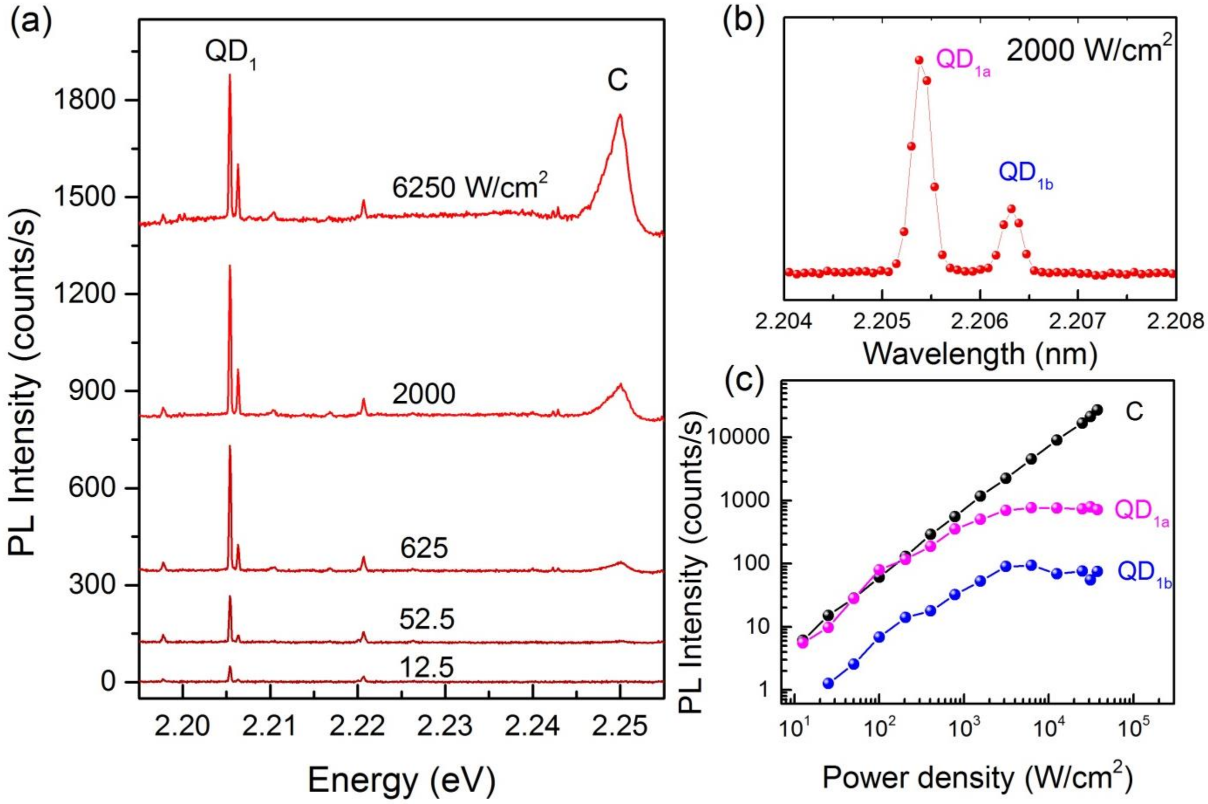

Figure 5.5. (a) Power-dependent photoluminescence spectra of a crystal phase quantum disk (CPQD) emission at 4 K. No visible shift of the CPQD PL peaks is observed in the excitation power range of 12.5 – 12500 W/cm^2. (b) The zoom-in spectrum measured at 2000 W/cm^2 shows two separate lines labeled as QD1a and QD1b. (c) Integrated PL intensity of the QD1a and QD1b lines together with the C peak are plotted against the excitation power. While the intensity of C peak increases linearly with excitation power the CPQD emissions exhibit saturation at an excitation power higher than 2000 W/cm^2.

Figure 5.5(a) presents the power dependent PL measurement on two CPQD emissions at 2.2055 and 2.2065 eV. At a low excitation power of 12.5 W/cm^2, the sharp emissions from CQPDs are clearly seen with higher peak intensity compared to the broader emission C. Interestingly, we do not observe any visible shift or broadening of the PL peaks when excitation varies 3 orders of magnitude from 12.5 to 12500 W/cm^2. When the excitation power is increased, the intensity of the two lines, QD_{1a} and QD_{1b}, increase at a similar rate and then become saturated above 2000 W/cm^2. In contrast, the peak C shows linear power dependence from 12.5 W/cm^2 up to our highest excitation power of 37.5 kW/cm^2. The observed saturation is typical for a QD emission which can only emit a single photon from each confinement level (assuming that the exciton and bi-exciton recombination energies are not identical, which is yet unknown for our CPQDs).

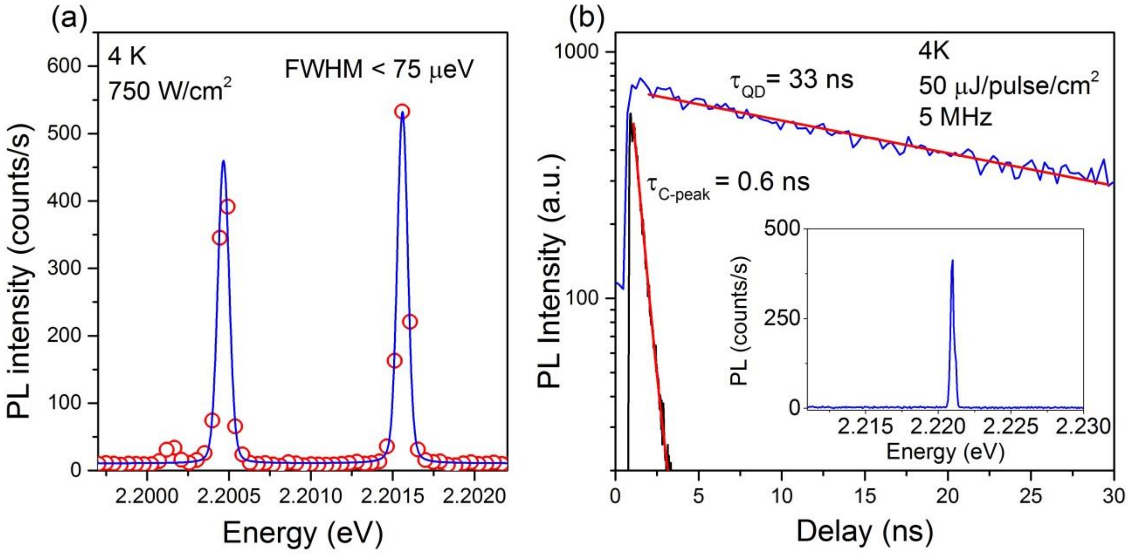

Figure 5.6. (a) PL spectrum of crystal phase quantum disk (CPQD) emissions measured at the highest spectral resolution of our setup, showing that the line-width is below 75 μeV. The solid curve presents the Voigt fit. (b) Comparison of the time-resolved PL from the C-peak and from a CPQD peak. The corresponding PL spectra of the CPQDs are plotted in the inset of (b). While the C peak shows a short decay time of 0.6 ns, the CPQD emissions at 2.221 eV exhibits long decay time of 33 ns. This long decay time is due to the spatial separation of electrons and holes which are confined at opposite sides of a stacking fault.

Two important parameters for the photons emitted from a quantum structures are its PL linewidth and PL lifetime. The low temperature PL spectrum measured at 750 W/cm^2 (figure 5.6(a)) clearly shows that the PL peaks illuminates only 2-3 pixels of our CCD detector, which is our system's resolution limit. By fitting those peaks by a Voigt function, we found a FWHM of 75 μeV. Since no broadening of the PL line is observed at higher excitation power, we believed that the actual line width is smaller than 70 μeV. In order to determine the true linewidth, another technique is needed such as using interferometry. The sharp emission is also in line with the fact that the CPQD emission has a very long lifetime of 33 ns, which is in contrast with the short lifetime of 0.6 ns observed for C peak. This lifetime of CPQD emission is several times longer than the type II transition at the interface of the WZ-ZB InP nanowires [131, 132], which might be due to the spatial separation between the electron and the hole in a CPQD or due to the small matrix element of the transitions in WZ GaP [168, 179].

One fundamental difference between the emission from WZ and ZB crystal structures is the polarization of the PL emission. Specifically, the WZ III-V semiconductors exhibit polarization perpendicular to the <111> crystal direction while the ZB shows no polarization [142, 198]. The polarization measurement of the WZ emission 2.251 eV (C peak) and CQPD emissions from a GaP NW are presented in figure 5.7. It can be clearly seen that both emission are polarized perpendicular to the nanowire axis with a degree of polarization (DOP) of 0.5 and 0.68 for the C peak and the CPQD emission, respectively. Since the transition from the hole in valence band of ZB GaP to an electron in the conduction band of WZ will not result in polarization of the emission perpendicular to the NW, our experimental data suggest that the hole is most likely confined in the WZ segment. Therefore, type I band alignment is most likely.

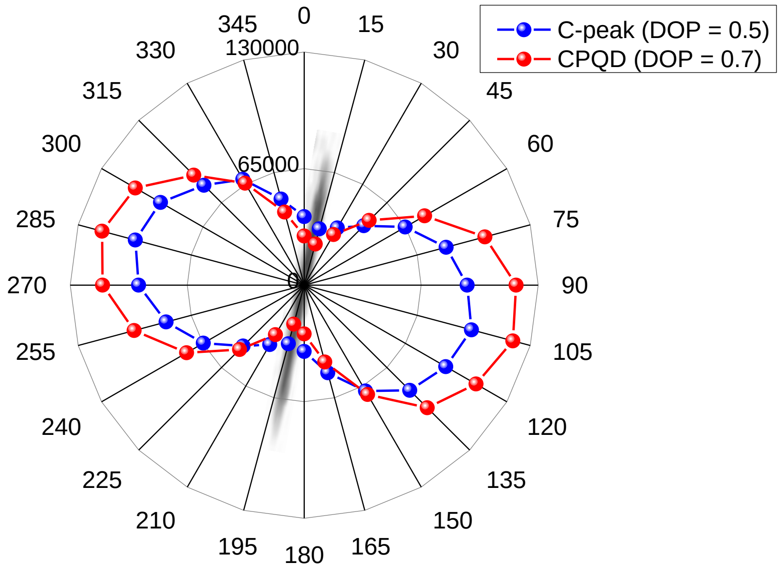

Figure 5.7. Polarization of the wurtzite C peak (2.251 eV in blue) and the crystal phase quantum disk (CPQD in red) peak at 2.220 eV in a WZ <111> GaP NW. Both of them show a polarization of the photoluminescence perpendicular to the nanowire axis with a degree of polarization (DOP) of 0.5 and 0.7 for the C peak and the CPQD peak, respectively.

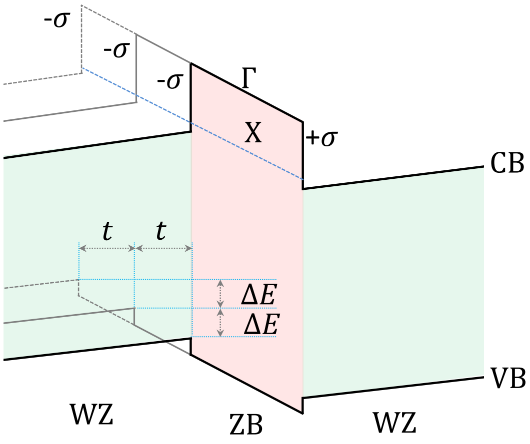

Figure 5.8. Schematic of the band profiles for different thicknesses of the zinc blende GaP insertion in a wurtzite GaP nanowire. By adding/removing one bilayer of thickness t, the resulting transition will be decreased/increased by an amount of *ΔE*.

As discussed before, the spontaneous polarization field can give rise to quantum confinement at the two opposite sides the ZB stacking fault, even if the ZB has a larger band gap than WZ and type I band alignment holds. Due to the quantum-confined Stark effect resulting from the spontaneous polarization field, the emission energy is red (blue) shifted by adding (removing) a bilayer of the ZB segment [194], as schematically illustrated in figure 5.8. In principle, the spontaneous polarization charge can be measured by the difference of the emission energies if we add or remove one bilayer. In practice, the control of the NW growth to obtain one bilayer difference is difficult. Therefore, in order to determine the spontaneous polarization of WZ GaP, we perform statistics on the emission energies of the CPQD PL peaks. We have measured the emission energies of about 340 CPQD peaks from many NWs horizontally transferred onto GaP substrates. A histogram presenting the emission energies with a binning size of 1 meV is shown in figure 5.9(a). Most of the CPQD emissions are found below the C energy band, though emissions just above the C band can also be found with a lower probability. The emissions below 2.10 eV are less frequent and have much lower intensity compared to the higher energy ones. The low probability of emissions at low energy is due to the larger spatial separation of electrons and holes by a thicker ZB segment that make the transition less favorable.

The histogram plot is analyzed by a Gaussian multiple-peak fit. The position and width of each distribution peak is plotted in figure 5.9(b). The dots represent the peak energies while error bars show the FWHM of the corresponding distribution peak. Strikingly we observe seven statistical peaks which are almost evenly spaced on the energy scale. A linear fit of the data (red line in figure 6.9(b)) indicates an average energy difference of ΔE = 22.5 ± 0.6 meV. Using equation 5.1 with ϵ = 11.1, and a 0.315 nm ZB bilayer thickness, we find P_{sp} = (7.02 ± 0.19) x 10^{-3} C/m^2. This value is higher than the theoretically predicted value (3 x 10^{-3} C/m^2) by Bechstedt [173], but is very close to a more accurate prediction using the measured c/a ratio by X-ray diffraction in combination with a density functional theory calculation (9 x 10^{-3} C/m^2) [193]. The distance between two consecutive peaks corresponds the energy difference by adding or removing one bilayer. Therefore we attribute the sharp emission lines to the quantum-confined Stark effect resulting from a strong spontaneous polarization field. The broadening of the distribution width can be explained by the random variation in the length of the WZ GaP segments in a random WZ-ZB mixed phase and the possible coupling to neighbouring QPQDs or to the substrate-induced strain when cooling down.

It is noticeable that the highest CPQD emission energy is distributed slightly (6 meV) above the C peak. This transition has smaller probability to be observed compared to the lower-energy transitions. It probably takes place across the thinnest stacking faults where tunneling of the carriers through the ZB layer can be pronounced. However, it is difficult to estimate the thinnest ZB layer thickness only from this experimental data. In this case,

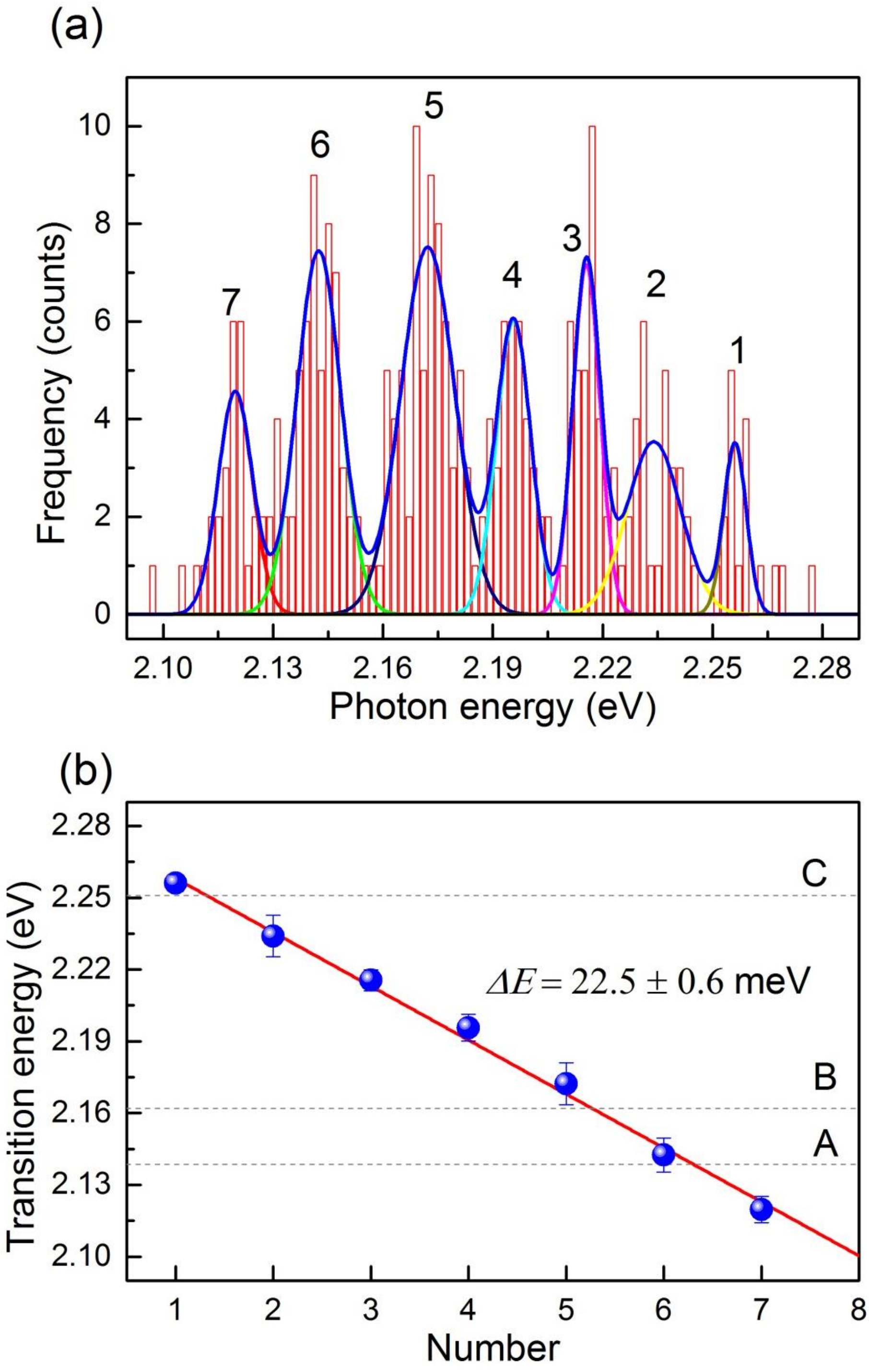

Figure 5.9. Peak energy histogram of the emission of 340 random crystal phase quantum disks (binning size of 1 meV) from different wires. The distribution is fitted with multiple Gaussians. (b) Energies of the histogram distribution peaks resulting from the Gaussian fit. The energies of the emission peaks are almost evenly spaced in energy scale with an average energy difference of 22.5 ± 0.6 meV. This is a signature of the quantum-confined Stark effect induced by the spontaneous polarization in wurtzite GaP. The A, B and C dashed lines show the position of the A, B and C peaks of pure wurtzite GaP.

a more detailed study on the quantized energy levels of electron and hole in a triangular WZ GaP quantum well is needed.

When the temperature of the system is increased, the emission from the CPQDs is quenched due to the thermal escape of electrons and holes out of the confinement potentials created by the conduction and valence band of ZB GaP. From the temperature dependence of the integrated PL intensity of a quantum disk at an emission energy of about 2.2 eV, we find an activation energy of 86.8 ± 16.0 meV (see figure 5.10)

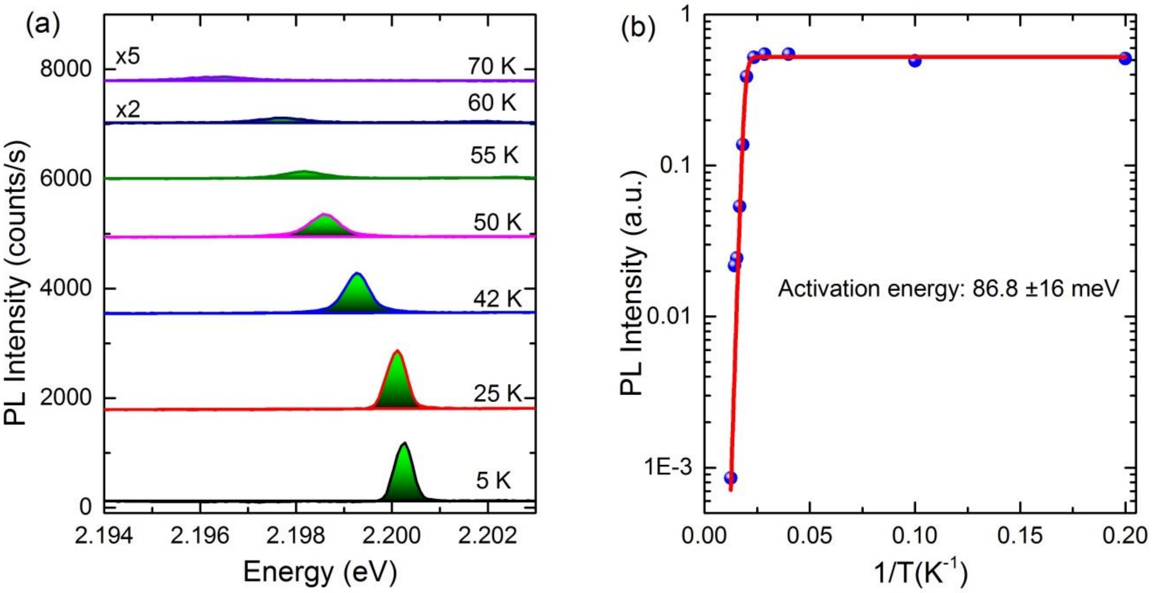

Figure 5.10. (a) Photoluminescence of a crystal phase quantum disk emission versus temperature. (b) Integrated PL intensities plotted against 1/T. The thermal activation energy is extracted from the Arrhenius-equation fit.

5.5.2 Position and size controlled crystal phase quantum disks

We now aim to improving control of the CPQDs. Precise control of the crystal phase quantum structures in terms of the position and thicknesses will first of all increase our understanding of the system and next open new possibilities for quantum device applications. We first demonstrate that the control of the crystal phase down to nearly atomic bilayers can be achieved using the GaP NW platform. Figure 5.11 presents the TEM and high-resolution TEM images of a WZ GaP NW which contains four intentionally grown ZB insertions of different thicknesses (2, 2, 7 and 27 bilayers). The ZB segments are separated by pure WZ segments of about 10 nm. The thicknesses of the ZB and WZ segments from two single nanowires are presented in figure 5.11(c), showing reproducibility. The NWs have a diameter of about 100 nm, smaller than that of the WZ GaP NW with a random WZ-ZB segment (200 nm) presented above, and a length of about 4 μm.

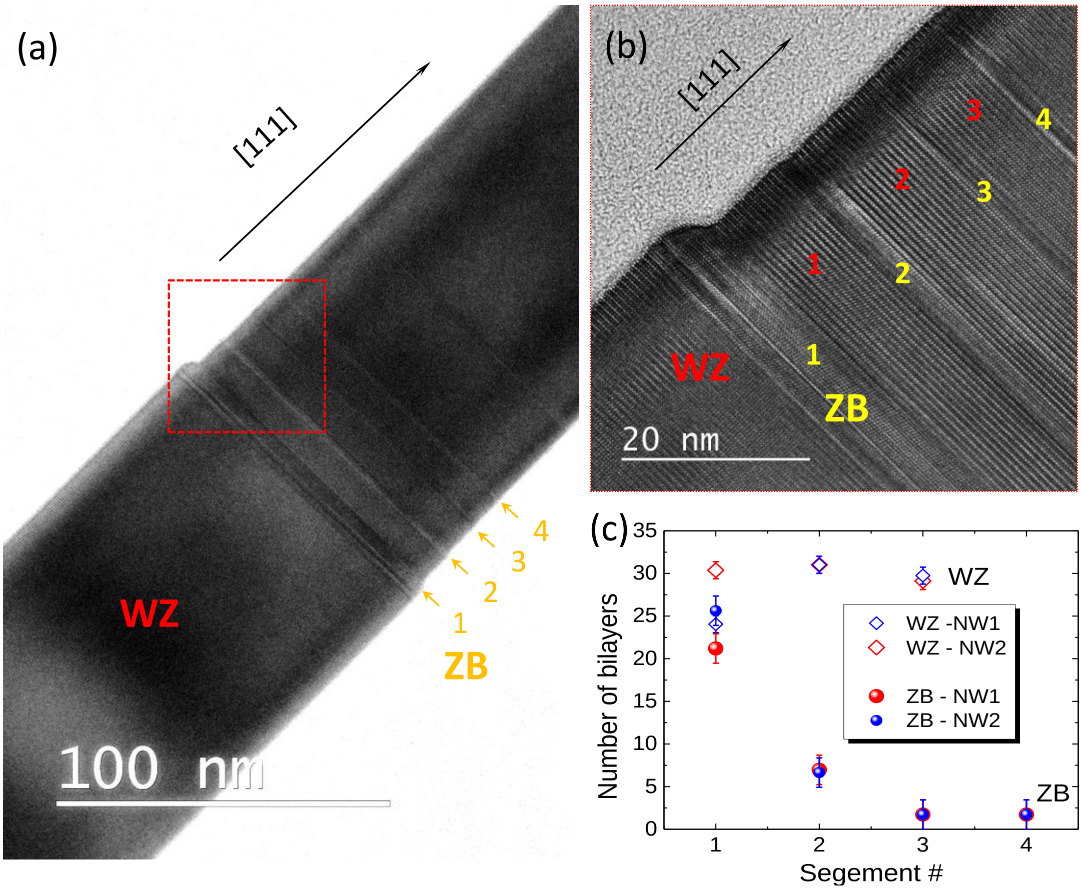

Figure 5.11. (a) Transmission electron microscopy (TEM) and (b) high-resolution TEM images of a wurtzite (WZ) GaP nanowire containing 4 zinc blende (ZB) insertions of different thicknesses. (c) Thicknesses of each zinc blende (ZB) and wurtzite (WZ) segments as labeled in (b) for two different nanowires.

In order to study the emission from the CPQDs as shown in figure 5.11, PL measurements have been carried out on horizontal NWs transferred on a thermally oxidized Si wafer. It should be mentioned here that the thicknesses of the ZB and WZ sections are expected to vary slightly from NW to NW, and can be somewhat different from the one presented in figure 5.11. The power dependent PL series show a very interesting behavior. When we gradually increase the excitation power, the CPQD emissions start to emerge, grow in intensity and gradually become saturated. Interestingly the process first takes place for the lowest energy emission and subsequently also for the higher energy ones, due to the gradual filling of the quantum states. This is due to the fact that the CPQDs are grown very close to one another (10 nm apart) and the photo-excited electrons and holes tend to occupy the lowest energy states first. No measurable shift was found for those CPQD emissions when we increase the excitation power from 7.5 to 3200 W/cm^2. This means that the screening effect, which is founded for GaN at high inject level, is negligible in our GaP NW system. At a relatively high excitation power we observe sharp emissions from all CPQDs, denoted as

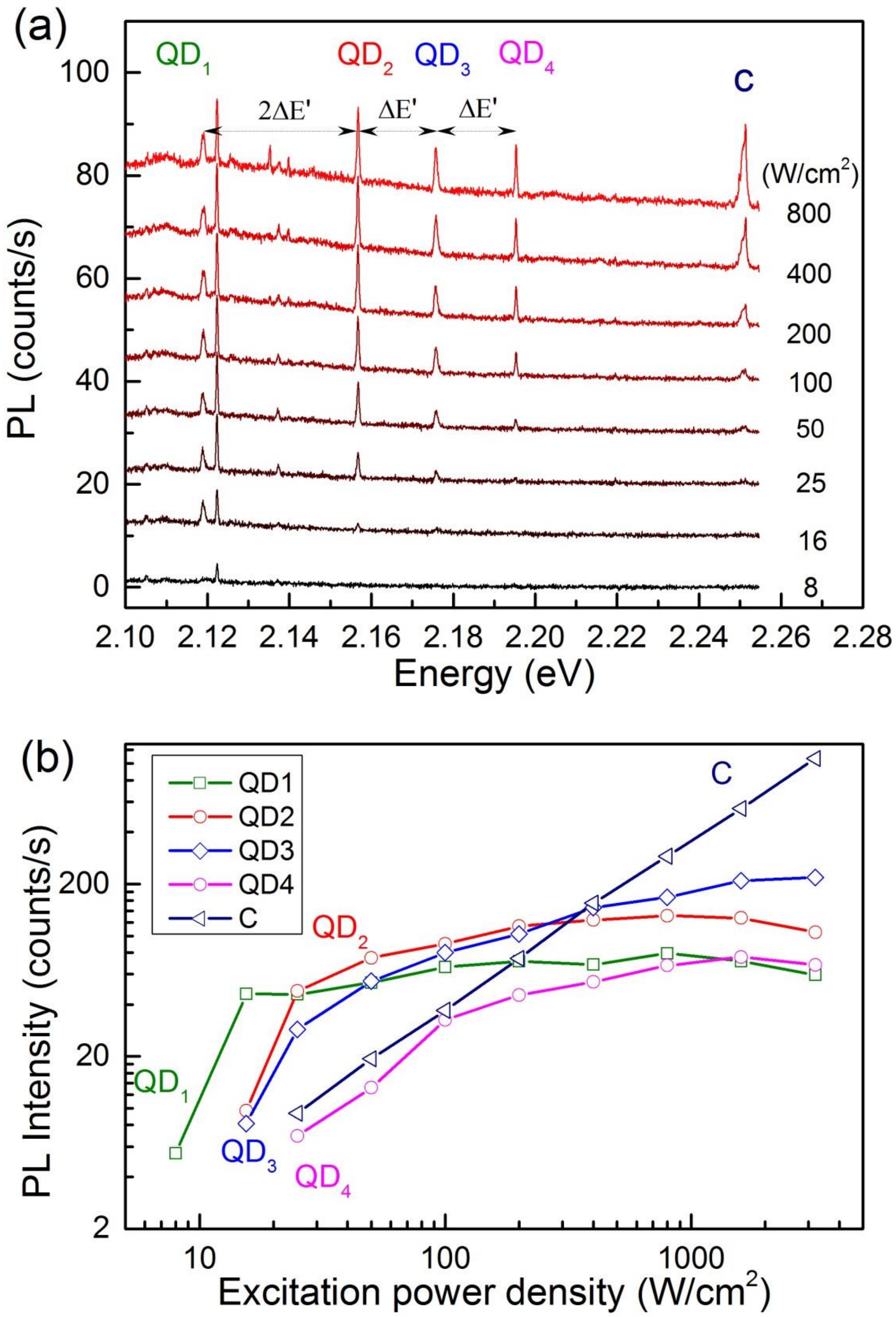

Figure 5.12. (a) Power dependent photoluminescence spectrum measured on horizontal nanowires containing 4 crystal phase quantum disks (QPQDs) of different thicknesses as shown in figure 5.11. The energetic distances between the CPQD emissions are indicated (ΔE’ = 19.05 ± 0.7 meV). (b) The integrated PL intensity of four different CPQDs as well as the bulk GaP C-peak, as a function of the excitation density.

QD_i, with i = 1, 2, 3, 4. The sharp emission at 2.1225 eV, slightly above QD_1 is probably from a nearby NW which is also excited by the laser spot. The energy spacings between the peaks QD_2, QD_3 and QD_4 to QD_1 are measured from the PL spectrum to be $4\Delta E'$, $2\Delta E'$ and $\Delta E'$ ($\Delta E' = 19.05 \pm 0.7$ meV), respectively. The spontaneous polarization is calculated to be $P'_{sp} = (5.94 \pm 0.23) \times 10^{-3}$ C/m^2. The distance between of the peak energies is slightly smaller the value we found in the statistical evaluation (ΔE = 22.5 eV). We speculate that this difference comes from the fact that the earlier measurements were carried out on random WZ-ZB segments while this measurement is based on well-defined length of the GaP segments. The change of NW diameters (100 nm versus 200 nm) and the substrate-induce strains when we cool down the horizontally transferred NW from room-temperature to 4 K may also causes the difference.

5.6 Conclusions

We have demonstrated that position and size controlled growth of atomically sharp zincblende sections in a wurtzite GaP nanowire leads to the formation of high quality crystal phase quantum disks (CPQDs) along the nanowire length. A systematic study base on photoluminescence emission of the CPQDs has revealed that the internal electric fields due to the spontaneous polarization in wurtzite GaP play a crucial role in the formation of a triangular potential well, giving rise to quantum confinement. We observe an equal spacing of the emission lines by adding or removing one bilayer of the CPQDs. The optical characterization of CPQDs shows very sharp emissions (< 75 µeV) at visible wavelengths in between the bandgaps of wurtzite and zincblende GaP with single-photon characteristics. Our results open up a gateway for realization of more complex solid-state quantum system based on crystal phase quantum structures.

Chapter 6

<100> InP nanowires for solar cells

Growth of InP nanowires (NWs) on the (100) industry standard InP substrates with pure zincblende (ZB) crystal structure is technologically relevant for nanowire solar cells and optoelectronic devices. In this chapter we demonstrate that the InP NWs grown along <100> direction are pure ZB regardless the use of the in-situ dopants. By means of the optical characterizations, the doping concentration in sulphur-doped (n-type) <100> InP NW can be estimated and compared with the value from electrical measurements. Additionally, we show that sulphur can enhance the quantum efficiency by passivating the NW surface. In contrast, Zn-doped <100> InP NWs show lower optical quality and complicated doping behavior with the coexistence of both interstitial and substitutional Zn. By thermally annealing the Zn-doped sample after the growth, interstitial Zn becomes substitutional and a higher quality of p-doped InP NWs can be obtained.

6.1 Introduction

InP nanowires (NWs) are promising for optoelectronics devices such as light-emitting diodes [18, 124], photodetectors [4], single photon emitters [69], and photovoltaics [8, 60, 75, 76]. They are most frequently grown on (111) substrates, due to the lower free energy of this surface, which favors the formation of vertical NWs [199, 202]. However, due to the stacking nature along this crystal direction, the bottom-up growth of <111> NWs often result in a high density of planar stacking faults. Even though the formation of stacking faults can be exploited to create new structures [19, 154, 176, 203] and to explore new physics [168] [131] [172], they can significantly affect the electronic and optical properties of NWs. Recently, electrical measurements on NW FET devices [111], and terahertz spectroscopy studies [110, 112] on doped and intrinsic InP NWs have revealed carrier mobilities of 200-700 cm^2/Vs, despite the low surface recombination velocity (SRV) of <111> InP NWs [110]. Those values are much lower than that of bulk InP [204] and are attributed to the trapping and scattering of carriers at these stacking faults [110-112].

If NWs grow vertically on a (100)-oriented substrate, they grow along a (100) axis, in which it is difficult to form stacking faults [137, 138, 205]. Despite the challenges in achieving growth in this unfavorable direction, it offers an opportunity to grow defect-free ZB InP NWs on <100>-oriented industry standard substrates. In addition, <100> nanowires feature completely flat and smooth side-facets which is important for reducing surface recombination losses. Numerous studies on III-V NWs on (100) substrates have been presented recently [137, 138, 205-207]. The vertical yield of NWs can be significantly increased by carefully controlling the NW nucleation step [205]. A study on the morphology and the vertical yield of <100>InP NWs on a <100> oriented substrate was presented in reference [208]. The study on the effect of dopants on the electrical and optical properties of <100> InP, which is essential for device fabrication, is however still very limited.

In this chapter we demonstrate that InP NWs grown along <100> direction are pure ZB despite the use of *in-situ* dopants. By using micro-photoluminescence (PL) and time-resolved PL measurements the effect of sulphur dopants on optical properties of NWs is investigated. The doping concentration of n-type <100> InP NW is estimated from the band filling effect. The p-doped <100> InP NWs show a complicated doping behavior with the coexistence of both interstitial (donor) and substitutional (acceptor) Zn in the NW lattice. The fraction of substitutional Zn over the total Zn dopant density can be improved by thermal annealing after the growth, yielding a better quality of p-doped InP NWs. Finally, measurements of the surface recombination velocity (SRV) in <111> and <100> intrinsic InP NWs will be presented.

6.2 Experiments

In this work, all the <100> InP NWs are grown on (100) InP substrate in a shower head MOVPE reactor (Aixtron CCS) using trimethylindium (TMIn) and phosphine (PH_3) as indium and phosphorous precursors, and gold droplets as catalysts. The growth temperature of all the samples is kept at 500 °C (unless otherwise mentioned). Two lithography techniques were employed to predefine the positions of the Au particles on (100) InP substrates [208]: electron beam lithography (EBL) to fabricate small array (25 x 25 NWs), and nanoimprint (NIP) for large-scale NW arrays. The EBL pattern contains various diameters from 25 nm to 100 nm and pitches from 0.3 µm to 5 µm, and the nanoimprint patterns yield Au disks with a diameter of 139 nm and a pitch of 513 nm. H_2S and DEZn are introduced with molar fractions $\chi_{H2S} = 4.2 \times 10^{-8}$ to 4.2×10^{-6} and $\chi_{DEZn} = 4.8 \times 10^{-7}$ as precursors for n-type and p-type dopants, respectively. Radial growth was suppressed by introducing HCl (15 sccm) during growth.

The as-grown samples are examined by scanning electron microscopy (SEM). The crystal structure is studied by transmission electron microscopy (TEM). For PL and TRPL measurements of individual NWs at various excitation conditions and temperatures, the NWs were broken off and transferred to Si substrates and mounted onto the cold finger of a He flow cryostat. The time integrated PL measurements were carried out using a 635 nm CW diode laser. TRPL is measured by 635 nm diode laser pulses at 40 MHz. The PL signal is excited and collected by the same optical objective (100x, NA = 0.7). The details of PL setup were presented in chapter 2 and 3.

6.3 <100> InP nanowires for solar cells

6.3.1 Crystal structure of <100> InP nanowires

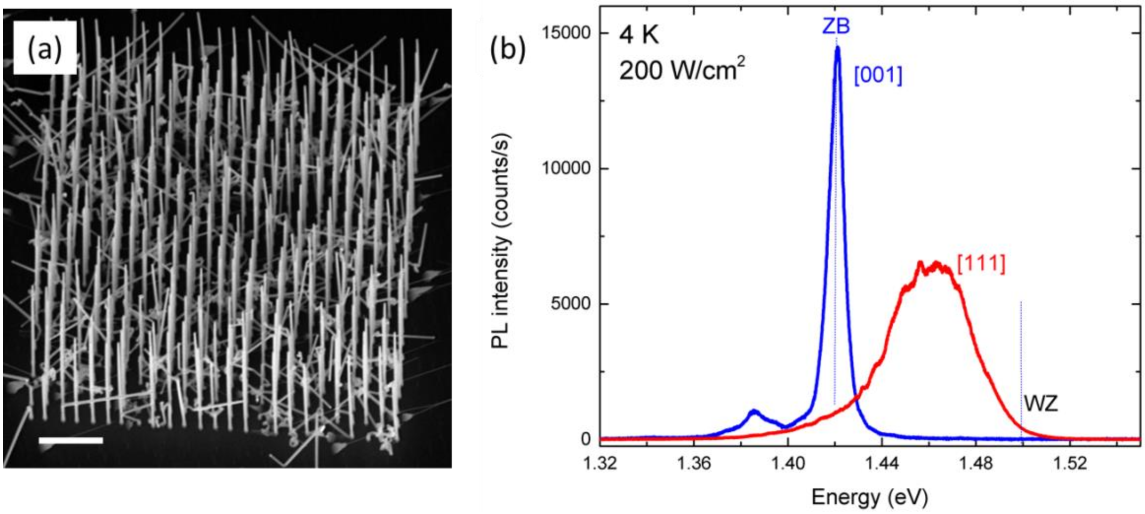

Figure 6.1. (a) Scanning electron microscopy image of InP NWs grown on (001) substrate (30^o tilted view). The sample consists of both <100> and <111> InP NWs. (b) Low temperature (4 K) photoluminescence spectra of <100> and <111> InP NWs from the sample shown in (a) which are measured at the same conditions. The <100> NW exhibits a sharp zinc blende band gap-related peak at 1.42 eV and a conduction band/donor to acceptor transition at 1.385 eV indicating pure zinc blende crystal structure, while the <111> wire shows a broad emission coming from a mixed wurtzite-zinc blende crystal phase.

Figure 6.1(a) presents a SEM image of an InP NW sample grown by a square array of 100 nm Au with a pitch of 500 nm at 500 °C. The sample shows both vertical and tilted InP NWs with a majority of the NWs grown along <100> direction. Low temperature PL measurements on single NWs of this sample (figure 6.1(a)) shows two different NW categories. The first category exhibits a sharp ZB bandgap emission at 1.42 eV [137] accompanied by residual donor/conduction band to acceptor transitions at about 1.385 eV. These NWs with only ZB peaks are pure <100> oriented InP. The second NW category exhibits a very broad PL emission between ZB and wurtzite (WZ) band gaps. The second category NWs are attributed to <111> InP NWs, since these growth conditions generally results in WZ with ZB stacking faults for <111> InP NWs (see also chapter 3). The PL measurements can thus be used to distinguish <100> InP NWs from <111> InP NWs when they are randomly transferred to a different substrate.

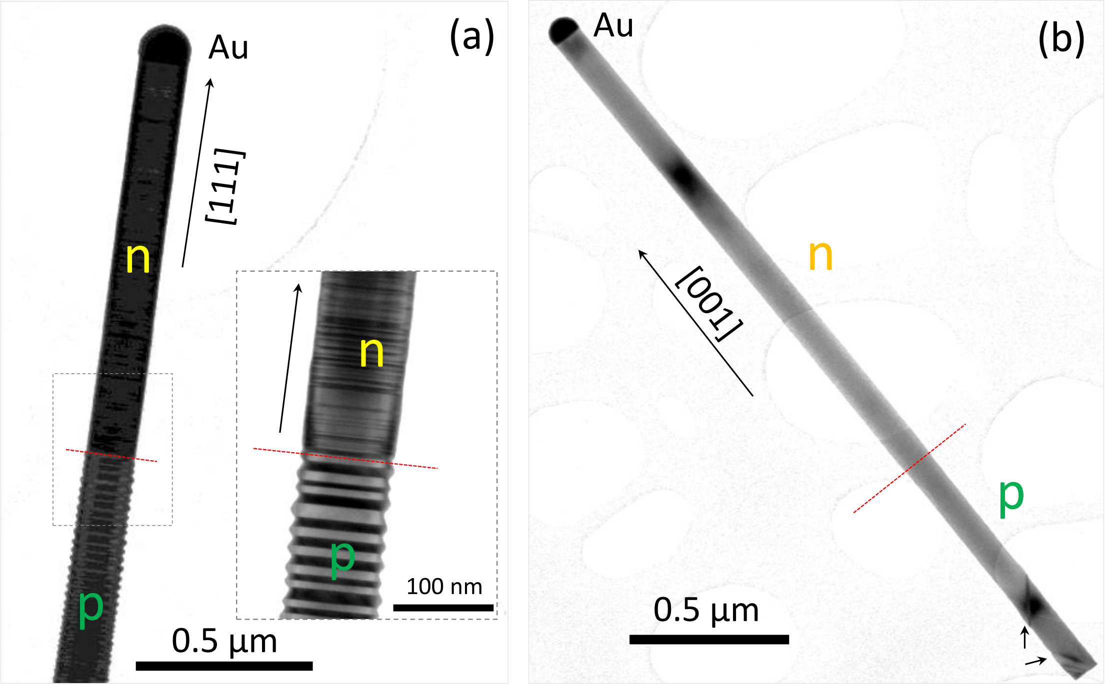

Figure 6.2. Transmission electron microscopy images of (a) <111> p-n junction and (b) <100> InP p-n junction. The n-part of the <111> NW is mainly wurtzite with random zincblende stacking faults; and the p-part is mainly zincblende with twin planes. In contrast, the <100> p-n NW shows no stacking fault (except two twin planes near the base of the NW as indicated by two short arrows). The p-n interfaces are marked by the red dashed lines. The p-n interface position of the <100> NW, which is not visible in TEM image, is estimated based on the growth times of the p- and n-parts.

As discussed above, the stacking faults and twin planes can trap and scatter carriers and significantly influence the carrier mobility [111, 112, 133, 134]. The stacking-fault-free nature of <100> InP NWs are therefore of importance for many applications which require crystal phase purity. Figure 6.2 presents TEM images of p-n junctions encoded in a <111> and a <100> InP NW, respectively. The <111> p-n junction have a sulfur-doped (n-type) part predominated by WZ with random ZB stacking faults, and the Zn-doped (p-type) part is ZB with many twin planes. The <100> InP p-n junction, in contrast, exhibits a ZB crystal structure with no WZ stacking faults. The position of the p-n interface is clearly seen for <111> NW by the contrast in the TEM image, due to the different crystal structures. The p-n interface of <100> InP NW is not visible in the TEM image since it is a single crystal phase. The interface can be approximately determined by the growth times. In order to gain more understanding on the effect of each type of dopants on the optical properties of the <100> InP NWs, n-doped and p-doped NWs are fabricated separately.

6.3.2 Doping of <100> InP nanowires

6.3.2.1 Sulphur-doped InP nanowires

The effect of *in-situ* suphur and zinc doping on the vertical yield, the morphology, the diameter and the growth rate of <100> InP NWs grown in our group, were presented in reference [208]. Here, we mainly focus on the optical properties of suphur- and zinc-doped <100> InP NWs. Figure 6.3 presents power dependent PL spectra of a single S-doped InP NW at a H_2S molar fraction of 4.2 x 10^{-7}. The PL spectrum shows a strong emission near the ZB bandgap (~ 1.417 eV) at an excitation density above 0.3 W/cm^2. This PL emission peak is attributed to a convolution of band-to-band transitions and the shallow donor to valence band transitions. The shallow donor to valence band transition should be about 5 meV below the band-to-band peak. However they are broadened due to intentional S dopants and are not clearly resolved. We will regard this peak as bandgap-related peak from now on. The second PL peak at 1.38 eV comes from the superposition of radiative transitions between the conduction-band to unintentional acceptors as well as due to donor-acceptor pair recombination, which are only clearly seen at low excitation powers. At an excitation power density above 100 W/cm^2 the bandgap related peak shows a pronounced blueshift due to band filling.

As discussed in chapter 4, the internal quantum efficiency (IQE) of the PL emission from NWs can be extracted by measuring the integrated PL intensity I_{PL} as a function of excitation power density P_{laser}. By fitting the following equation $P_{laser} = P_1\sqrt{I_{PL}} + P_2 I_{PL} + P_3 I_{PL}^{3/2}$, the radiative quantum efficiency as a function of excitation power density can be calculated as $\eta = I_{PL}P_2/P_{laser}$ [96]. P_1, P_2, and P_3 are three fitting parameters. The internal quantum efficiency of the S-doped InP NW are extracted and plotted as the solid dots in the figure 6.3(b). For comparison we performed a similar measurement on a typical intrinsic NW fabricated at the same growth conditions as the n-doped one but without the use of the H_2S doping precursor. The internal quantum efficiency of the intrinsic NW is presented as open dots in figure 6.3(b). It can be seen that the quantum efficiency of the S-doped <100> InP NW is much higher than that of the intrinsic NW at low excitation powers (< 1000 W/cm^2). When the excitation power is higher than 1000 W/cm^2 the non-radiative channels are saturated and the PL efficiencies of both nanowires are comparable. This indicates that the S dopant enhances the radiative processes [209] in the <100> InP NWs.

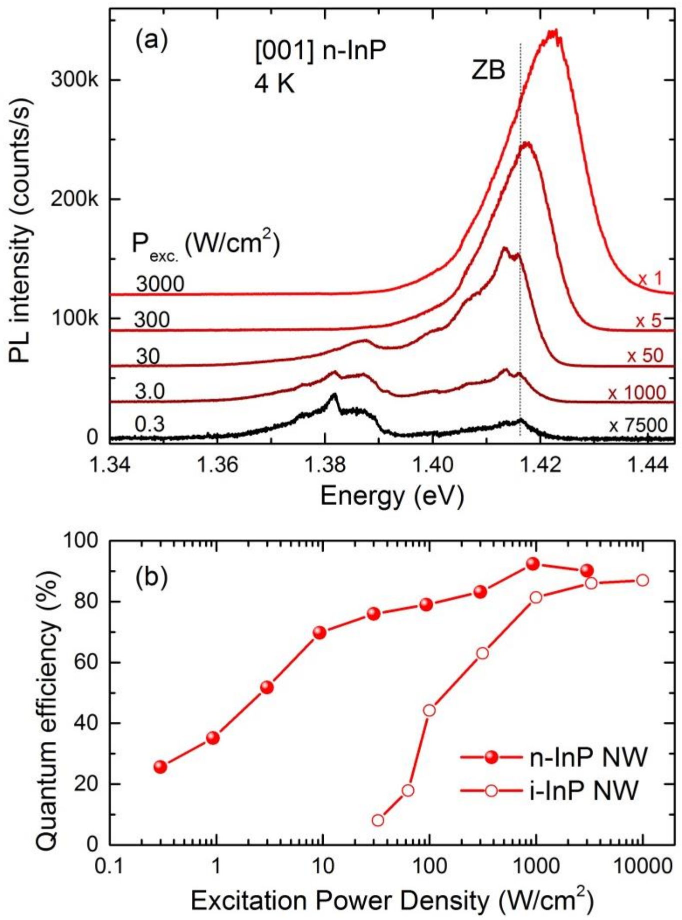

Figure 6.3. (a) Power-dependent photoluminescence spectra of S-doped (n-type) <100> InP NWs (χ_{H2S} = 4.2 x 10^{-7}). (b) Internal quantum efficiency (IQE) of S-doped <100> InP NW as a function of the excitation power density. The intrinsic InP NW fabricated at a similar growth condition but without any intentional doping exhibits a much weaker IQE, as compared to the S-doped one.

In order to quantify the doping concentration, the normalized PL spectra from different samples with H_2S molar fraction varying in the range from 4.2 x 10^{-8} to 4.2 x 10^{-6} are measured and shown in figure 6.4(a). The measurements were carried out at room temperature. The PL peak blueshifts as the doping concentration is increased. The energetic difference between the PL peak of the doped (E) and undoped (E_0) samples ($\Delta E = E - E_0$) is a function of χ_{H2S}. It should be noticed for intrinsic <111> InP NWs that PL emission exhibits a blue shift from ZB peak toward WZ peak due to the quantum confinement at the WZ and ZB sections of the mix phase nanowire, as seen in figure 6.1(b). The introduction of n-type dopants causes an additional blue shift due to Burstein-Moss effect [210]. Therefore for <111> InP NWs it is difficult to distinguish the effect of dopants and the crystal phase mixing on the PL shift. Different from the <111> InP NWs, the PL blueshift of S-doped <100> InP (pure ZB crystal structure) is solely from the increasing sulphur concentration. Therefore, we can unambiguously attribute the blue shift to the Burstein-Moss effect resulted from n-type doping [210]. The shift is even visible at a low doping level of 10^{17} cm^{-3} due to the small effective mass of the electrons in the conduction band. Therefore, the doping concentration can be estimated based on the measured shift of the PL peak, using the equation $\Delta E = \frac{16.9}{m^*} \times \left(\frac{n}{10^{19}\mathrm{cm}^{-3}}\right)^{2/3}$ (meV) (6.1) [210] [211], where we neglected bandgap renormalization, which is a small correction in n-type InP. Here, m^* is the effective electron mass and n is the doping concentration of the NW. The calculated values of n as a function of χ_{H2S} are plotted in figure 6.4(b). Electrical measurements on three single NW field effect transistors (FETs) at χ_{H2S} = 4.2 x 10^{-7} [208] (fabricated and measured at TU Delft) show a doping concentration of (2.5 ± 0.1) x 10^{17} cm^{-3}. This is two times higher than the value estimated from our PL measurement using equation 6.1. The PL measurements can thus be used as a quick and quantitative method to estimate the S doping concentration within the n-type <100> InP NW.

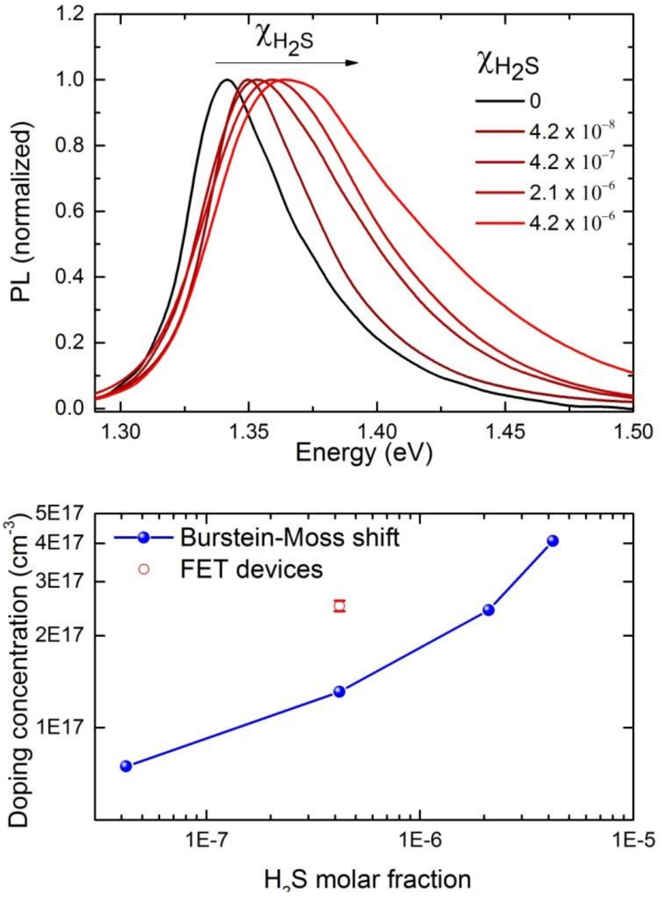

Figure 6.4. (a) Room-temperature photoluminescence (PL) spectra as a function of H_2S molar fraction. The PL from intrinsic InP nanowire (black curve) is for reference. The PL peak shift is attributed to the Burstein-Moss effect coming from S dopants. (b) Doping concentrations are estimated from the PL peak shift and plotted as the blue dots (the blue solid lines are the guides to the eye). The red dot shows the doping concentration of (2.5 ± 1.0) x 10^{17} cm^{-3} from electrically measured by fabricating FET devices fabricated by using S-doped <100> InP nanowires (χ_{H2S} = 4.2 x 10^{-7}) [208].

The effect of S-doping on the optical quality of an InP NW is further investigated by varying the H_2S molar fraction. Figure 6.5 presents the average (over 10 NWs per sample) integrated PL intensities and PL lifetimes at various sulphur doping concentration (estimated from the Burstein-Moss shift for different H_2S molar fractions). It is clearly seen that by increasing the doping concentration from 7.4 x 10^{16} to 4 x 10^{17}cm^{-3} (or molar fraction of H_2S from 4.2 x 10^{-8} to 4.2 x 10^{-6}), the PL intensity increases 5 times and PL lifetime increases from 0.24 ns to 0.51 ns. A systematic study by Rosenwaks *et al.* [212] has pointed out that room temperature recombination in bulk n-InP is dominated by the radiative process (Schockley-Read Hall recombination on n-type impurity has very long lifetime compared to the band-to-band radiative one). For our <100> n-InP NWs, the carrier lifetime is strongly affected by the surface recombination (see section 6.3.2 and chapter 2). Therefore, the enhancement of the integrated PL intensity and carrier lifetime can be attributed to the surface passivation effect of sulphur, which is well known for InP [209, 213].

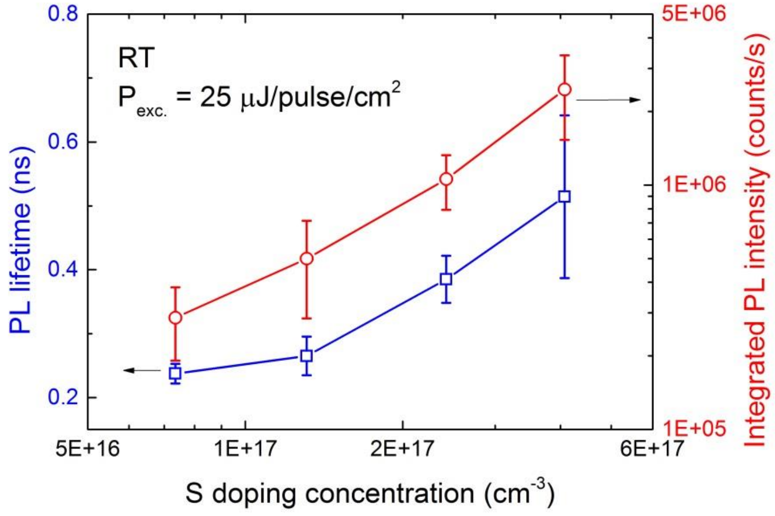

Figure 6.5. Right-axis: Room-temperature integrated photoluminescence (PL) and Left-axis: PL decay times of the S-doped <100> InP NW samples as a function of the sulphur doping concentration. The lines connecting the data points are the guides for the eyes.

6.3.2.2 Zinc doped <100> InP nanowires

Zn is one of the most widely used p-type dopants in InP and its related compounds, which are important for many optoelectronic devices. Zn doping is usually introduced by two methods: thermal diffusion [214, 215] and *in-situ* doping [216, 217]. In our study, Zn dopants are incorporated *in-situ* during NW growth. It is experimentally demonstrated that the verticality of InP NWs on a (100) substrate increases with increasing DEZn molar fraction from 4.8 x 10^{-8} to 2.4 x 10^{-5}. Too high DEZn flow, however, will affect the morphology and stops the NW growth [208]. The determination of Zn-doping concentration in NWs by electrical measurement is difficult compared to S-doped InP because the electrical contacts to p-type InP NWs are usually highly non-ohmic. The Burstein-Moss shift is also much smaller in p-type InP due to high effective mass of the hole and is of similar magnitude but has the opposite sign to bandgap renormalization [218]. Optical measurements, however, will provide us detailed insight into the electronic states of the Zn dopants.

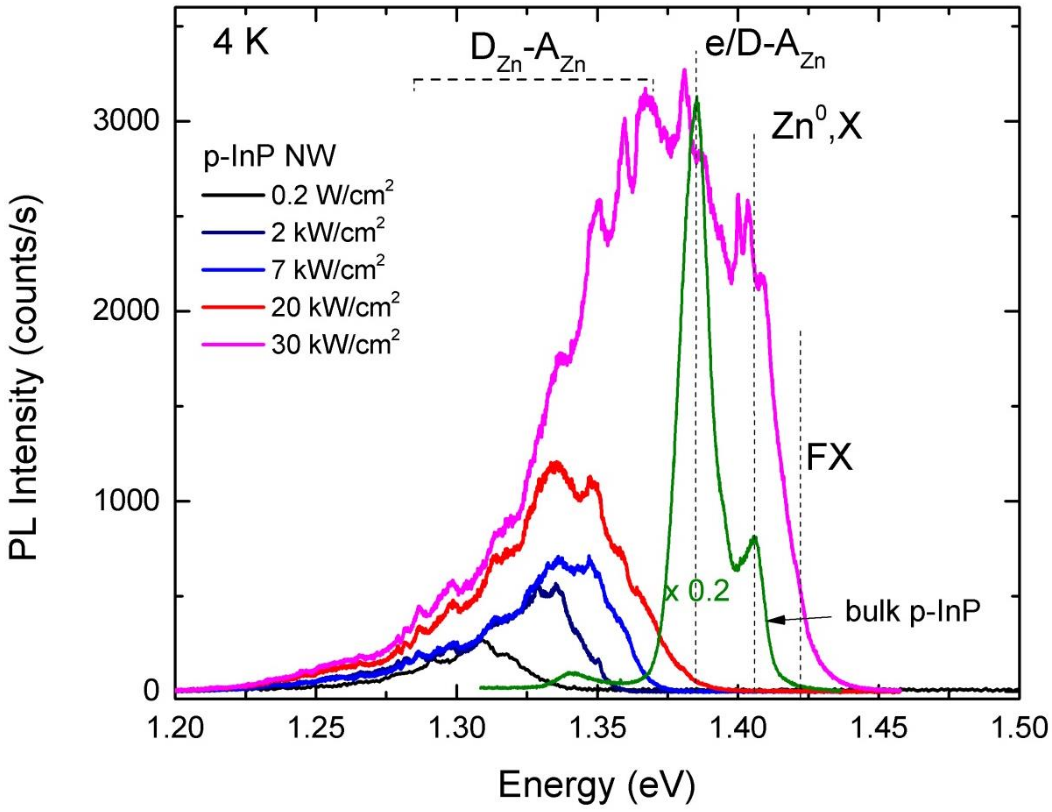

Figure 6.6. Power dependence photoluminescence (PL) spectra of a Zn-doped <100> InP NW (χ_{DEZn} = 4.8 x 10^{-7}) measured at 4 K. The PL spectra are broad and the PL efficiency of Zn-doped NW is about one order of magnitude lower than for the n-doped <100> InP NWs at the same excitation condition. The broad emission at low energy region (< 1.37 eV) come from interstitial to substitutional Zn transitions in the NWs.

Figure 6.6 presents 4 K PL spectra of a Zn-doped InP wafer (doping concentration of 10^{18} cm^{-3}) and Zn-doped (100) NWs grown at 500 °C, and χ_{DEZn} = 4.8 x 10^{-7}. The p-InP substrate, shown as a reference, shows a strong electron/donor to Zn acceptor (e/D-A_{Zn}) emission at 1.385 eV and an exciton bound to neutral acceptor (Zn,X) peak at 1.406 eV. No PL peak at lower energy was observed except the longitudinal optical phonon replica of the e/D-A_{Zn} at 1.34 eV. The bulk p-InP PL peaks do not shift considerably with the excitation density in the range 0.2-30 kW/cm^2. Different from the bulk p-InP, the PL spectrum from the p-InP NW is extended towards the low energy range and the PL efficiency is almost one order of magnitude lower than that of the S-doped NWs. At an excitation density of 200 W/cm^2, only an emission peak at energy of about 1.309 eV is observed. The peak at about 1.38 eV, which corresponds to a conduction band to Zn acceptor (e-A$_{Zn}$) transition, or to a transition from unintentional donors to Zn acceptors (D-A$_{Zn}$) is not visible below 7 kW/cm^2. When the excitation density increases, this low-energy PL peak blue shifts toward the ZB bandgap.

The PL peak in the range of 1.20 – 1.37 eV, which blue shifts with increasing excitation power, can be attributed to the optical transitions between substitutional and interstitial Zn. The substitutional Zn acts as an acceptor while the interstitial Zn act like a deep donor [214, 216, 217]. In order to understand the shift of the PL peak, we consider the energy of the transition at different excitation density regime. We adopt the explanation from reference [214], assuming that the transition takes place between electrons and hole of a D$_{Zn}$-A$_{Zn}$ pair which are separated by a distance r. In order to create a free electron in conduction band and a free hole in the valence band, an energy of E_g is needed. When the electron neutralizes a Zn donor, an energy of $E_{D_{Zn}}$(ionization energy of interstitial Zn) is released. However a potential energy of $e^2/\epsilon r$ is added to the system due to the coulomb interaction between the ionized acceptor and the added electron. When a hole comes and neutralizes the ionized acceptor of the system, only energy of $E_{A_{Zn}}$(ionization energy of a Zn acceptor) is released because the hole is not affected by the neutralized donor. The energy of the emitted photon ends up as being $h\nu = E_g - \left(E_{A_{Zn}} + E_{D_{Zn}}\right) + e^2/\epsilon r = E_{min} + e^2/\epsilon r$ (6.2) as presented in reference [214]. When the excitation density increases, the distance between the donors and acceptors between which the transitions takes place, decreases due to higher carrier concentration. The D$_{Zn}$-A$_{Zn}$ peak therefore blue shifts with increasing excitation density. Since the decay time is dependent on the spatial distance between the D$_{Zn}$ and the A$_{Zn}$, we expect a longer carrier lifetime for a larger r, or equivalently lower energy transition. From the TRPL measurements (not shown here) we indeed found that the D$_{Zn}$-A$_{Zn}$ transition at low energy of 1.27 eV has a long lifetime of 10-15 ns while a higher D$_{Zn}$-A$_{Zn}$ energy emission at 1.33 eV shows a shorter lifetime of about 2 ns. The e/D-A$_{Zn}$ emission at 1.385 eV exhibits a decay time of 1 ns.

In order to qualitatively estimate the binding energy $E_{D_{Zn}}$of the Zn donors, we plot the position of the D$_{Zn}$-A$_{Zn}$ peak for a p-doped <100> InP NW as a function of the excitation power density in semi-logarithmic scale (figure 6.7). The PL peak shift coefficient of 27 meV per decade change in excitation power density is found by linearly fitting the experimental data in figure 6.7. We extrapolate the ground state of the D$_{Zn}$-A$_{Zn}$ peak to approximately 1.233 eV. The binding energy of interstitial Zn donor is thus found to be 149± 0.5 meV. This value is similar to the energy of the D$_{Zn}$-A$_{Zn}$ peak of bulk Zn-doped InP measured at low excitation power, as presented in reference [219].

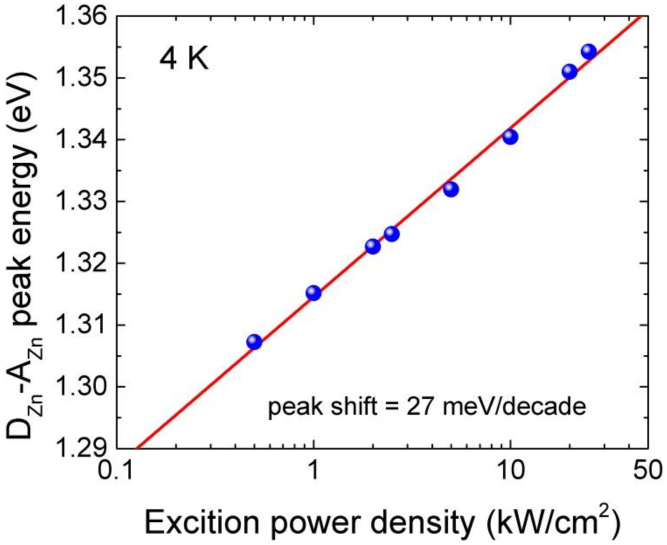

Figure 6.7. Energy of D_{Zn} –A_{Zn} peak of a Zn-doped <100> InP nanowire as a function of excitation density. The dots present experimental data and the straight line is a fit. The energy shift coefficient of 27 meV per decade change in excitation power density is found.

Since we intentionally use Zn as p-dopant, the existence of interstitial (donor) Zn will compensate the substitutional (acceptor) Zn, resulting in a hole concentration, which is much lower than the Zn concentration. Moreover, deep level interstitial Zn is a source of non-radiative [160, 219] recombination and degrades the material quality. That also explains the low PL efficiency of our p-doped <100> InP NWs. In bulk InP, Zn diffusion can result in a high amount of interstitial Zn [217, 220]. *In-situ* doping usually leads to lower interstitial Zn concentration. The reason for the high amount of interstitial Zn in our <100> InP NWs is not clearly understood though. Different from Zn-doped <100> InP NWs, PL measurement on <111> p-InP nanowire grown at a similar conditions (for our <111> InP NW solar cells) exhibits a PL spectrum similar to that the p-InP wafer with dominant e/D-A_{Zn} peak (1.385 eV). This is probably due to the difference in the incorporation of Zn into <100> and <111> InP NWs [221]. In order to increase the amount of substitutional Zn, thermal annealing of the sample is most commonly used in bulk. During the thermal annealing, the interstitial Zn becomes subsituational Zn [214, 217, 222]. Figure 6.8 presents the typical PL spectra of single NWs at 4 K from two samples grown at the same conditions, with and without the annealing step at 600 °C for 10 mins. The annealing is performed *in-situ* after the NW sample is grown. It can be seen that the annealed NWs show a PL peak at the e/D-A_{Zn} transition while the sample without annealing shows dominant PL from substitutional Zn. The average integrated PL intensity also increases 1.5 times after the annealing. Therefore thermal annealing can be used to improve the quality of p-doped sample when the interstitial Zn concentration is too high.

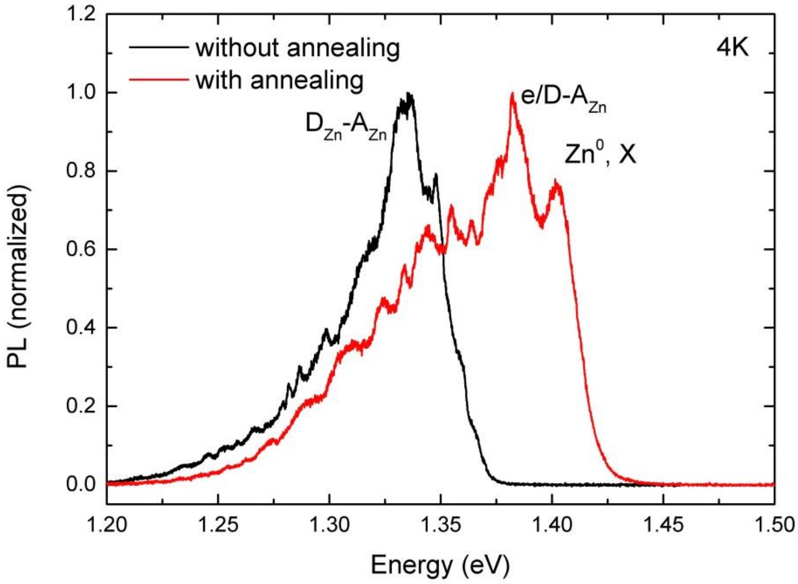

Figure 6.8. PL spectra of Zn-doped <100> InP NWs (a) before and (b) after annealing at 600 °C. The measurements were carried out at an excitation power of 2 kW/cm^2, at 4 K.

6.4 Surface recombination velocities

Due to the small dimensions of NWs, the influence of the surface recombination on the optical and electrical properties of the NW becomes very important. Here we present a measurement of surface recombination velocities of intrinsic <111> and <100> InP NWs. All the NWs are grown in the same run and on the same substrate at 540 °C. An EBL pattern consisting of square array of gold catalysts with different diameters (25, 50, 75, 100 nm) was used for VLS growth. The PL spectra of those NWs exhibit two distinct categories with ZB emission for <100> NWs and WZ emission for <111> nanowires. The PL lifetimes are measured at room temperature on 10-20 nanowires for each diameter and for each growth direction. The surface recombination velocity is then extracted by fitting the experimental data using the equation $1/\tau = 1/\tau_{bulk} + 4S/d$ [110], where τ is the measured PL decay time, τ_{bulk} is the carrier lifetime in the bulk of the NW without a contribution from the surface, S is the surface recombination velocity and d is the diameter of the NW. The results are presented in figure 6.9.

We found that the surface recombination velocity of the <111> NW is 2.2 x 10^3 cm/s and the NW bulk lifetime is 0.25 ns. The surface recombination velocity of the <100> InP NW is extracted to be 8.1 x 10^3 cm/s, and the NW bulk lifetime is 0.74 ns. The difference in the surface recombination velocity between <111> and <100> NWs is probably due to different crystal structures (predominantly WZ for <111> and pure ZB <100>) and side facets [223] (predominantly $\{1\bar{1}00\}$ oriented for <111> and {001} for <100>). The accuracy of surface recombination velocity extraction for <100> InP NWs is limited by the number available data points of our measurements (<100> NWs can be grown by using Au diameters larger than 50 nm only). Our obtained surface recombination velocities are similar to that of typical bulk InP but higher than that of the pure WZ intrinsic InP NWs (161 cm/s) [113] grown at much high temperature of 730 °C by selective area epitaxy method which have non-tapered morphology and smooth side facets.

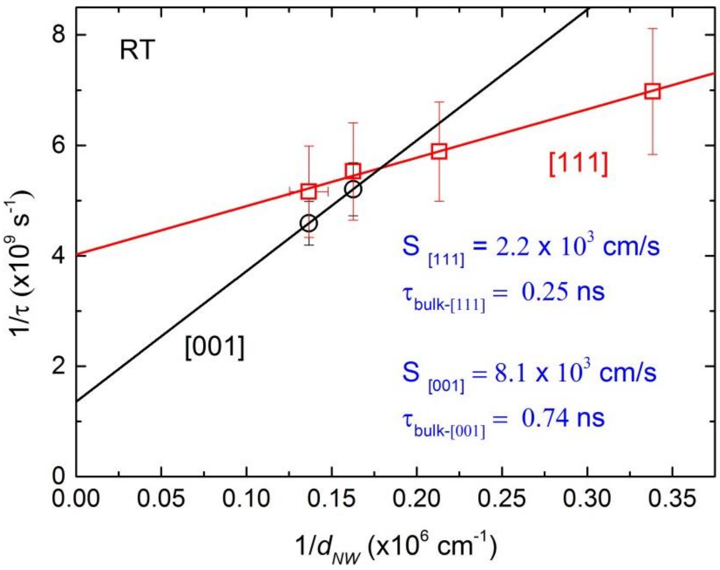

Figure 6.9. Estimation of room-temperature surface recombination velocities of intrinsic <111> and <100> InP NW by measuring the PL lifetimes as a function of the NW diameters. The surface recombination velocities are 2.2 x 10^3 cm/s and 8.1 x 10^3 cm/s for <111> and <100> InP NWs, respectively.

6.5 Conclusions

We have studied the optical properties of intrinsic, n-doped and p-doped <100> InP NWs grown on (100) InP substrates. The <100> InP NWs grown are free of planar stacking faults regardless the use of the *in-situ* dopants. Sulfur-doped <100> InP NWs show excellent photoluminescence efficiency. We were able to estimate the doping concentration of these NWs from the Burstein-Moss shift of the photoluminescence peak at room temperature. The Zn-doped <100> InP NWs show a lower photoluminescence efficiency compared to suphur-doped NWs and a complicated doping behavior. They exhibit an emission which originally appears at 1.224 eV for low excitation powers, and then broadens toward the zincblende InP bandgap when the excitation density is increased. This effect is explained by the coexistence of both interstitial and substitutional Zn dopants. The high amount of unwanted interstitial Zn, which compensates the Zn acceptors, can be significantly reduced by thermal annealing. Our study on n- and p-doped <100> InP NWs is important for the fabrication of stacking fault free nanowire solar cells and optoelectronic devices.

Bibliography

[1] S. Nadj-Perge, S. M. Frolov, E. P. A. M. Bakkers and L. P. Kouwenhoven, "Spin–orbit qubit in a semiconductor nanowire," *Nature,* vol. 468, p. 1084, 2010.

[2] Y. Hu, F. Kuemmeth, C. M. Lieber and C. M. Marcus, "Hole spin relaxation in Ge–Si core–shell nanowire qubits," vol. 7, p. 47, 2012.

[3] V. Mourik, K. Zuo, S. M. Frolov, S. R. Plissard, E. P. A. M. Bakkers, and L. P. Kouwenhoven, "Signatures of Majorana Fermions in Hybrid Superconductor-Semiconductor Nanowire Devices," vol. 336, pp. 1003-7, 2012.

[4] G. Bulgarini, M. E. Reimer, M. Hocevar, E. P. A. M. Bakkers, L. P. Kouwenhoven and V. Zwiller, "Avalanche amplification of a single exciton in a semiconductor nanowire," *Nature Photonics,* vol. 6, pp. 455-8, 2012.

[5] B. M. Kayes, H. A. Atwater and N. S. J. Lewis, "Comparison of the device physics principles of planar and radial p-n junction nanorod solar cells," *Appl. Phys.,* vol. 97, p. 114302, 2005.

[6] B. Tian, X. Zheng, T. J. Kempa, Y. Fang, N. Yu, G. Yu, J. Huang and C. M. Lieber, "Coaxial silicon nanowires as solar cells and nanoelectronic power sources," *Nature ,* vol. 449, p. 885–9, 2007.

[7] M. Heurlin, P. Wickert, S. Fält, M. T. Borgström, K. Deppert, L. Samuelson, M. H. Magnusson, "Axial InP nanowire tandem junction grown on a silicon substrate," *Nano Lett.,* vol. 11, p. 2028–2031, 2011.

[8] J. W. M. H. S. F. P. W. J. L. M. H. M. K. D. L. S. M. T. Borgström, "Nanowires with promise for photovoltaics," *IEEE J. Sel. Top. Quantum Electron.,* vol. 99, p. 1050, 2010.

[9] A. I. Hochbaum and P. Yang, "Semiconductor nanowires for energy conversion," *Chem. Rev.,* vol. 110, p. 527–546, 2010.

[10] A. M. Morales and C. M. Lieber, "A laser ablation method for the synthesis of crystalline semiconductor nanowires," *Science,* vol. 279, p. 208, 1998.

[11] A. Cavallini, L. Polenta, M. Rossi, T. Richter, M. Marso, R. Meijers, R. Calarco, and H. Luth, "Defect distribution along single GaN nanowhiskers," *Nano Lett.,* vol. 6, p. 1548, 2006.

[12] M. T. Björk , B. J. Ohlsson , T. Sass , A. I. Persson , C. Thelander , M. H. Magnusson , K. Deppert , L. R. Wallenberg and L. Samuelson, "One-dimensional steeplechase for electrons realized," *Nano Lett.,* vol. 2, p. 87, 2002.

[13] K. Haraguchi, T. Katsuyama, K. Hiruma and K. Ogawa, "GaAs p-n junction formed in quantum well wire crystals," *Appl. Phys. Lett.,* vol. 60, p. 745, 1992.

[14] R. S. Wagner and W. C. Ellis, "Vapor-liquid-solid mechanism of single crystal growth," *Appl. Phys. Lett.,* vol. 4, p. 89, 1964.

[15] J. B. Hannon, S. Kodambaka, F. M. Ross, and R. M. Tromp, "The influence of the surface migration of fold on the growth of silicon nanowires," *Nature,* vol. 440, p. 69, 2006.

[16] V. Schmidt, J. V. Wittemann, S. Senz, and U. Gosele, "Silicon nanowires: a review on aspects of their growth and their electrical properties," *Adv. Mater. ,* vol. 21, p. 2681–2702, 2009.

[17] G. Gu, M. Burghard, G. T. Kim, G. S. Dusberg, P. W. Chiu, V. Krstic, S. Roth, and W. Q. Han, "Growth and electrical transport of germanium nanowires," *J. Appl. Phys.,* vol. 90, p. 5747, 2001.

[18] X. F. Duan, Y. Huang, Y. Cui, J. F. Wang, and C. M. Lieber, "Indium phosphide nanowires as building blocks for nanoscale electronic and optoelectronic devices," *Nature,* vol. 409, p. 66, 2001.

[19] R. E. Algra, M.A. Verheijen, M.T. Borgström, L.F. Feiner, G. Immink, W.J.P. van Enckevort, E. Vlieg,and E.P.A.M. Bakkers, "Twinning superlattices in indium phosphide nanowires," *Nature,* vol. 456, pp. 369-372, 2008.

[20] K. Hiruma, M. Yazawa, T. Katsuyama, K. Ogawa, K. Haraguchi, M. Koguchi, and H. Kakibayashi, "Growth and optical properties of nanometer-scale GaAs and InAs whiskers," *J. Appl. Phys.,* vol. 77, p. 447, 1995.

[21] F. Glas, J. C. Harmand, and G. Patriarche, "Why does wurtzite form in nanowires of III-V zinc blende semiconductors?," *Phys. Rev. Lett.,* vol. 99, p. 146101 , 2007.

[22] X. Duan and C. M. Lieber, "General synthesis of compound semiconductor nanowires," *Adv. Mat.,* vol. 12, p. 298, 2000.

[23] S. Assali, I. Zardo, S. Plissard, D. Kriegner, M. A. Verheijen, G. Bauer, A. Meijerink, A. Belabbes, F. Bechstedt, J. E. M. Haverkort, and E. P. A. M. Bakkers, "Direct band gap wurtzite GaP nanowires," vol. 13, p. 1559–1563, 2013.

[24] X. Duan, and C. M. Lieber, "Laser assisted catalytic growth of single crystal GaN nanowires," *JACS,* vol. 122, p. 188, 2000.

[25] M. H. Huang, S. Mao, H. Feick, H. Yan, Y. Wu, H. Kind, E. Weber, R. Russo, P. D. Yang, "Room-temperature ultraviolet nanowire nanolasers," *Science,* vol. 1897, p. 292, 2001.

[26] K. L. van Vugt, S. Ruhle, and D. Vanmaekelbergh, "Phase-correlated nondirectional laser emission from the end facets of a ZnO nanowire," *Nano Lett.,* vol. 6, p. 2707, 2006.

[27] M. T. Borgström, J. Wallentin, J. Trägårdh, P. Ramvall, M. Ek, L. R. Wallenberg, L. Samuelson, and K. Deppert, "In situ etching for total control over axial and radial nanowire growth," vol. 3, p. 264–270, 2010.

[28] A. I. Persson, M. W. Larsson, S. Stenström, B. J. Ohlsson, L. Samuelson, and L. R. Wallenberg, "Solid-phase diffusion mechanism for GaAs nanowire growth," *Nat. Mat. ,* vol. 3, p. 677, 2004.

[29] T. J. Trentler, K. M. Hickman, S. C. Goel, A. M. Viano, P. C. Gibbons, W. E. Buhro, "Solution-liquid-solid growth of grystalline III-V semiconductors: an analogy to vapor-liquid-solid growth," *Science,* vol. 270 , p. 1791, 1995.

[30] J. W. Matthews and A. E. Blakeslee, "Defects in epitaxial multilayers: I. Misfit dislocations," *J. Cryst. Growth,* vol. 27, p. 118, 174.

[31] Y. Li, F. Qian, J. Xiang, and Charles M. Lieber, "Nanowire electronic and optoelectronic devices," *Materialtoday,* vol. 9, p. 18, 2006.

[32] F. Dimroth and S. Kurtz, "High-efficiency multijunction solar cells," *MRS Bulletin,* vol. 32, p. 230, 2007.

[33] W. Guter, J. Schöne, S. P. Philipps, M. Steiner, G. Siefer, A. Wekkeli, E. Welser, E. Oliva, A. W. Bett, and F. Dimroth, "Current-matched triple-junction solar cell reaching 41.1% conversion efficiency under concentrated sunlight," *Appl. Phys. Lett.,* vol. 94, p. 223504, 2009.

[34] P. Caroff, M. E. Messing, B. M. Borg, K. A. Dick, K. Deppert, and L. E. Wernersson, "InSb heterostructure nanowires: MOVPE growth underextreme lattice mismatch," *Nanotechnology,* vol. 20, p. 495606, 2009.

[35] T. Martensson, C. P. T. Svensson, B. A. Wacaser, M. W. Larsson, W. Seifert, K. Deppert, A. Gustafsson, L. R. Wallenberg, L. Samuelson, "Epitaxial III−V nanowires on silicon," *Nano Letter,* vol. 4, p. 1987, 2004.

[36] E. P. A. M. Bakkers, J. A. van Dam, S. D. Franceschi, L. P. Kouwenhoven, M. Kaiser, M. Verheijen, H. Wondergem and P. van der Sluis, "Epitaxial growth of InP nanowires on germanium," *Nat. Mater.,* vol. 3, pp. 769-773., 2004.

[37] E. P. A. M. Bakkers, M. T. Borgstrom and M. A. M. Verheijen, "Epitaxial growth of III-V nanowires on group IV substrates," *MRS Bull.,* vol. 32, p. 117, 2007.

[38] K. Tomioka, J. Motohisa, S. Hara and T. Fukui, "Control of InAs nanowire growth directions on Si," *Nano Lett.,* vol. 8, p. 3475–3480, 2008.

[39] K. Li, H. Sun, F. Ren, K. W. Ng, T. T. D. Tran, R. Chen and C. J. Chang-Hasnain, "Tailoring the optical characteristics of microsized InP nanoneedles directly grown on silicon," *Nano Lett.,* vol. 14, pp. 183-190, 2013.

[40] A. L. Roest, M. A. Verheijen, O. Wunnicke, S. Serafin, H. Wondergem and E. P. A. M. Bakkers, "Position-controlled epitaxial III–V nanowires on silicon," *Nanotechnology,* vol. 17, pp. 271-773, 2006.

[41] M. T. Bjork, B. J. Ohlsson, T. Sass, A. I. Persson, C. Thelander, M. H.Magnusson, K. Deppert, L. R. Wallenberg and L. Samuelson, "The morphology of axial and branched nanowire heterostructures," *Nano Lett.,* vol. 7, pp. 1817-1822, 2007.

[42] P. Caroff, M. E. Messing, B. M. Borg, K. A. Dick, K. Deppert and L. E. Wernersson, "InSb heterostructure nanowires: MOVPE growth under extreme lattice mismatch," *Nanotechnology,* vol. 20, p. 495606, 2009.

[43] M. Hocevar, G. Immink, M. Verheijen, N. Akopian, V. Zwiller, L. Kouwenhoven and E. Bakkers, "Growth and optical properties of axial hybrid III–V/silicon nanowires," *Nat. Commun.,* vol. 3, p. 1266, 2012.

[44] K. Hillerich, K. A. Dick, C. Y. Wen, M. C. Reuter , S. Kodambaka and F. M. Ross, "Strategies to control morphology in hybrid group III–V/group IV heterostructure nanowires," *Nano Lett.,* vol. 13, p. 903–908, 2013.

[45] http://us.sunpower.com/solar-panels-technology/e-series-solar-panels/.

[46] "http://www.sciencedaily.com/releases/2013/09/130923204214.htm".

[47] M. A. Green, K. Emery, Y. Hishikawa, W. Warta and E. D. Dunlop, "Solar cell efficiency tables (version 41)," *Progress in Photovoltaics,* vol. 21, pp. 1-11, 2013.

[48] J. V. Holm, H. I. Jørgensen, P. Krogstrup, J. Nygård, H. Liu and M. Aagesen, "Surface-passivated GaAsP single-nanowire solar cells exceeding 10% efficiency grown on silicon," *Nat. Commun.,* vol. 4, p. 1498, 2013.

[49] P. Krogstrup, H. I. Jørgensen, M. Heiss, O. Demichel, J. V. Holm, M. Aagesen, J. Nygard and

A. F. I. Morral, "Single-nanowire solar cells beyond the Shockley–Queisser limit," *Nature Photonics,* vol. 7, pp. 306-310, 2013.

[50] N. Anttu, A. Abrand, D. Asoli, M. Heurlin, I. Åberg, L. Samuelson and M. Borgström, "Absorption of light in InP nanowire arrays," *Nano Research,* 2014.

[51] J. Kupec and B. Witzigmann, "Dispersion, wave propagation and efficiency analysis of nanowire solar cells," *Optics Express,* vol. 17, p. 10399–10410, 2009.

[52] J. Kupec, R. L. Stoop and B. Witzigmann, "Light absorption and emission in," *Optics Express,* vol. 18, p. 27589, 2010.

[53] N. Anttu and H. Q. Xu, "Coupling of light into nanowire arrays and subsequent absorption," *J. Nanosci. Nanotechno,* vol. 10, pp. 7183-7187, 2010.

[54] S. K. Kim, K. D. Song, T. J. Kempa, R. W. Day, C. M. Lieber and H. G. Park, "Design of nanowire optical cavities as efficient photon absorbers," *ACS Nano,* p. DOI: 10.1021/nn5003776, 2014.

[55] S. Hu, C. Y. Chi, K. T. Fountaine, M. Yao, H. A. Atwater, P. D. Dapkus, N. S. Lewis and C. Zhou , "Optical, electrical, and solar energy-conversion properties of gallium arsenide nanowire-array photoanodes," *Energy Environ. Sci.,* vol. 6, pp. 1879-1890, 2013.

[56] C. Colombo, M. Heibeta, M. Gratzel, and A. Fontcuberta i Morral, "Gallium arsenide p-i-n radial structures for photovoltaic applications," *Appl. Phys. Lett.,* vol. 94, p. 173108, 2009.

[57] H. Goto, K. Nosaki, K. Tomioka, S. Hara, K. Hiruma, J. Motohisa, and T. Fukui , "Growth of core-shell inp nanowires for photovoltaic application by selective-areametal organic vapor phase epitaxy," *Appl. Phys. Express,* vol. 2, p. 035004, 2009.

[58] Z. Fan, H. Razavi, J. Do, A. Moriwaki, O. Ergen, Y.-L. Chueh, P. W. Leu, J. C. Ho, T. Takahashi, L. A. Reichertz, S. Neale, K. Yu, M. Wu, J. W. Ager and A. Javey, "Three-dimensional nanopillar-array photovoltaics on low-cost and flexible substrates," *Nat. Mater.,* vol. 8, p. 648–653, 2009.

[59] E. Garnett and P. D. Yang, "Light trapping in silicon nanowire solar cells," *Nano Lett.,* vol. 10, pp. 1082-1087, 2010.

[60] M. Yoshimura, E. Nakai, K. Tomioka and Ta. Fukui, "Indium Phosphide core–shell nanowire array solar cells with lattice-mismatched window layer," *Appl. Phys. Express,* vol. 6, p. 052301, 2013.

[61] J. Wallentin, N. Anttu,D. Asoli, M. Huffman, I. Åberg, M. H. Magnusson, G. Siefer, P. Fuss-Kailuweit, F. Dimroth, B. Witzigmann, H. Q. Xu, L. Samuelson, K. Deppert, M. T. Borgström, "InP nanowire array solar cell achieving 13.8% by exceeding the ray optics limit," *Science,* vol. 339, p. 1057, 2013.

[62] Y. Cui, J. Wang, S. R. Plissard, A. Cavalli, T. T. T. Vu, R. P. J. van Veldhoven, L. Gao, M. Trainor, M. A. Verheijen, J. E. M. Haverkort and E. P. A. M. Bakkers, "Efficiency enhancement of InP nanowire solar sells by surface cleaning," *Nano Lett.,* vol. 13, p. 4113–4117, 2013.

[63] G. Mariani, A. C. Scofield, C.H. Hung and D. L. Huffaker, "GaAs nanopillar-array solar cells employing in situ surface passivation," *Nat. Commun.,* vol. 4, p. 1497, 2013.

[64] D. Wang, A. Pierre, M. G. Kibria, K. Cui, X. Han, K. H. Bevan, H. Guo, S. Paradis, A. R. Hakima, and Z. Mi, "Wafer-level photocatalytic water splitting on GaN nanowire arrays grown by molecular beam epitaxy," *Nano Lett.,* vol. 11, p. 2353, 2011.

[65] L. Gao, Y. Cui, J. Wang, A. Cavalli, A. Standing, T. T. T. Vu, M. A. Verheijen, J. E. M. Haverkort, E. P. A. M. Bakkers, Peter HL Notten, "Photoelectrochemical hydrogen production on InP nanowire arrays with molybdenum sulfide electrocatalysts," *Nano Lett.,* vol. 14, p. 3715, 2014.

[66] S. W. Boettcher, J. M. Spurgeon, M. C. Putnam, E. L. Warren, D. B. Turner-Evans, M. D. Kelzenberg, J. R. Maiolo, H. A. Atwater, N. S. Lewis, "Energy-Conversion properties of vapor-liquid-solid–grown silicon wire-array photocathodes," *Science,* vol. 327, pp. 185-187 , 2010.

[67] S. Hu, C. Xiang, S. Haussener, A. D. Berger, and N. S. Lewis, "An analysis of the optimal band gaps of light absorbers in integrated tandem photoelectrochemical water-splitting systems," *Energy Environ. Sci.,* vol. 6, p. 2984, 2013.

[68] A. J. Standing, S. Assali, J. E.M. Haverkort JE, E. P. A. M. Bakkers, "High yield transfer of ordered nanowire arrays into transparent flexible polymer films," *Nanotechnology,* vol. 23, p. 495305, 2012.

[69] M. E. Reimer, G. Bulgarini, N. Akopian, M. Hocevar, M. B. Bavinck, M. A. Verheijen, E. P. A. M. Bakkers, L. P. Kouwenhoven and V. Zwiller , "Bright single-photon sources in bottom-up tailored nanowires," *Nature Commun. ,* vol. 3 , p. 737, 2012.

[70] World Energy Council, "World Energy Resources: 2013 Survey," London, 2013.

[71] W. Shockley and H.J. Queisser, "Detailed balance limit of efficiency of p-n junction solar cells," *J. Appl. Phys.,* vol. 32, p. 510, 1961.

[72] "World Record Solar Cell with 44.7% Efficiency," September 23, 2013.

[73] R. R. LaPierre, A. C. E. Chia, S. J. Gibson, C. M. Haapamaki, J. Boulanger, R. Yee, P. Kuyanov, J. Zhang, N. Tajik, N. Jewell and K. M. A. Rahman, "III–V nanowire photovoltaics: Review of design for high efficiency," *physica status solidi (RRL),* vol. 7, p. 815, 2013.

[74] F. Dimroth, S. Kurtz, "High-efficiency multijunction solar cells," *MRS Bulletin,* vol. 32, pp. 230-234, 2007.

[75] Y. Cui, J. Wang, S. R. Plissard, A. Cavalli, T. T. T. Vu, R. P. J. van Veldhoven, L. Gao, M. Trainor, M. A. Verheijen, J. E. M. Haverkort and E. P. A. M. Bakkers, "Efficiency enhancement of InP nanowire solar sells by surface cleaning," *Nano Lett.,* vol. 13, p. 4113–4117, 2013.

[76] J. Wallentin, N. Anttu,D. Asoli, M. Huffman, I. Åberg, M. H. Magnusson, G. Siefer, P. Fuss-Kailuweit, F. Dimroth, B. Witzigmann, H. Q. Xu, L. Samuelson, K. Deppert, M. T. Borgström,, "InP nanowire array solar cell achieving 13.8% by exceeding the ray optics limit," *Science,* vol. 339, p. 1057, 2013.

[77] S. J. Fonash, Solar cell device physics, 2nd edition, Academic Press, 2010.

[78] J. Nelson, The physics of solar cells, London: Imperial College Press, 2004.

[79] B. M Kayes, H. A. Atwater, N. S. Lewis, "Comparision of the device physics priciples of planar and radial p-n junction nanorod solar cells," *J. Appl. Phys.,* vol. 97, p. 114302, 2005.

[80] S. J. Fonash, Solar Cell Device Physics (Second Edition), Amsterdam: Academic Press, 2010.

[81] http://www.ioffe.rssi.ru/SVA/NSM/Semicond/InP/reference.html.

[82] Aspnes, D. E. and A. A. Studna, "Dielectric functions and optical parameters of Si, Ge, GaP, GaAs, GaSb, InP, InAs, and InSb from 1.5 to 6.0 eV," *Phys. Rev. B,* vol. 27, pp. 985-1009., 1983.

[83] O. L. Muskens, J. G. Rivas, R. E. Algra, E. P. A. M. Bakkers, D. Lagendijk, "Design of light scattering in nanowire materials for photovoltaics applications," *Nano Lett.,* vol. 8, pp. 2638-2642, 2008.

[84] L. Hu, G. Chen, "Analysis of optical absorption in silicon nanowire arrays for photovoltaic applications," *Nano Lett.,* vol. 7, p. 3249–3252, 2007.

[85] N. Anttu, "Geometrical optics, electrostatics, and nanophotonic resonances in absorbing nanowire arrays," *Opt. Lett.,* vol. 38, pp. 730-732, 2013.

[86] O. T. A. J. G. G. E. P. A. M. B. a. J. G. R. S. L. Diedenhofen, "Strong Geometrical Dependence of the Absorption of Light in Arrays of Semiconductor Nanowires," *ACS Nano,* vol. 5, p. 2316–2323, 2011.

[87] J. Zhu, Z. Yu, G. F. Burkhard, C. M. Hsu, S. T. Connor, Y. Xu, Q. Wang, M. McGehee, S. Fan, Y. Cui, "Optical absorption enhancement in amorphous silicon nanowire and nanocone arrays," *Nano lett.,* vol. 9, pp. 279-282, 2009.

[88] Z. Fan, R. Kapadia, P. W. Leu, X. Zhang, Y. L. Chueh, K. Takei, K. Yu, A. Jamshidi, A. A. Rathore, D. J. Ruebusch, M. Wu, and A. Javey, "Ordered arrays of dual-diameter nanopillars for maximized optical absorption," *Nano Lett.,* vol. 10, p. 3823–3827, 2010.

[89] N. Anttu, A. Abrand, D. Asoli, M. Heurlin, I. Åberg, L. Samuelson, and M. Borgström, "Absorption of light in InP nanowire arrays," *Nano Research,* vol. 7, p. 816–823, 2014.

[90] W. Shockley, W. T. Read, "Statistics of the Recombinations of Holes and Electrons," *Phys.Rev.,* vol. 87, p. 835–842, 1952.

[91] R. N. Hall, "Electron-hole recombination in Germanium," *Phys. Rev.,* vol. 87, p. 387, 1952.

[92] R. K. Ahrenkiel and M. S. Lundstrom, "Minority Carriers In III-V Semiconductors: Physics and Applications," in *Semiconductor and semimetals, Vol. 39*, 1993, pp. 39-149.

[93] A. Haug, "Auger recombination in InGaAsP," *Appl. Phys. Lett.,* vol. 42, p. 512, 1983.

[94] S. Ghosh, P. Bhattachary, E. Stoner, J. Singh, H. Jiang, S. Nuttinck, and J. Laskar, "Temperature-dependent measurement of Auger recombination in self-organized InGaAs/GaAs quantum dots," *Appl. Phys. Lett.,* vol. 79, p. 722, 2001.

[95] W. Guo, M. Zhang, P. Bhattacharya, and J. Heo, "Auger recombination in III-Nitride nanowires and Its effect on nanowire light-emitting diode characteristics," *Nano Lett.,* vol. 11, p. 1434–1438, 2011.

[96] Y. S. Yoo, T. M. Roh, J. H. Na, S. J. Son, and Y. H. Cho, "Simple analysis method for determining internal quantum efficiency and relative recombination ratios in light emitting diodes," *Appl. Phys. Lett.,* vol. 102, p. 211107, 2013.

[97] H. P. T Nguyen, M. Djavid, K. Cui, and Z. Mi, "Temperature-dependent nonradiative recombination processes in GaN-based nanowire white-light-emitting diodes on silicon," *Nanotechnology,* vol. 23, p. 194012, 2012.

[98] A. Dmitriev and A. Oruzheinikov , "The rate of radiative and recombination in the nitride semiconductor and alloys," *J. Appl. Phys.,* vol. 86, p. 3241, 1999.

[99] R. N. Hall, "Recombination processes in semiconductors, Vol. 106B," in *Proceedings of the IEE*, 1960.

[100] D.Z. Garbuzov, "Reradiation effects, lifetimes and probabilities of band-to-band transitions in direct A3B5 compounds of GaAs type," *J. Luminescence,* vol. 27, p. 109, 1982.

[101] B. Imangholi, M. P. Hasselbeck, M. Sheik-Bahae, R. I. Epstein, and S. Kurtz, "Effects of epitaxial lift-off on interface recombination and laser cooling in GaInP/GaAs heterostructures," *Appl. Phys. Lett. 86,* vol. 86, p. 081104 , 2005.

[102] F. Stern, "Calculated spectral dependence of gain in excited GaAs," *J. Appl. Phys.,* vol. 47, p. 5382, 1976.

[103] T. Matsusue and H.i Sakaki, "Radiative recombination coefficient of free carriers in GaAsAlGaAs quantum wells and its dependence on temperature," *Appl. Phys. Lett.,* vol. 50, p. 1429, 1987.

[104] A. Rose, Concepts in photoconductivity and allied problems, New York: Robert Krieger Publishing Company, 1978.

[105] P. B. Klein, R. Myers-Ward, K.-K. Lew, B. L. VanMil, C. R. Eddy, D. K. Gaskill, A. Shrivastava, and T. S. Sudarshan, "Recombination processes controlling the carrier lifetime in n–4H–SiC epilayers with low Z1/2 concentrations," *J. Appl. Phys.,* vol. 108, p. 033713 , 2010.

[106] F. Léonard, A. A. Talin, B. S. Swartzentruber, and S. T. Picraux, "Diameter-dependent electronic transport properties of Au-catalyst/Ge-nanowire Schottky diodes," *Phys. Rev. Lett.,* vol. 102, p. 106805, 2009.

[107] Y. Dan, K. Seo, K. Takei, J. H. Meza, A. Javey, and K. B. Crozier, "Dramatic reduction of surface recombination by in situ surface passivation of silicon nanowires," *Nano Lett.,* vol. 11, p. 2527–2532, 2011.

[108] J. P. McKelvey, and R. L. Longini, "Volume and surface recombination rates for injected carriers in Germanium," *J. Appl. Phys.,* vol. 25, p. 634 , 1954.

[109] M. A. Fickenscher, H. E. Jackson, L. M. Smith, J. M. Yarrison-Rice, J. H. Kang, S. Paiman, Q. Gao, H. H. Tan, and and C. Jagadish, "Direct imaging of the spatial diffusion of excitons in single semiconductor nanowires," *Appl. Phys. Lett.,* vol. 99, p. 263110, 2011.

[110] H. J. Joyce, J. Wong-Leung, C. K. Yong, C. J. Docherty, S. Paiman, Q. Gao, H. H. Tan, C. Jagadish, J. Lloyd-Hughes, L. M. Herz, and M. B. Johnston, "Ultralow Surface Recombination Velocity in InP Nanowires Probed by Terahertz Spectroscopy," *Nano Lett.,* vol. 12, p. 5325–5330, 2012.

[111] J. Wallentin, M. Ek, L. R. Wallenberg, L. Samuelson, and Magnus T. Borgström †, "Electron trapping in InP nanowire FETs with stacking faults," *Nano Lett.,* vol. 12, p. 151–155, 2012.

[112] H. J. Joyce, C. J. Docherty, Q. Gao, H. H. Tan, C. Jagadish, J. Lloyd-Hughes, L. M. Herz, and M. B. Johnston, "Electronic properties of GaAs, InAs and InP nanowires studied by terahertz spectroscopy," *Nanotechnology,* vol. 24, p. 214006, 2013.

[113] Q. Gao, D. Saxena, F. Wang, L. Fu, S. Mokkapati, Y. Guo, L. Li, J. Wong-Leung, P. Caroff, H. H. Tan, and C. Jagadish , "Selective-area epitaxy of pure wurtzite InP nanowires: high quantum efficiency and room-temperature lasing," *Nano Lett.,* vol. 14, p. 5206–5211, 2014.

[114] S. Bothra, S. Tyagi, S.K. Ghandhi, and J.M. Borrego, "Surface recombination velocity and lifetime in InP," *Solid-State Electronics,* vol. 34, pp. 47-50, 1991.

[115] A. Delamarre, L. Lombez, and J. F. Guillemoles, "Contactless mapping of saturation currents of solar cell by photoluminescence," *Appl. Phys. Lett.,* vol. 100, p. 131108, 2012.

[116] T. T. D. Tran, H. Sun, K. W. Ng, F. Ren, K. Li, F. Lu, E. Yablonovitch, and C. J. Chang-Hasnain, "High brightness InP micropillars grown on silicon with fermi level splitting larger than 1

eV," *Nano Lett.,* vol. 14, p. 3235, 2014.

[117] "http://www.picoquant.com/applications/category/life-science/time-resolved-fluorescence".

[118] X. Duan, Y. Huang, Y. Cui, J. Wang and C.M. Lieber, "InP nanowires as building blocks for nanoscale electronic and optoelectronic devices," *Nature,* vol. 409, pp. 66-69, 2001.

[119] G. Mariani, A. C. Scofield, C. H. Hung, and D. L. Huffaker, "GaAs nanopillar-array solar cells employing in situ surface passivation," *Nat. Com.,* vol. 4, pp. 1-7, 2013.

[120] P. Krogstrup, H. I. Jørgensen, M. Heiss, O. Demichel, J. V. Holm, M. Aagesen, J. Nygard, and A F. i Morral, "Single-nanowire solar cells beyond the Shockley–Queisser limit," *Nature Photonics,* vol. 7, p. 306–310, 2013.

[121] B. Hua, J. Motohisa , Y. Kobayashi , S. Hara, and Takashi Fukui, "Single GaAs/GaAsP coaxial core–shell nanowire lasers," *Nano Lett.,* vol. 9 , p. 112–116, 2009.

[122] Q. Li, J. B. Wright, W. W. Chow, T. S. Luk, I. Brener, L. F. Lester, and G. T. Wang, "Single-mode GaN nanowire lasers," *Opt. Expr.,* vol. 20, pp. 17873-17879, 2012.

[123] A. C. Scofield, S. H. Kim, J. N. Shapiro, A. Lin, B. Liang, A. Scherer, and D. L. Huffaker, "Bottom-up photonic crystal lasers," *Nano Lett.,* vol. 2011, p. 5387–5390, 2011.

[124] K. Tomioka, J. Motohisa, S. Hara, K. Hiruma,and T. Fukui, "GaAs/AlGaAs core multishell nanowire-based light-emitting diodes on Si," *Nano Lett.,* vol. 10, p. 1639–1644, 2010.

[125] L. C. Chuang, F. G. Sedgwick, R. Chen, W. S. Ko, M. Moewe, K. Wei Ng, T. T. D. Tran, and C. Chang-Hasnain, "GaAs-based nanoneedle light emitting diode and avalanche photodiode monolithically integrated on a silicon substrate,," *Nano Lett.,* vol. 11, p. 385, 2011.

[126] E. M. Gallo, G. Chen, M. Currie, T. McGuckin, P. Prete, N. Lovergine, B. Nabet, and J. E. Spanier, "Picosecond response times in GaAs/AlGaAs core/shell nanowire-based photodetectors," *Appl. Phys. Lett. ,* vol. 98, p. 241113, 2011.

[127] S. P. Bremner, M. Y. Levy, andC. B. Honsberg, "Analysis of tandem solar cell efficiencies under AM1.5G spectrum using a rapid flux calculation method," *Prog. Photovoltaics,* vol. 16, p. 225, 2008.

[128] P. Caroff, J. Bollinsson, J. Johansson, "Crystal phases in III-V nanowires: from random toward engineered polytypism," *IEEE J. of Sel. Top. Quant. Elec.,* vol. 17, pp. 829-846, 2011.

[129] M. Murayama and T. Nakayama, "Chemical trend of band offsets at wurtzite/zinc-blende heterocrystalline semiconductor interfaces," *Phys. Rev. B,* vol. 49, p. 4710, 1994.

[130] S. Perera, K. Pemasiri, M. A. Fickenscher, H. E. Jackson, L. M. Smith,J. Yarrison-Rice, S. Paiman, Q. Gao, H. H. Tan,and C. Jagadish, "Probing valence band structure in wurtzite InP nanowires using excitation spectroscopy," *Appl. Phys. Lett.,* vol. 97, p. 023106 , 2010.

[131] N. Akopian, G. Patriarche, L. Liu, J.-C. Harmand and V. Zwiller, "Crystal phase quantum dots," *Nano Lett.,* vol. 10, p. 1198–1201, 2010.

[132] K. Li, H. Sun, F. Ren, K. W. Ng, T. T. D. Tran, R. Chen, and C. J. Chang-Hasnain, "Tailoring the optical characteristics of microsized InP nanoneedles directly grown on silicon," *Nano Lett.,* vol. 14, p. 183–190, 2014.

[133] M. D. Stiles and D. R. Hamann, "Ballistic electron transmission through interfaces," *Phys. Rev. B,* vol. 38, pp. 2021-2037, 1988.

[134] M. D. Stiles and D. R. Hamann, "Electron transmission through silicon stacking faults," *Phys.*

Rev. B, vol. 41, pp. 5280-5282, 1990.

[135] M. D. Schroer and J. R. Petta, "Correlating the nanostructure and electronic properties of InAs nanowires," *Nano Lett.,* vol. 10, pp. 1618-1622, 2010.

[136] F. J. Lopez, E. R. Hemesath, and L. J. Lauhon, "Ordered stacking fault arrays in silicon nanowires," *Nano Lett.,* vol. 9, p. 2774–2779, 2009.

[137] J. Wang, S. Plissard, M. Hocevar, T. T. T. Vu, T. Zehender, G. G. W. Immink, M. A. Verheijen, J. Haverkort, E. P. A. M. Bakkers, "Position-controlled [100] InP nanowire arrays," *Appl. Phys. Lett.,* vol. 100, p. 053107, 2012.

[138] U. Krishnamachari, M. Borgstrom, B. J. Ohlsson, N. Panev, L. Samuelson, W. Seifert, M. W. Larsson, and L. R. Wallenberg, "Defect-free InP nanowires grown in [001] direction on InP (001)," *Appl. Phys. Lett. ,* vol. 85, p. 2077, 2004.

[139] J. Wang, S. R. Plissard, M. A. Verheijen, L. F. Feiner, A. Cavalli and E. P. A. M. Bakkers, "Reversible Switching of InP Nanowire Growth Direction by Catalyst Engineering," *Nano Lett.,* vol. 13, pp. 3802-3806, 2013.

[140] I. Regolina, D. Sudfeldb, S. Lüttjohann, V. Khorenko, W. Prost, J. Kästner, G. Dumpich, C. Meier, A. Lorke, F.-J. Tegude, "Growth and characterisation of GaAs/InGaAs/GaAs nanowhiskers on (1 1 1) GaAs," *Journal of Crystal Growth,* vol. 298, p. 607–611, 2007.

[141] L.D. Zhu, K.T. Chan, J.M. Ballantyne, "MOCVD growth and characterization of high quality InP," *Journal of Crystal Growth,* vol. 73, pp. 83-95, 1985.

[142] A. Mishra, L. V. Titova, T. B. Hoang, H. E. Jackson, L. M. Smith, J. M. Yarrison-Rice, Y. Kim, H. J. Joyce, Q. Gao, H. H. Tan, and C. Jagadish, "Polarization and temperature dependence of photoluminescence from zincblende and wurtzite InP nanowires," *Appl. Phys. Lett.,* vol. 91, p. 263104, 2007.

[143] R.E. Algra, M.A. Verheijen, M.T. Borgström, L.F. Feiner, G. Immink, W.J.P. van Enckevort, E. Vlieg,and E.P.A.M. Bakkers, "Twinning superlattices in indium phosphide nanowires," *Nature,* vol. 456, pp. 369-372 , 2008.

[144] T. Xu, K. A. Dick, S. Plissard, T. H. Nguyen, Y. Makoudi, M. Berthe, J.-P. Nys, X. Wallart, B. Grandidier, and P. Caroff, "Faceting, composition and crystal phase evolution in III–V antimonide nanowire heterostructures revealed by combining microscopy techniques," *Nanotechnology,* vol. 23, p. 095702, 2012.

[145] G. L. Tuin, M. T. Borgström, J. Trägårdh, M. Ek, L. R. Wallenberg, L. Samuelson, M. E. Pistol, "Valence band splitting in wurtzite InP nanowires observed by photoluminescence and photoluminescence excitation spectroscopy," *Nano Research,* vol. 4, pp. 159-163, 2011.

[146] S. A. Chevtchenko, M. A. Reshchikov, Q. Fan, X. Ni, Y. T. Moon, A. A. Baski, and H. Morkoç, "Study of SiNx and SiO2 passivation of GaN surfaces," *J. Appl. Phys. ,* vol. 101, p. 113709, 2007.

[147] M. Mattila, T. Hakkarainen, M. Mulot, and H. Lipsanen, "Crystal-structure-dependent photoluminescence from InP nanowires," *Nanotechnology,* vol. 17, p. 1580–1583, 2006.

[148] Z. M. Fang, K. Y. Ma, R. M. Cohen, and G. B. Stringfellow , "Effect of growth temperature on photoluminescence of InAs grown by organometallic vapor phase epitaxy," *Appl. Phys. Lett. ,* vol. 59, p. 1446, 1991.

[149] K. L. Fry, C. P. Kuo, C. A. Larsen, R. M. Cohen, G. B. Stringfellow, and A. Melas, "OMVPE

growth of InP and Ga0.47In0.53As using ethyldimethylindium," *J. Elec. Mat.,* vol. 15, pp. 91-96, 1986.

[150] J. M. Bao, D. C. Bell, F. Capasso, J. B. Wagner, T. Martensson, J. Tragardh, and L. Samuelson, "Optical properties of rotationally twinned InP nanowire heterostructures," *Nano Lett.,* vol. 8, pp. 836-841, 2008.

[151] H. J. Joyce, J. Wong-Leung , Q. Gao , H. H. Tan, and C. Jagadish, "Phase perfection in zinc blende and wurtzite III–V nanowires using basic growth parameters," *Nano Lett.,* vol. 10, p. 908–915, 2010.

[152] H. Shtrikman, R. Popovitz-Biro, A. Kretinin, L. Houben, M. Heiblum, M. Bukała, M. Galicka, R. Buczko, and P. Kacman, "Method for Suppression of Stacking Faults in Wurtzite III−V Nanowires," *Nano Lett.,* vol. 9, p. 1506–1510, 2009.

[153] M. Heiss, S. Conesa-Boj, J. Ren, H. H. Tseng, A. Gali, A. Rudolph, E. Uccelli, F. Peiro, J. R. Morante, D. Schuh, E. Reiger, E. Kaxiras, J. Arbiol, and A. M. i Fontcuberta, "Direct correlation of crystal structure and optical properties in wurtzite/zinc-blende GaAs nanowire heterostructures," *Phys. Rev. B,* vol. 83 , p. 045303, 2011.

[154] P. Caroff, K. A. Dick, J. Johansson, M. E. Messing, K. Deppert, and L. Samuelson, "Controlled polytypic and twin-plane superlattices in III–V nanowires," *Nat. Nanotech.,* vol. 4, pp. 50-55, 2009.

[155] K. Naji, H. Dumont, G. Saint-Girons, J. Penuelas, G. Patriarche, M. Hocevar, V. Zwiller, and M. Gendry, "Growth of vertical and defect free InP nanowires on SrTiO3(001) substrate and comparison with growth on silicon," *J. Cryst. Growth,* vol. 343, pp. 101-104, 2012.

[156] E. G. Gadret, G. O. Dias, L. C. O. Dacal, M. M. de Lima, Jr., C. V. R. S. Ruffo, F. Iikawa, M. J. S. P. Brasil, T. Chiaramonte, M. A. Cotta, L. H. G. Tizei, D. Ugarte, and A. Cantarero, "Valence-band splitting energies in wurtzite InP nanowires: Photoluminescence spectroscopy and ab initio calculations," *Phys. Rev. B,* vol. 87, p. 125327 , 2010.

[157] N. Chauvin, M. H. Hadj Alouane, R. Anufriev, H. Khmissi, K. Naji, G. Patriarche, C. Bru-Chevallie, and M. Gendry, "Growth temperature dependence of exciton lifetime in wurtzite InP nanowires grown on silicon substrates," *Appl. Phys. Lett.,* vol. 100, p. 011906, 2012.

[158] M. H. H. Alouane, N. Chauvin, H. Khmissi, K. Naji, B. Ilahi, H. Maaref, G. Patriarche, M. Gendry, and C. Bru-Chevallie, "Excitonic properties of wurtzite InP nanowires grown on silicon substrate," *Nanotechnology,* vol. 24, p. 035704, 2013.

[159] P. J. Dean and M. S. Skolnick, "Donor discrimination and bound exciton spectra in InP," *J. Appl. Phys.,* vol. 54, p. 346, 1983.

[160] Y. Rosenwaks, I. Tsimberova, H. Gero, and M. Molotskii, "Minority-carrier recombination in p –InP single crystals," *Phys. Rev. B,* vol. 68, p. 115210, 2003.

[161] L. M. Smith, H. E. Jackson, J. M .Yarrison-Rice, and C. Jagadish, "Insights into single semiconductor nanowire heterostructures using time-resolved photoluminescence," *Semicond. Sci. Technol.,* vol. 25, p. 024010, 2010.

[162] L. Zhang, J. W. Luo, A. Zunger, N. Akopian, V. Zwiller, and J. C. Harmand, "Wide InP nanowires with wurtzite/zincblende superlattice segments are type-II whereas narrower nanowires become type-I: an atomistic pseudopotential calculation," *Nano Lett.,* vol. 10, p. 4055–4060, 2010.

[163] A. Liu and Y. Rosenwaks, "Excess carriers lifetime in InP single crystals: Radiative versus nonradiative recombination," *J. Appl. Phys.,* vol. 86, p. 430, 1999.

[164] C. Jordan, J. F. Donegan, J. Hegarty, B. J. Roycroft, S. Taniguchi, T. Hino, E. Kato, N. Noguchi, and A. Ishibashi, "Carrier-density dependence of the photoluminescence lifetimes in ZnCdSe/ZnSSe quantum wells at room temperature," *Appl. Phys. Lett.,* vol. 74, p. 3359.

[165] S. Perera, M. A. Fickenscher, H. E. Jackson, L. M. Smith, J. M. Yarrison-Rice, H. J. Joyce, Q. Gao, H. H. Tan, C. Jagadish, X. Zhang, and J. Zou, "Nearly intrinsic exciton lifetimes in single twin-free GaAs/AlGaAs core-shell nanowire heterostructures," *Appl. Phys. Lett.,* vol. 93, p. 053110, 2008.

[166] R. Anufriev, N. Chauvin, H. Khmissi, K. Naji, M. Gendry, and C. Bru-Chevallier1, "Impact of substrate-induced strain and surface effects on the optical properties of InP nanowires," *Appl. Phys. Lett.,* vol. 101, p. 072101.

[167] I. Vurgaftman, J. R. Meyer, and L. R. Ram-Mohan, "Band parameters for III–V compound semiconductors and their alloys," *J. Appl. Phys.,* vol. 89, p. 5815, 2001.

[168] A. Belabbes, C. Panse, J. Furthmuller, and F. Bechstedt, "Electronics bands of III-V semiconductor polypypes and their allignment," *Phys. Rev. B,* vol. 86, p. 075208, 2012.

[169] K. Hiruma, M. Yazawa, T. Katsuyama, K. Ogawa, K. Haraguchi, M. Koguchi, and H. Kakibayashi, "Growth and optical properties of nanometerscale GaAs and InAs whiskers," vol. 77, p. 447, 1995.

[170] T. T. T. Vu, T. Zehender, M. A. Verheijen, S. R. Plissard, G. W. G. Immink, J. E. M. Haverkort, E. P. A. M. Bakkers, "High optical quality single crystal phase wurtzite and zincblende InP nanowires," *Nanotechnology,* vol. 24, p. 115705, 2013.

[171] K. A. Dick, C. Thelander, L. Samuelson, and P. Caroff, "Crystal phase engineering in single InAs nanowires," *Nano Lett.,* vol. 10, p. 3494, 2010.

[172] P. Corfdir, B. V. Hattem, E. Uccelli, S. Conesa-Boj, P. Lefebvre, A. F. i Morral, and R. T. Phillips, "Three-dimentional magneto-photoluminescence as a probe of the electonic propeties of crystal-phase quantum disks in GaAs nanowires," *Nano Lett.,* vol. 13, pp. 5303-5310, 2013.

[173] A. Belabbes, J. Furthmuller, and F. Bechstedt, "Relation between spontaneous polarization and crystal field from first principles," *Phys. Rev. B,* vol. 87, p. 035305, 2013.

[174] J. Lahnemann, O. Brandt, U. Jahn, C. Pfuller, C. Roder, P. Dogan, F. Grosse, A. Belabbes, F. Bechstedt, A. Trampert, and L. Geelhaar,, "Direct experimental determination of the spontaneous polarization of GaN," *Phys. Rev. B,* vol. 86, p. 081302(R), 2012.

[175] G. Jacopin, L. Rigutti, L. Largeau, F. Fortuna, F. Furtmayr, F. H. Julien, M. Eickhoff, and M. Tchernycheva, "Optical properties of wurtzite/zinc-blende heterostructures in GaN nanowires," *Appl. Phys. Lett.,* vol. 110, p. 064313, 2011.

[176] J. Bolinsson, P. Caroff, B. Mandl, and K. A. Dick, "Wurtzite-zincblende superlattices in InAs nanowires using a supply interruption method," *Nanotechnology,* vol. 22, p. 265606, 2011.

[177] S.M. Sze, Physics of semiconductor devices, 2nd edition, John Wiley & Sons, 1981.

[178] A. De and Craig E. Pryor, "Predicted band structures of III-V semiconductors in the wurtzite phase," *Phys. Rev. B,* vol. 81, p. 155210, 2010.

[179] F. Bechstedt and A. Belabbes, "Structure, energetics and electronic states of III-V compound polytypes," *J. Phys.: Cond. Matt.,* vol. 25, p. 273201, 2013.

[180] S. Assali, J. E. M. Haverkort, M. de Moor, I. Zardo, E. P. A. M. Bakkers, "Band structure of wurtzite GaP," *Submitted,* 2014.

[181] D. G. Thomas, J.J. Hopfeld, and C.J. Frosch, "Isoelectronic traps due to nitrogen in gallium phosphide," *Phys. Rev. Lett.,* vol. 15, p. 857, 1965.

[182] J. L. Merz, R. A. Faulkner, and P. J. Dean, "Excitonic molecule bound to the isoelectronic nitrogen trap in GaP," *Phys. Rev.,* vol. 188, p. 1228, 1969.

[183] R. D. King-Smith and David Vanderbilt, "Theory of polarization of crystalline solids," *Phys. Rev. B,* vol. 47, p. 1651, 1992.

[184] F. Bernardini, V. Fiorentini and D. Vanderbilt, "Spontaneous polarization and piezoelectric constants of III-V nitrides," *Phys. Rev. B,* vol. 56, p. R10 024, 1997.

[185] R. Resta, "Macroscopic polarization in crystalline dielectrics: the geometric phase approach," *Rev. Mod. Phys.,* vol. 66, p. 899, 1994.

[186] F. Bechstedt, Ulrike Grossner, and J. Furthmuller, "Dynamics and polarization of group-III nitride lattices: A first-principles study," *Phys. Rev. B,* vol. 62, pp. 8003-8011, 2000.

[187] O. Ambacher, J. Smart, J. R. Shealy, N. G. Weimann, K. Chu, M. Murphy, W. J. Schaff, L. F. Eastman, R. Dimitrov, L. Wittmer, M. Stutzmann, W. Rieger, and J. Hilsenbeck, "Two-dimensional electron gases induced by spontaneous and piezoelectric polarization charges in N-and Ga-face AlGaN/GaN heterostructures," *J. Appl. Phys.,* vol. 85, pp. 3222-3233, 1999.

[188] S. H. Park and S. L. Chuang, "Spontaneous polarization effects in wurtzite GaN/AlGaN quantum wells and comparison with experiment," *Appl. Phys. Lett.,* vol. 76, p. 1981, 2000.

[189] O. Ambacher, J. Majewski, C.Miskys, A.Link, M.Hermann, M.Eickhoff, M.Stutzmann, F.Bernardini, V.Fiorentini, V. Tilak, B. Schaff,and L.F.Eastman3, "Pyroelectric properties of Al(In)GaN/GaN hetero- and quantum well structures," *J. Phys.: Condens. Matter,* vol. 14, p. 3399, 2002.

[190] B. Bauer, J. Hubmann, M. Lohr, E. Reiger, D. Bougeard, and J. Zweck, "Direct detection of spontaneous polarization in wurtzite GaAs nanowires," *Appl. Phys. Lett.,* vol. 104, p. 211902, 2014.

[191] C. Y. Yeh, Z. W. Lu, S. Froyen, and A. Zunger, "Zinc-blende–wurtzite polytypism in semiconductors," *Phys. Rev. B,* vol. 46, p. 10086, 1992.

[192] V. Fiorentini, F. Bernardini, F. D. Salla, a. D. Carlo, and P. Lugli, "Effects of macroscopic polarization in III-V nitride multiple quantum wells," *Phys. Rev. B,* vol. 60, pp. 8849-8858, 1999.

[193] D. Kriegner, S. Assali, A. Belabbes, T. Etzelstorfer, V. Holý, T. Schülli, F. Bechstedt, E. P. A. M. Bakkers, G. Bauer, and J. Stangl, "Unit cell structure of the wurtzite phase of GaP nanowires: X-ray diffraction studies and density functional theory calculations," *Phys. Rev. B,* vol. 88, p. 115315 , 2013.

[194] J. Lahnemann, U. Jahn, O. Brandt, T. Flissikowski, P. Dogan, and H. T. Grahn, "Luminescence associated with stacking faults in GaN," *J. Phys. D: Appl. Phys. ,* vol. 47, p. 423001 , 2014.

[195] J. D. Cuthbert and D. G. Thomas, "Fluorescent decay times of excitons bound to isoelectronic traps in GaP and ZnTe," *Phys. Rev.,* vol. 154, pp. 763-771, 1967.

[196] M. Ikezawa, Y. Sakuma, and Y. Masumoto, "Single photon emission from individual nitrogen pairs in GaP," *Jap. J. Appl. Phys.,* vol. 46, p. L871–L873, 2007.

[197] Y. Sakumaa, M. Ikezawab, M. Watanabeb, and Y. Masumoto, "Isoelectronic nitrogen δ-doping in GaP and single-photon emission from individual nitrogen pairs," *J. Cryst. Growth,* vol. 310, pp. 4790-4794, 2008.

[198] C. Wilhelm, A. Larrue, X. Dai, D. Migas, and C. Soci, "Anisotropic photonic properties of III-V nanowires in the zinc-blende and wurtzite phase," *Nanoscale,* vol. 4, p. 1446, 2012.

[199] W. Braun, Vl. M. Kaganer, A. Trampert, H. P. Schönherr, Q. Gong, R. Nötzel, L. Däweritz, and K. H. Ploog, "Diffusion and incorporation: shape evolution during overgrowth on structured substrates," *J. Cryst. Growth,* vol. 227, pp. 51-55, 2011.

[200] S. A. Fortuna and X. Li, "Metal-catalyzed semiconductor nanowires: a review on the control of growth directions," *Semicond. Sci. Technol.,* vol. 25, p. 024005, 2010.

[201] A. A. Stekolnikov, J. Furthmüller, and F. Bechstedt, "Absolute surface energies of group-IV semiconductors: Dependence on orientation and reconstruction," *Phys. Rev. B,* vol. 65, p. 115318, 2002.

[202] N. Wang, Y. Cai, and R. Q. Zhang, "Growth of nanowires," *Materials Science and Engineering: R: Reports,* vol. 60, pp. 1-51, 2008.

[203] R. E. Algra, M. Hocevar, M. A. Verheijen, I. Zardo, G. G. W. Immink, W. J. P. van Enckevort, G. Abstreiter, L. P. Kouwenhoven, E. Vlieg, and E. P. A. M. Bakkers, "Crystal structure transfer in core/shell nanowires," *Nano Lett.,* vol. 11, p. 1690–1694, 2011.

[204] M. Razeghi, Ph. Maurel, M. Defour, F. Omnes, G. Neu and A. Kozacki, "Very high purity InP epilayer grown by metalorganic chemical vapor deposition," *Appl. Phys. Lett.,* vol. 52, p. 117, 1988.

[205] J. Wang, S. R. Plissard, M. A. Verheijen, L. F. Feiner, A. Cavalli, and E. P. A. M. Bakkers, "Reversible switching of InP nanowire growth direction by catalyst engineering," *Nano Lett.,* vol. 13, p. 3802–3806, 2013.

[206] J. H. Kang, Y. Cohen, Y. Ronen, M. Heiblum, R. Buczko, P. Kacman, R. Popovitz-Biro, and H. Shtrikman, "Crystal structure and transport in merged InAs nanowires MBE grown on (001) InAs," *Nano Lett.,* vol. 13, pp. 5190-5196, 2013.

[207] S. Murakami, H. Funayama, K. Shimomura, and T. Waho, "Au-Assisted Growth of InAs Nanowires on GaAs(111)B, GaAs(100), InP(111)B, InP(100) by MOVPE," *Phys. Status Solidi C ,* vol. 10, p. 761–764., 2013.

[208] J. Wang, Controling nanowire growth direction, PhD Thesis, ISBN: 978-90-8891-785-1, Eindhoven University of Technology, 2013.

[209] R. Iyer, R. R. Chang, and D. l. Liie, "Sulfur as a surface passivation for inP," *Appl. Phys. Lett.,* vol. 134, p. 134, 1988.

[210] C. Liu, L. Dai, L. P. You, W. J. Xu, and G G Qin, "Blueshift of electroluminescence from single n-InP nanowire/p-Si heterojunctions due to the Burstein–Moss effect," *Nanotechnology,* vol. 19, p. 465203, 2008.

[211] Boer, K. W., "Survey of Semiconductor Physics," New York: Van Nostrand Reinhold, 1990, p. 240.

[212] I. Tsimberova, Y. Rosenwaks, and M. Molotskii, "Minority carriers recombination in n-InP single crystals," *J. Appl. Phys.,* vol. 93, p. 9797, 2003.

[213] N. Tajik, C. M. Haapamaki, and R. R. LaPierre, "Photoluminescence model of sulfur passivated

p-InP nanowires," *Nanotechnology,* vol. 23, p. 315703, 2012.

[214] J. K. Hsu, C. Juang, B. J. Lee, and G. C. Chi, "Photoluminescence studies of interstitial Zn in InP due to rapid thermal annealing," *J. Vac. Sci. Technol. B,* vol. 12, p. 1416, 1994.

[215] A. Borghesi, G. Guizzetti, M. Patrini, A. Caligiore, R. C. Chen, and S. Pellegrino, "Infrared study and characterization of Zn diffused InP," *J. Appl. Phys.,* vol. 74, p. 2445 , 1993.

[216] C. Blaauw and L. Hobbs, "Donor-acceptor pair formation in InP doped simultaneously with Si and Zn during metalorganic chemical vapor deposition," *Appl. Phys. Lett. ,* vol. 59, p. 674, 1991.

[217] Y. B. Moon, S. K. Si, E. J. Yoon, and S. J. Kim, "Low temperature photoluminescence characteristics of Zn-doped InP grown by metalorganic chemical vapor deposition," *J. Appl. Phys.,* vol. 83, pp. 2261-2265, 1998.

[218] M. Grundmann, The physics of semiconductors, Berlin: Springer, 2006.

[219] K. H. Yoon, Y. H. Lee, D. H. Yeo, and S. J. Kim, "The characteristics of Zn-doped InP using spin-on dopant as a diffusion source," *J. of Elec. Mat.,* vol. 31, pp. 244-247, 2002.

[220] N. H. Ky, L. Pavesi, D. Araujo, J. D. Ganiere, and F. K. Reinhart, "A model for the Zn diffusion in GaAs by a photoluminescence study," *J. Appl. Phys.,* vol. 69, p. 7585 , 1991.

[221] A. Casadei, P. Krogstrup, M. Heiss, J. A. Rohr, C. Colombo, T. Ruelle, S. Upadhyay, C. B. Srensen, J. Nygard, and A. F. i Morral, "Doping incorporation paths in catalyst-free Be-doped GaAs nanowires," *Appl. Phys. Lett.,* vol. 102, p. 013117, 2013.

[222] E. A. Montie and G. J. van Gurp, "Photoluminescence of Zn-diffused and annealed InP," *J. Appl. Phys.,* vol. 66, pp. 5549-5553, 1989.

[223] C. A. Hoffman, H. J. Gerritsen and A. V. Nurmikko , "Study of surface recombination in GaAs and InP by picosecond optical techniques," *J. Appl. Phys.,* vol. 51, p. 1603, 1980.

[224] D. G. Thomas, J. J. Hopfield and W. M. Augustyniak, "Kinetics of Radiative Recombination at Randomly Distributed Donors and Acceptors," *Phys. Rev.,* vol. 140, p. 202, 1965.

[225] E. Spenke, "Electronic Semicondutor," New York, McGraw-Hill, 1958, p. 45.

List of Abbreviations

CPQD	Crystal phase quantum dot/disk
CW	Continuous wave
HRTEM	High-resolution transmission electron microscopy
IQE	Internal quantum efficiency
MBE	Molecular beam epitaxy
MOVPE	Metalorganic vapor phase epitaxy
NW	Nanowire
PDMS	Polydimethylsiloxane
PL	Photoluminescence
QCSE	Quantum-confined Stark effect
SAPD	Single photon avalanche diode
SEM	Scanning electron microscopy
SP	Spontaneous polarization
TCSPC	Time-correlated single photon counting
TEM	Transmission electron microscopy
TMG	Trimethylgallium
TMIn	Trimethylindium
TP	Twin plane
TRPL	Time-resolved photoluminescence
VLS	Vapor-liquid-solid
VS	Vapor-solid
WZ	Wurtzite
ZB	Zincblende
ZB-TSL	Zincblende twinning superlattice

Summary

Nanowire photoluminescence for photovoltaics

Nanowires have emerged as a promising class of materials for high efficiency, low cost solar cells. Thanks to the elastic strain relaxation, nanowire enables the fabrication of almost unlimited combinations of semiconductor materials, enabling the fabrication of multi-junction cell with bandgaps matching the entire solar spectrum. The light concentration effects of the nanowire geometry allow high optical absorption while using much less material as compared to their thin film counterparts. In order to obtain high efficiency nanowire solar cells, many requirements must be simultaneously met, including a perfect crystal phase, a low surface recombination velocity, the absence of unintentional sidewall growth and very low residual impurities levels.

This thesis focuses on micro-photoluminescence (PL) and time-resolved PL techniques to study the structural and optical properties of nanowires intended for solar cell applications. The semiconductor nanowires used in our studies are grown by the vapor-liquid-solid mechanism using metalorganic vapour phase epitaxy. By employing high-temperature growth combined with HCl in-situ etching, high material quality single crystal phase wurtzite (WZ) and zincblende (ZB) <111> InP nanowire have been obtained for different diameter of the catalyst seeds. These nanowires show bulk-like PL with bright emissions and long PL lifetime. For ZB <111> InP nanowires, a small amount of overgrowth on the nanowire sidewall is attributed due to their zigzag morphology. This sidewall growth (by vapour-liquid mechanism) often results in a lower material quality and a higher amount of incorporated carbon impurities. The PL spectrum from those ZB nanowires shows pronounced acceptor-related emission which is not observed in WZ nanowires with smooth side facets. By piranha post-growth etching, the overgrown sidewall can be completely removed. This can be clearly observed by comparing the nanowire PL before and after post-growth etching as presented in chapters 3 and 4.

This sidewall cleaning technique was also applied to axial p-n junction <111> InP solar cells. When we grow Zn-doped (p-type) <111> InP nanowires, the overgrowth on the sidewall form extrusions with poor crystal quality, which are a source of non-radiative recombination, and therefore detrimental to solar cell performance. By piranha post-growth etching, we can effectively remove these extrusions, resulting in clean <111> sidewalls without visible defects. This cleaning step leads to an improvement of solar cell efficiency from almost zero to 11.1 % for a nanowire array which covers only 1.8% of the surface area.

One distinctive feature of nanowires is that they enable the growth of both zincblende (ZB) and wurtzite (WZ) crystal phases. Although it is not desirable for solar cells where the intermixing of crystal phases results in enhanced carrier trapping and reduced mobility, a WZ/ZB/WZ nanowire section can provide a so called crystal phase quantum dot/disk (CPQD) in a chemically homogeneous nanowire with atomically flat interfaces. It was demonstrated in chapter 5 that the controlled growth of atomically sharp WZ and ZB GaP nanowire sections results in very sharp quantum dot emissions at visible wavelengths with single photon characteristics. Those quantum structures are promising for the realization of more complex solid-state quantum devices.

The vertical growth of InP NWs on the (100) industry standard InP substrates with a pure zincblende (ZB) crystal structure is technologically relevant for NW solar cells and optoelectronic devices. In chapter 6, we demonstrate that InP NWs grown along the <100> direction are pure ZB regardless of the use of the in-situ dopants. The n-type (with sulfur) and p-type (with zinc) doped <100> InP NWs are investigated by photoluminescence and lifetime measurements. While the sulfur-doped NWs show excellent optical quality, the zinc-doped ones exhibit very low photoluminescence efficiency with a large amount of interstitial zinc (donors). The interstitial zinc degrades the material quality and compensates the substitutional zinc (acceptors). It was found that the amount of interstitial Zn can be significantly reduced by thermal annealing of the NW samples after the growth.

Acknowledgements

The work presented in this PhD thesis is the results of a team effort. The thesis could not be done without the help of many other people. Therefore, I would like to take this opportunity to acknowledge every person who have contributed to this work and supported my research for past four years.

First of all, I would like to express my greatest appreciation to Dr. Jos Haverkort, my daily supervisor, and Prof. Erik Bakkers, my promoter, for giving me the opportunity to carry out a fascinating research on the field of nanowire optics and photovoltaics. Thank Jos for teaching me about semiconductor optics from the very beginning of my PhD, for guiding me to build the micro-photoluminescence setup from the scratch, and for countless scientific discussions. Thank you for being available when I need your helps and for keeping me focused on the nanowire solar cell project. I would like to thank Erik who has been always inspiring me in both research and life. I am so grateful that you always encourage me to set higher standard in my research. I really appreciate your supervision, your great enthusiasm and your constructive comments.

I am very grateful to the members of my dissertation committee: Prof. Jaime Gomez Rivas (who is my second promoter), Prof. Silke Christiansen, Prof. Tom Gregorkiewicz, Prof. Rene Janssen and Prof. Ruud Schropp. Thank you for your time and efforts to read my dissertation and for your invaluable feedback.

I would like acknowledge all the persons I have collaborated with during my past four years. I warmly thank Yingchao Cui, my teammate in the nanowire solar cell project, who has made the most important contribution to the fabrication of the solar cell devices and shared lots of knowledge with me. I also thank Tilman Zehender, Jia Wang, Alessandro Cavalli and Dr. Sebastien Plissard for providing high quality nanowire samples and for explaining me the insight into the growth of nanowires. I really enjoyed working with all you guys. I would like to acknowledge Dr. Nika Akopian and Simone Assali for their great efforts in the project of crystal phase quantum structures. Without their trust, patient, and support, many important results would have not been accomplished. Thank you, Nika, for connecting me to TU Delft where I had performed many experiments and collaborated with excellent colleagues, especially Maaike and Klaus. My work was also largely supported by Dr. Marcel Verheijen who performed many important TEM studies. I also would likely to extend my acknowledgment to Ikaros Hauge for the collaboration on hexagonal silicon (though it is finally not included as a part of this thesis), Anthony

Standing for helping me with transferring nanowires to PDMS, and Dick van Dam for absorption measurements.

My work cannot be carried out smoothly without support from many people in Photonics and Semiconductor Nanophysics (PSN) group. Especially, I would like to acknowledge Prof. Paul Koenraad, Prof. Andrea Fiore, Dr. Rob van der Heijden, Dr. Andrei Silov for being very supportive in my research during past four years.

I would like to acknowledge the help and support from many other people, including Thang Hoang and Ilaria Zardo for sharing their experiences in nanowire optical measurements, Jos and Nando for liquid Helium, Martine and Jos for the installation of the new instrument. Michiel, Joost, Milo, Zili, Tian, Sartoon, Francesco, Leonardo, Dondu, Saeedeh, Steven, Chaoyuan, Rosalinda, Adam and Johannes, thank you all for your helps in the lab every now and then.

My optics lab was very often in the dark, but I could always enjoy the light both in my work and in my life thanks to many wonderful colleagues. Magriet, Annebee, Simone and Thérèse-Anne, thank you all for your support and for organizing great group outing events. Erwin, Ikaros, Diana, Tilman, Rianne, Davide, Rene, Devin and Joris, I will never forget the experience with all kind of 'alcoholic tasting' activities you had organized in PSN group. My special thanks should also go to my PSN football teammates for all the fun and the victories we had together.

I would like to thanks all the present and past members of the group: Michele, Zarko, Douglas, Luca, Julia, Maurangelo, Bruno, Sebastian, Christian, Adam, Sam, Juanita, Ineke, Frank, Rian and Salman for a very nice group atmosphere and for many social activities. I am so grateful to have all of you as my friends and colleagues. There is also a long list of my close friends, both new and old, far away and nearby; their continuous encouragements are the great source of motivation to my life. Thank you all.

Finally, I owe my deepest gratitude to the love, the support, and the encouragement from my parents and my wife Hoa Vu.

List of Publications

This thesis

1. T.T.T. Vu, S. Assali, N. Akopian, M.A. Verheijen, K. Jöns, M.B. Bavinck, J.E.M. Haverkort, and E.P.A.M. Bakkers, Crystal phase quantum structures and spontaneous polarization field in GaP nanowires (submitted)

2. L. Gao, Y. Cui, J. Wang, A. Cavalli, A. Standing, T.T.T. Vu, M.A. Verheijen, J.E.M. Haverkort, E.P.A.M. Bakkers, and P.H.L. Notten, Photoelectrochemical hydrogen production on InP nanowire arrays with molybdenum sulphide electrocatalysts, *Nano Lett.* **14**, 3715–3719 (2014).

3. Y. Cui, J. Wang, S. Plissard, A. Cavalli, T.T.T. Vu, R. Veldhoven , L Gao , M. Trainor, M.A. Verheijen, J.E.M. Haverkort and E.P.A.M. Bakkers, Efficiency enhancement of InP nanowire solar cells by surface cleaning, *Nano Lett.* **13**, 4113-4117, (2013).

4. T.T.T. Vu, T. Zehender, M.A. Verheijen, S. R. Plissard, G.W.G. Immink, J. Haverkort, E.P.A.M. Bakkers, High optical quality of single crystal phase wurtzite and zincblende InP nanowires, *Nanotechnology* **24**, 115705 (2013). (Featured by Nanotechweb)

5. J. Wang, S. Plissard, M. Hocevar, T.T.T. Vu, T. Zehender, G. Immink, M. A. Verheijen, J. Haverkort, E. P. A. M. Bakkers, Position-controlled [100] InP Nanowire Arrays, *Appl. Phys. Lett.* **100**, 053107 (2012).

Other topics (not included in this thesis)

6. D.F. Wang, J.M. Kim, M.S. Seo, T.T.T. Vu, Y.J. Yoo, Y.P. Lee, and J.Y. Rhee, Magnetoresistance in ZnO induced by spin-splitting and weak localization, *Mat. Chem. Phys.* **134**, 74 (2012)

7. N.T. Tung, J.W. Park, T.T.T. Vu, P. Lievens, Y.P. Lee, and V.D. Lam, Characterization and electromagnetic response of a Φ-shaped metamaterial, *The European Physical Journal B* **81**, 263 (2011).

8. T.T.T. Vu, N.T. Tung, V.D. Lam, J.W. Park, J.Y. Rhee, and Y.P. Lee, In-plane interactions in supercell of cut-wire pairs, *J. of Korean Phys. Soc.* **58**, 87 (2011).

9. J.W. Park, N.T. Tung, T.T.T. Vu, V.D. Lam, and Y.P. Lee, Strong tie between cut-wire pair and continuous wire in combined, *Opt. Commu.* **284**, 919 (2011).

10. T.T.T. Vu, N.T. Tung, J.W. Park, V.D. Lam, Y.P. Lee and J.Y. Rhee, Highly dispersive transparency in coupled metamaterials, *J. Optics* **12**, 115102 (2010).

11. T.T.T. Vu, D.T. Viet, N.V. Hieu, V.D. Lam, Y.P. Lee, N.T. Tung, Triple negative permeability in cut-wire-pair metamaterials by plasmon hybridization, *Opt. Commun.* **283**, 4303 (2010).

12. N.T. Tung, T.T.T. Vu, J.W. Park, J.Y. Rhee, and Y.P. Lee, Left-handed transmission in a simple cut-wire pair structure, *J. Appl. Phys.* **107**, 023503 (2010).

13. N.T. Tung, T.X. Hoai, V.D. Lam, J.W. Park, T.T.T. Vu, and Y.P. Lee, Perfect impedance-matched left-handed behavior in combined metamaterial, *The European Physical Journal B* **74**, 47 (2010).

Curriculum Vitae

Vu Tran Thanh Thuy

Born 14th of September 1985 in Nam Dinh, Vietnam

2010 – 2015	PhD student at Eindhoven University of Technology, Photonics and Semiconductor Nanophysics group Thesis: *Nanowire photoluminescence for photovoltaics* Promotors: prof. dr. E.P.A.M. Bakkers and prof. dr. J. Gomez Rivas Co-promotor: dr. J.E.M. Haverkort
2008 – 2010	M.Sc. in physics, Department of Physics, Hanyang University, Seoul, South Korea (with full scholarship) Thesis: *A study on the coupling effects between constituent elements of metamaterials* Supervisor: prof. dr. YoungPak Lee Best award for international excellent students (HIEA), 2008-2009, Hanyang University (GPA: 4.44/4.5)
2007 – 2008	Researcher, Laboratory of Laser Spectroscopy, Institute of Physics, Hanoi, Vietnam
2003 – 2007	B.Sc. in physics, Honors Program, Department of Physics, Hanoi National University of Education First Prize, 10th National Physics Olympiad for students, 2006, Vietnam Physical Society